Study of Human Motion Control with a Physiology Based Robotic Arm and Spinal Level Neural Controller

by

Ching-Ping Chou

A dissertation submitted in partial fulfillment
of the requirements for the degree of

Doctor of Philosophy

University of Washington

1996

Approved by ______________________________
(Chairperson of Supervisory Committee)

____

____

____

____

Program Authorized
to Offer Degree **Department of Electrical Engineering**

Date ______________________________

University of Washington

Abstract

Study of Human Motion Control with a Physiology Based Robotic Arm and Spinal Level Neural Controller

by **Ching-Ping Chou**

Chairperson of the Supervisory Committee: **Professor Blake Hannaford**
Department of Electrical Engineering

The goals of this research are: 1) to apply knowledge of human neuro-musculo-skeletal motion control to build a physiology based neural controller and biomechanics based "anthroform" robotic arm system, and 2) to utilize the neural controller and anthroform arm system to study some controversial issues and to predict new phenomena of the human motion control system.

A physiologically analogous artificial neural network controller, a feed-forward controller, and two anatomically accurate robotic arms (the Anthroform Arm and the testing elbow) are implemented and applied in this study. In order to build the physical arm systems to have mechanical properties as close as possible to the human arm, McKibben pneumatic artificial muscles, force sensors, and mechanical muscle spindles are integrated in the systems with anatomically accurate muscle attachment points. In addition, the neural controller emulates the behavior of spinal segmental reflex circuitry in real time, which includes motoneurons, interneurons, and Ia and Ib afferent feedbacks. The feed-forward controller emulates the inverse kinematics and inverse dynamics functions of higher central nervous system to convert conceptual movement parameters to spinal neural activation patterns.

Systematic experiments of elbow posture maintenance and voluntary fast flexion movement are performed and compared to physiological experimental data. New experiments are performed in which responses to torque perturbation are measured when selected afferent pathways are blocked. A "covariance diagram" is introduced. And a linear model is used to help to analyze the roles of system components and the stability. The results show: 1) the neural controller and testing elbow system is capable of similar performance in posture maintenance as the human elbow. 2) Muscle co-contraction and Ia afference with gamma motoneuron excitation are two effective ways to increase joint stiffness and damping, which in turn reduces the mechanical sensitivity of the joint to external perturbation and shorten the settling time of the system. 3) Feed-forward inverse dynamics information is important to performing voluntary fast movement. And 4) feedback delay limits the maximum loop gain of the closed-loop controlled system to maintain stability and still produce enough additional torque to resist external perturbations during voluntary movement. A higher level "nearly open loop" predictive feedback mechanism is proposed for solving this high-loop-gain instability problem. Physiological experiments are encouraged to verify the above phenomena in the future.

TABLE OF CONTENTS

LIST OF FIGURES

LIST OF TABLES

ACKNOLEDGMENTS

First of all, I am grateful to my parents, Yi-Shin Chou and Jan-Her-Jen Chou. They have been encouraging and supporting me achieving higher education for over twenty-two years. I want to thank my wife, Meei-Ling Chiang. She has been studying together with me in EEUW since we first arrived this foreign country, USA, and took care of the family when I was busy in preparing this dissertation.

I am grateful to Professor Blake Hannaford. He has been advising me not only on the research, but also on English and American living style since my master's study. Thanks to Professor Robert Pinter and Professor Jenq-Neng Hwang for spending the time on reading the draft of this dissertation. And thanks to Professor Marc Binder for giving me valuable information of physiology when needed.

Thanks to Pierre Marbot, who built the mechanical spindles and wrote half of the software used in the system; Professor Jack Winters and his students in Catholic University of America who built the first version of the anthroform arm; Glenn Klute, who helped me to make new artificial muscles and to rebuild the anthroform arm; Ian MacDuff and Steven Venema, who designed the DSP computer; and Melani Shoemaker, who designed the analog interface card for the DSP computer. I also want to thank all the students in the Biorobotics Laboratory and the Genomation Laboratory, who formed a very pleasant international-style working environment.

Finally, I am grateful to US Office of Naval Research and National Science Foundation, by whom this research was supported.

I. Introduction

1.1. Objectives

The goals of this research are twofold. The first is to apply knowledge of human neuro-musculo-skeletal motion control to build a physiology based neural controller and biomechanics based “anthroform” robotic arm system. This kind of system is expected to have similar motion control performance to human arm in terms of smoothness, compliance, accuracy, and stability.

On the other hand, unlike physiological experiments with human or animal subjects, which are usually constrained by in vivo or in vitro conditions, experiments with the neural controller and anthroform arm system can be performed completely and systematically under different conditions. In addition, the system parameters, such as synaptic weights and propagation delays, can be easily modified in experiments to highlight particular roles of the system components. As a result, the second goal of this research is to utilize the neural controller and anthroform arm system to study some controversial issues and to predict new phenomena of the human motion control system.

1.2. Overview

While modern control research is still developing a number of theories to solve motion control problems, the human musculo-skeletal motion system has been proven to succeed by nature for thousands of years. Scientists have long attempted to fully understand the functioning of human motion control. However, the complexity of the system and the lack of technology made this very difficult. With the development of advanced electronic instruments and medical techniques, more and more insight into the human nervous system has been discovered, and more and more researchers have gone into this area.

The approach to human motion control research can be either top-down or bottom-up. While the top-down approach starts from the conceptual layer (task) and proceeds through the functional layer (block) to physical (device) layer, the bottom-up approach just reverses this ordering. The foci can be roughly partitioned into high level control and low level control. The high level control focuses on brain functionality, such as motion planing and learning (Alexander et al. 1992) (Gomi & Kawato 1993) (Raibert 1978). The low level control focuses on spinal cord functionalities, such as short latency reflex and the integration of voluntary commands into spinal neural circuitries. Neither the top-down or bottom-up approach has achieved full understanding of the system. As a result, it is very reasonable that the high level control research chooses a top-down approach and the low level control research chooses a bottom-up approach.

In order to incorporate the goals of this research, I started by focusing on the low level control and using a bottom-up approach. Existing low level neural control research can be partitioned into two stages, the controller and the plant. The controller can be further classified into two types: 1) conventional feedback controller with minimal or very abstract neural control concepts (He et al. 1991) (Ramos et al. 1990) (Yoshida & Horch 1996), and 2) artificial neural network controller with functional reproduction of human neural circuitry (Bullock et al. 1992) (Hannaford et al. 1995). Similarly, the plant can be classified into four types: 1) mathematical dynamics models (Bullock et al. 1992)(He et al. 1991) (Ramos et al. 1990), 2) conventional robotic arms with muscle-like actuators (Inoue 1988), 3) anthroform robotic arms (Hannaford et al. 1995), and 4) biological limb (Jacks et al. 1988) (Wierzbicka et al. 1986) (Yoshida & Horch 1996). Here we define the term "anthroform" to describe a robotic arm in which all aspects of its design are specified in terms of emulation of the corresponding functions of the human arm. Many of these approaches have established new research directions.

This study used a physiologically analogous artificial neural network controller and two biomechanics based robotic arms. The first arm, named the "Anthroform Arm", is a physical multi-joint musculo-skeletal model. The Anthroform Arm has several mechanical properties which are very close to the human arm: 1) McKibben pneumatic actuators (Schulte 1961) were chosen as artificial muscles, which have the closest mechanical properties to biological muscles among various artificial actuators (Chou & Hannaford 1994, 1996) (Hannaford & Winters 1990). And 2) the shapes of the skeletons and the joints, and the attachment points of the muscles were designed based on human anatomical geometry (Snell 1980) (Zuckerman & Matsen 1989) to mimic the real human arm mechanical properties around shoulder and elbow joints. The second arm, named the "testing elbow", is a physical single-joint model with the abstract properties of the Anthroform Arm around the elbow joint. In addition, force sensors which act as Golgi tendon organ (GTO), and mechanical muscle spindles (Marbot 1995) (Marbot & Hannaford 1993) which mimic the behavior of biological muscle spindles (Marbot 1995) (Marbot & Hannaford 1993) are integrated in the testing elbow to perform closed loop control.

On the other hand, the physiologically analogous artificial neural network controller (Hannaford et al. 1995) is implemented by a DSP computer system to emulate the behavior of spinal segmental reflex circuitry (Binder 1989b, 1989c) (Gandevia & Burke 1992) (McCrea 1992), including alpha and gamma motoneurons, Ia and Ib afferent sensory neurons, Ia inhibitory, Ib inhibitory, and Renshaw cell interneurons, and descending inputs to the motoneurons and interneurons. This neural controller was used with the testing elbow to perform a series of posture maintenance experiments. In addition, a feed forward controller which implements the inverse kinematics and inverse dynamics features of the higher level central nervous system was involved on top of the spinal level neural controller to perform voluntary fast movement experiments.

There are three key reasons to use a physical arm instead of a mathematical model: 1) a physical system will obey all physical laws which otherwise may be neglected or may not even be considered when modeling or during simulation. At first glance it would see unlikely that a computer simulation of physically correct differential equations would be capable of violating physical laws. However due to quantization error and sampling, simulations of correctly modeled physical elements can lead to violation of conservation of energy. 2) While we can build a physical arm with mechanics as close as possible to human arm, the complexity of a mathematical model which implements similar details of mechanics will make it very difficult to simulate. And 3) the implementation of the physical anthroform arm itself will help develop new technologies on actuators, sensors, and prosthetic arm.

However, there are two major limitations for the testing elbow and neural controller system: 1) since the large number of motor units in a biological muscle are emulated in the system by only one artificial muscle and motoneuron, phenomena related to motor unit recruitment can not be studied. 2) Since only one sensor of each type is used for each muscle, spatial summation of multiple afferent signals will not take effect.

Two series of experiments were performed with the testing elbow and the spinal neural controller: the posture maintenance series and the voluntary fast flexion series. In the posture maintenance experiments, the performance of the testing elbow and neural controller system against external disturbances will be compared to a physiological experiment performed by Lacquaniti et al. (1982). The results demonstrate that the testing elbow and neural controller system has very similar performance to the human's motion system. The system behavior will also be analyzed with reference to a linearized model, with which the specific roles of neural circuit elements will be identified and some nervous system abnormalities predicted.

In the voluntary fast flexion experiment, the feed forward controller is added on top of the spinal neural controller, which provides a solution to the inverse kinematics and inverse dynamics problems. The results are compared to another physiological experiment performed by Dufresne et al. (1978). Based on the discrepancy of the experimental results, an important role is suggested for a long latency feedback mechanism in control of fast movements.

1.3. About This Dissertation

First, short reviews of related research will be given in Chapter 2. According to the bottom-up approach, the devices used in this study will be described next, followed by the arm sub-systems and the neural controller. These include the measurement and modeling of the McKibben pneumatic artificial muscles in Chapter 3, a brief introduction to the mechanical muscle spindle in Chapter 4, the implementation of the Anthroform Arm and the testing elbow in Chapter 5, and the implementation of the spinal level neural controller in Chapter 6. After that, two series of experiments will be described. These include posture maintenance experiments in Chapter 7, and voluntary fast forearm flexion experiment in Chapter 8. Finally, conclusions will be given in Chapter 9.

II. Literature Review

2.1. Reviews

Bullock et al. (1992) proposed a physiology based neural network model of the human spinal circuitry with a mathematical model of muscle and joint in the simulations of joint equilibria and point to point movement. The model consists of alpha and gamma motoneurons, Ia and Ib afferents, and various feed-forward and recursive interneurons, and is even more detailed than the one used in this study. However, the mathematical model of muscle and joint are much simpler and, as a result, cannot demonstrate the particular roles of the network components. In addition, their simulation results were never directly compared to physiological experiments.

He et al. (1991) proposed a partially linear model for the neuromuscular control of posture, and a mathematical model for the muscle activation and limb mechanics. By abstracting some concepts of spinal neurophysiology, the model included four types of feedbacks: 1) motoneuron activation feedback (corresponding to Renshaw cell), 2) muscle length and velocity (Ia afferent), 3) muscle tension (Ib afferent), and 4) joint angle. However, the non-linearity which exists in the biological sensors and neurons was not simulated. Also, there was no gamma motoneuron excitation and spinal interneuron recursive inhibition as they exist in the human neuro-musculo-skeletal system. On the other hand, the mathematical model of the muscle and limb consisted of nonlinear muscle activation and dynamics, and linearized mechanics of cat hind limb. The linearized limb mechanics model limited their simulation to a very small range of movement.

Inoue (1988) applied the McKibben muscle in a robotic design. A non-biomechanically designed robot arm and a conventional feedback controller were used in his study. Although it is not very related to human motion control, it is still worth mentioning because of the physical application of the muscle-like, McKibben pneumatic actuator.

Jacks et al. (1988) studied the instability of human forearm movements with feedback controlled electrical stimulation of muscles. Amplitude-modulated electrical stimulation was applied to the elbow flexor and extensor muscles to produce forearm movements in normal human subjects. And the transduced forearm signals were fed back through a filter to derive the analogous muscle spindle Ia afferents. With these efforts, they replaced the neural part of the reflex arc with the artificial controller, but left the musculoskeletal part intact. The instability experiments were performed by increasing the gain and delay of the feedback pathway. The results showed that all subjects developed forearm oscillations when the loop gain exceeded a threshold value.

Ramos et al. (1990) proposed a piecewise linear feedback controller and a mathematical model for the muscle and joint. Only the joint angle, which is linear to the muscle length in their joint mechanics model, has feedback in the controller. Along with the first and second derivatives and the propagation delay, this feedback was proposed to model the Ia afferent pathway. The mathematical model of the muscle and joint consists of linear muscle activation, nonlinear muscle dynamics, and linear joint mechanics. Instead of performing spinal reflex simulation, they applied this model in the simulation of voluntary movement to study the temporal patterns of the descending commands.

Wierzbicka et al. (1986) studied fast voluntary movements of the human forearm with electrical stimulation on forearm muscles. They reproduced the three distinct bursts of EMG activity in antagonistic muscles, which normally appear during fast voluntary movement, through surface electrodes stimulation, and found the relationships between the movement parameters and the stimulation voltage.

Yoshida and Horch (1996) implemented a closed loop functional neuromuscular stimulation (FNS) controller in ankle position control experiments with neurally intact anesthetized cats and unanesthetized decerebrate cats. The signals from muscle spindle afferents were measured to provide the position and velocity feedback information. After some signal mapping mechanisms, the error signal between the target position and estimated position was generated to stimulate the ankle muscles through electrodes. Although the controller is not a physiologically analogous neural network controller, this is the only study reviewed in this chapter which performs the closed loop experiments with the spindle afferent signals on real animal subjects.

2.2. Conclusion of reviews

According to the reviews given in the above section, no one has ever performed the lower level human motion control studies with the COMBINATION of a physiologically analogous neural controller AND a real human (animal) arm or a biomechanically accurate physical robot arm. The feedback controllers used in the above studies, although valuable, cannot physiologically reflect the neural processes of the human spinal circuitry. On the other hand, the mathematical model of the muscle activation and limb mechanics are commonly over simplified. This will significantly reduce the ability to discovering the insight of human motion control mechanisms.

III. McKibben Pneumatic Artificial Muscle

McKibben pneumatic artificial muscle, mechanical muscle spindle, and artificial Golgi tendon organ (GTO) are three devices which make the testing elbow different from a conventional robotic arm. Before applying the McKibben pneumatic artificial muscles to the testing elbow and the Anthroform Arm, we must fully understand their mechanical properties. The mechanical spindle will be introduced in the next chapter. The GTO is implemented by strain gauge bridge force sensor, and will not be described in more detail in this dissertation. Many of the results in this chapter have recently appeared in Chou & Hannaford 1996.

3.1. Introduction to McKibben Pneumatic Artificial Muscle

The McKibben pneumatic artificial muscle was developed in artificial limb research in the 1950s and 1960s (Schulte 1961, Gavrilovic and Maric 1969). They have recently been commercialized by the Bridgestone Rubber Company of Japan for robotic applications (Inoue 1988), and re-engineered by Dr. Jack Winters for construction of biomechanically realistic musculo-skeletal models.

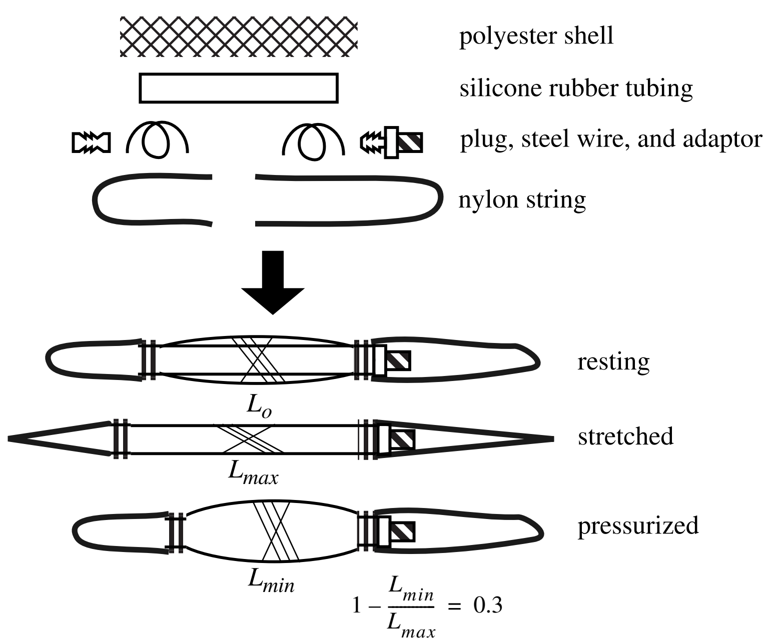

Fig.3.1 Construction of McKibben muscle.

In general, McKibben muscles consist of an internal bladder surrounded by a braided mesh shell (with flexible yet non-extensible threads) that is attached at either end to fittings or to some tendon-like structure (Fig.3.1). When the internal bladder is pressurized, the high pressure gas pushes against its inner surface and against the external shell, and tends to increase its volume. Due to the non-extensibility (or very high longitudinal stiffness) of the threads in the braided mesh shell, the actuator shortens according to its volume increase and/or produces tension if it is coupled to a mechanical load. This physical configuration causes McKibben muscles to have variable-stiffness spring-like characteristics, non-linear passive elasticity, physical flexibility, and very light weight. All of these characteristics make the McKibben muscles much more similar to biological muscles than other kinds of artificial actuators (Hannaford and Winters 1990).

The relationships between tension, length, velocity, and activation are major characteristics of actuators which vary greatly from type to type. Human skeletal muscle also has its own particular characteristics: for example, the convex shape active tension-length relationship (Gordon et al. 1966), the non-linear passive tension-length relationship, and the hyperbolic tension-velocity relationship (Hill 1938). Each of these properties is also a function of activation level (McMahon 1984, Winters 1990, Zahalak 1990). In order to show the similarity to biological muscles, four types of McKibben muscles were tested. Also, an idealized static physical model of McKibben muscles will be analyzed with an accurate yet simple theoretical approach.

3.2. Dynamic Testing Machine

For the following experiments, a testing system capable of producing and recording desired patterns of the tension, length, and pressure of the actuator was built (Fig.3.2). The system consists of an IBM compatible personal computer (PC, with 16 MHz 386sx, real time updating rate up to 5 kHz), PC extension bus interface and timers, A/D and D/A converters, analog filters and amplifiers, pressure sensors (100 psi, 6.8 bar max.), strain gauge force sensors (100 N max.), a 1/4 horse power DC motor with PWM power amplifier (± 24 A max. current), an optical angular position incremental encoder (1600 steps per

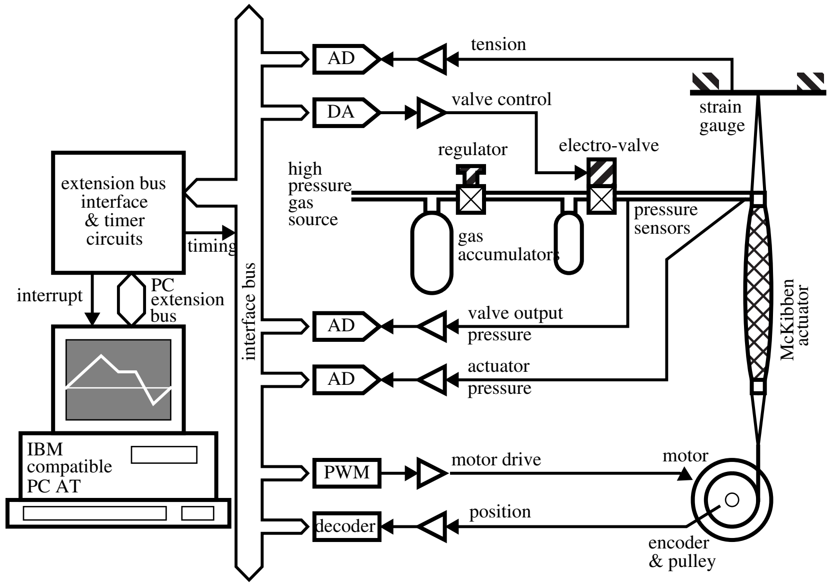

Fig.3.2 Dynamic testing system.

revolution) and a decoder, a pressure regulator (10 bar max.), an electro-valve (Festo proportional pressure regulator MPP-3-1/8, 10 bar max.), two gas accumulators (3 in^3 and 10 in^3), and flexible tubing (ϕ 1/8")

By utilizing different combinations of the I/O channels and software settings, the system can performs a variety of testing conditions, such as constant pressure testing, isometric testing, and isotonic testing.

3.3. Constant Pressure Tension-Length Relationships

3.3.1. Quasi-static experiments

Since there is no analytical solution to describe biological muscle tension-length-activation relationships, a variety of testing configurations have been chosen to illustrate part of this relationship, such as static tension-length relationship under constant activation level (Gordon et al. 1966), isometric to isotonic quick release experiment (Gasser and Hill 1924), isokinetic experiment (Gasser and Hill 1924, Levin and Wyman 1927), isometric tension in response to activation (Burke et al. 1976, Chou and Hannaford 1992), etc. Notice that the activation is always an input to muscle mechanics, and either one of the other two quantities (tension and length) may be input or output.

The pressure of the actuator is analogous to the activation level and will initially be thought of as an input to the actuator. It will be held as constant as possible in these experiments in order to minimize the effects of the pressure dynamics and thus simplify the analysis.

Four types of actuators were tested here. The first one, with nylon shell, is 14 cm in resting length (L_o), and 1.1 cm in diameter at 5 bar no load. The second one, with fiberglass shell, is 20 cm in length, 0.9 cm in diameter. The third one, manufactured by Bridgestone, is 14.7 cm in length, and 1.5 cm in diameter. And the last one, which was used in the testing elbow and the Anthroform Arm, with polyester shell and more reliable, re-designed fitting, is 30.5 cm in length, and 1.5 cm in diameter.

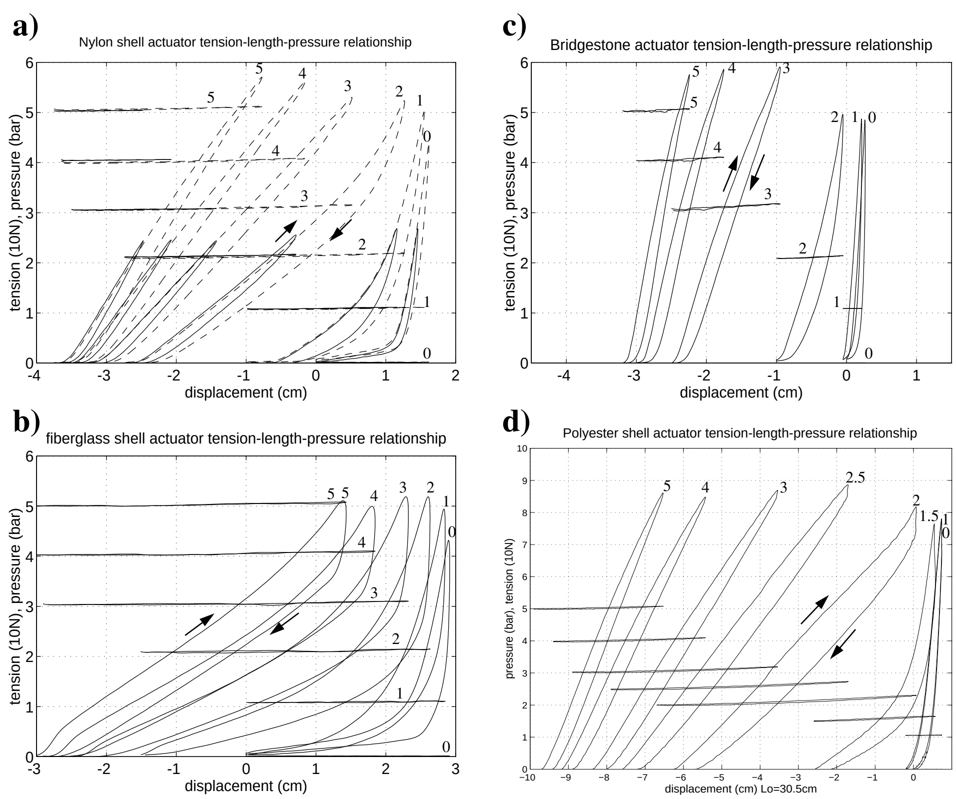

Fig.3.3 a to **d** Tension-length-pressure relationships of four types of McKibben actuators. Pairs of curves are superimposed in plots: nearly horizontal curves, measured pressure-length; sloped curves, tension-length. Operating pressure in bar is printed just above each tension-length loop. Hysteresis direction is clockwise. **a** Solid lines: small displacement range; dashed lines: large displacement range.

A set of 1 Hz triangular wave displacements to best cover the non-saturated tension regions for several pressure levels were selected for each actuator as the length input. This yields the peak velocity of 0.3 L_o/s.

The pressure was set by a manual regulator to obtain six desired constant levels (0-5 bar relative). Due to 1) the volume change of the actuator with length change, 2) the gas viscosity in connection tubing, and 3) the regulator's output hysteresis, the measured pressure will increase when the actuator lengthens and will decrease when it shortens. In order to reduce the variation of the pressure, a 10 in^3 (164 cm^3) accumulator was connected to the regulator, and a 3 in^3 (49 cm^3) accumulator was connected directly to the actuator. As a result, the pressure variation was limited to less than 0.1 bar due to the large total capacity of the accumulators, and the pressure hysteresis was almost immeasurable due to the close position (to the actuator) of the second accumulator.

Both the measured pressure and the tension are shown in response to the displacements (Fig.3.3). By minimizing the effect of pressure variation, the hysteresis loop of the tension-length relationship is illuminated. The width and height of the loop for the nylon shell actuator (Fig.3.3 a) is about 0.2-0.5 cm and 5-10 N respectively. The stiffness, friction, and extensibility are quite different in these four actuators. Two further experiments were made with the nylon shell actuator to illustrate more features of the hysteresis.

First, the frequency of the displacement waveforms is reduced to 0.25 Hz, while the displacement range remains the same (which yields the peak velocity of 0.075 L_o/s). The result is almost identical to the previous case, which suggests that at low velocity, the tension-length behavior is velocity independent (when the pressure hysteresis is suppressed). Second, the frequency is set to 1 Hz, while the displacement range is reduced about half (Fig.3.3 a, solid lines). The tension rising paths remain the same (the rising "initial conditions" are the same), but the falling paths are different (The falling "initial conditions" are different due to the smaller displacement). As a result, the width and height of the loop are reduced. This indicates the hysteresis is history dependent.

3.3.2. Dynamic experiment

In dynamic experiment, a set of middle to high frequency sinusoidal wave displacements with small displacement range were applied to the nylon shell actuator. The pressure was set to relative 5 bar, and remains constant quite well in this condition due to smaller length change. The frequencies and displacement ranges are designed to obtain 0.2-8.0 L_o/s peak velocity and remain in the non-saturated tension-length region. The viscous friction (damping force) if measurable, would be revealed by a hysteresis width which is a monotonic increasing function of the velocity. However, the results show that the width of the tension-displacement loop is almost unchanged, except for a slight decrease at higher frequency (Fig.3.4).

These results indicate that the velocity-independent hysteresis is most likely to be the Coulomb friction, which dominates the total friction of the actuator. The viscous friction is much smaller than Coulomb friction and thus immeasurable.

3.4. Isometric and Isotonic Experiments

In these two series of experiments, additional characteristics related to both the actuator and gas dynamics will be demonstrated. Particular patterns of control voltage were input to the electro-valve to generate dynamic pressure waveforms. Although no mathematical

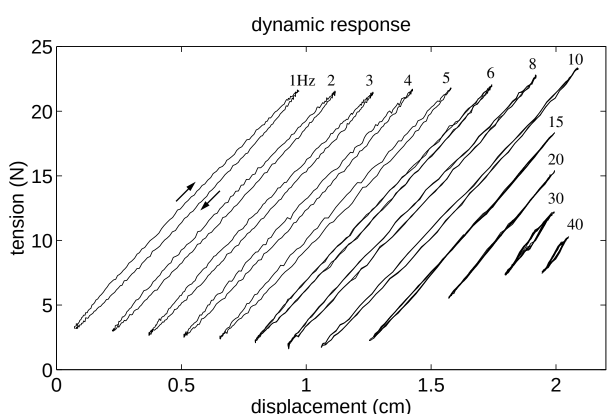

Fig.3.4 Dynamic sinusoidal responses. Results for 12 frequencies are combined together with shifting curves along displacement axis. Notice width of hysteresis is almost unchanged for peak velocity from 0.2 L_o/s (1 Hz) to 2.0 L_o/s (10 Hz). Hysteresis direction is clockwise.

model will be introduced for the gas dynamics, these experiments will still give valuable information on the timing of the response waveform and the power capability of the system. Please refer to (Chou & Hannaford 1996) for more detail on the experiment and modeling of the actuator gas dynamics, and the analysis and comparison of energy efficiency of the actuators and biological muscle.

3.4.1. Isometric experiment

In this experiment, without using the motor, the actuator was fixed at the end to a stiff metal plate. Two pressure sensors were placed one at the output of the electro-valve and the other at the fitting of the actuator with a 1 m long, 1/8” diameter tubing in between. The pressure and the tension is recorded in response to a square wave (steps) control voltage (Fig.3.5).

The delay time from the control voltage stepping to the output pressure rising is about 5 ms, purely due to the delay of the valve. The pressure delay between the two sensors is about 4 ms, this is the gas propagation time. From the rise of pressure to the rise of tension

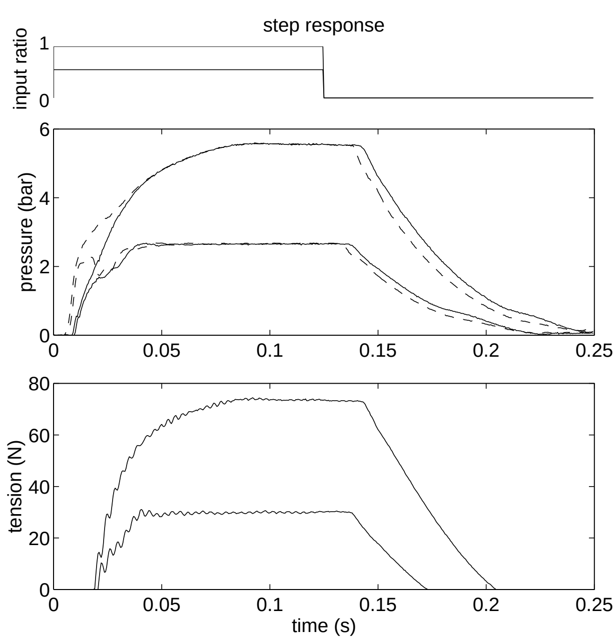

Fig.3.5 Isometric step responses. Two sets of curves in response to two different amplitudes of control voltage steps are superimposed in plot. Upper lines, control voltage ratio; dashed lines, valve output pressure; middle solid lines, actuator pressure; lower lines, tension.

is about 10 ms, mostly because it takes time for the pressure to overcome the threshold (P_{th}). However, longer delays were observed in other experiments when the control voltage changed slower unlike a step. The tension rising time (0 to 90%) is 30 ms for the full range step and 15 ms for the half range step, and the falling time (100% to 10%) is 53 ms and 30 ms respectively, these are limited by the maximum flow rate of the valve and the gas viscosity of the tubing (and connectors).

3.4.2. Isotonic experiment

In this experiment, closed loop control of the tension was performed by feeding back the measured tension to the motor drive. Three different frequency (1, 2, and 5 Hz) triangular waveforms were applied to the valve control voltage, and three different load levels (10, 30, and 50 N) were selected for the controlled tension. The pressure, shortening (negative displacement), and measured tension of selected typical results are shown in Fig.3.6.

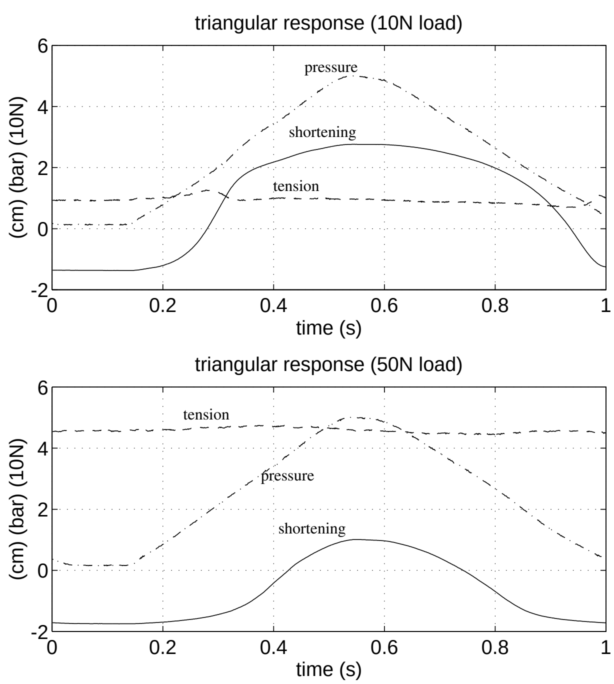

Fig.3.6 Isotonic triangular responses. Two typical results are shown at 1 cycle per second with 10 N and 50 N load respectively. Center lines, actuator pressure; dashed lines, tension; solid lines, shortening. Power is product of tension and shortening velocity.

The highest average velocity of 41.0 cm/s and peak velocity of 86.6 cm/s in these experiments were obtained at 5 cps with 10 N load. It is evident that the measured tension has some variation due to limited capability of the motor and the bandwidth of the feedback. However, the positive work and power can still be calculated by numerically integrating the product of tension and shortening velocity. This gave the positive work per each shortening of 0.45 J, average power of 0.9 W, and peak power of 3.8 W at 1 Hz with 10 N load, or the work per each shortening of 1.4 J, average power of 14 W, and peak power of 33 W at 5 Hz with 50 N load. These values are for reference but do not represent the maximum capability of the actuator. The maximum power is mostly limited by the maximum pressure of the gas source, the maximum flow rate of the valve, and the gas viscosity inside the pneumatic circuit.

3.5. Modeling of the McKibben Muscles

3.5.1. Static model of McKibben muscles

McKibben muscle is an actuator which convert pneumatic (or hydraulic) energy into mechanical form by transferring the pressure applied on the inner surface of its bladder into the shortening tension. In order to find the tension as a function of pressure and actuator length without involving the detailed of the geometric structure, a theoretical approach based on energy conservation is introduced first.

The input work (W_{in}) is done in the McKibben muscle when gas pushes the inner bladder surface. This is

$$dW_{in} = \int_{S_i} (P - P_o)\, d\mathbf{l_i} \cdot d\mathbf{s_i} = (P - P_o) \int_{S_i} d\mathbf{l_i} \cdot d\mathbf{s_i} = P' dV \qquad 3.1$$

where P is the absolute internal gas pressure; P_o, the environment pressure (1 atm,1.0336 bar); P', the relative pressure; S_i, total inner surface; $d\mathbf{s_i}$, area vector; $d\mathbf{l_i}$, inner surface displacement; and dV, the volume change. The output work (W_{out}) is done when the actuator shortens associated with the volume change, which is

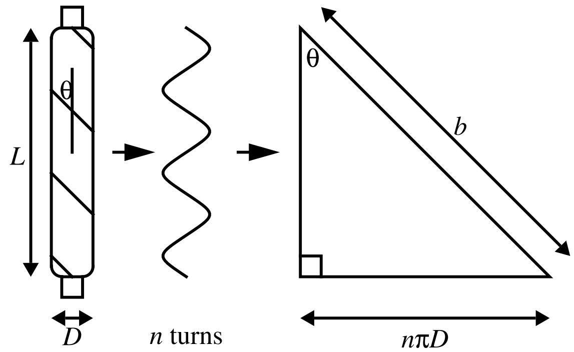

Fig.3.7 Geometry of the actuator. The middle portion of the actuator is modeled as a perfect cylinder with length L and diameter D. θ is the angle between a braided thread and the cylinder long axis, n, number of turns of a thread, and b, the thread length. The relationship between the above parameters is illustrated by the triangle.

$$dW_{out} = -FdL \qquad 3.2$$

where F is the axial tension, and dL, the axial displacement. From the view of energy conservation, the input work should equal the output work if a system is lossless and without energy storage. Assume the actuator is in this ideal condition. We can then use the "virtual work" argument:

$$dW_{out} = dW_{in}, \qquad 3.3$$

as a result, with Equ.3.1 and Equ.3.2, yields

$$-FdL = P'dV, \qquad 3.4a$$

$$F = -P'\frac{dV}{dL}. \qquad 3.4b$$

To estimate dV/dL, first we assume the extensibility of the shell threads is very low (as it has to be chosen), so the actuator volume will only depends on its length. In addition, the middle portion of the actuator is modeled as a perfect cylinder with zero-wall-thickness (Fig.3.7), where L is the length of the cylinder;θ, the angle between a braided thread and the cylinder long axis; D, the diameter of the cylinder; n, number of turns of a thread; and b, the thread length. L and D can be expressed as functions of θ with constant parameters n and b,

$$L = b\cos\theta, \tag{3.5}$$

$$D = \frac{b\sin\theta}{n\pi}. \tag{3.6}$$

The volume of the cylinder is

$$V = \frac{1}{4}\pi D^2 L = \frac{b^3}{4\pi n^2}\sin^2\theta\cos\theta. \tag{3.7}$$

So, from Equ.3.4b, F can be expressed as a function of P' and θ,

$$F = -P'\frac{dV}{dL} = -P'\frac{dV/d\theta}{dL/d\theta} = \frac{P'b^2\left(2\cos^2\theta - \sin^2\theta\right)}{4\pi n^2} = \frac{P'b^2\left(3\cos^2\theta - 1\right)}{4\pi n^2}, \tag{3.8a}$$

which is equivalent to

$$F = \frac{\pi D_o^2 P'}{4}\left(3\cos^2\theta - 1\right) \tag{3.8b}$$

where $D_o = b/n\pi$, is the ideal diameter when θ equals 90°, which is the same form used in Schulte's paper (1961). The tension is thus linearly proportional to the pressure, and is a monotonic function of the braid angle (0° < θ < 90°). The maximal shortening will be reached when $F = 0$, that is, θ = 54.7°.

Notice that although we calculate the tension with the assumption of ideal cylinder here, the tension can always be derived by knowing the dV/dL of any arbitrary shaped actuator without the assumption, and applying to Equ.3.4b.

Excluding the measured Coulomb friction, a hypothetically static tension-length relation can be calculated by applying the geometry parameters (measured from the nylon shell actuator, $b = 16.4$ cm, $n = 3.15$, and yields $D_o = 1.66$ cm) to Equ.3.8b. The simulation result is shown in Fig.3.8 a to d (solid lines).

Non-ideality and simplification of the static model

Now, if the thickness (t_k) of the shell and bladder is considered, the volume becomes

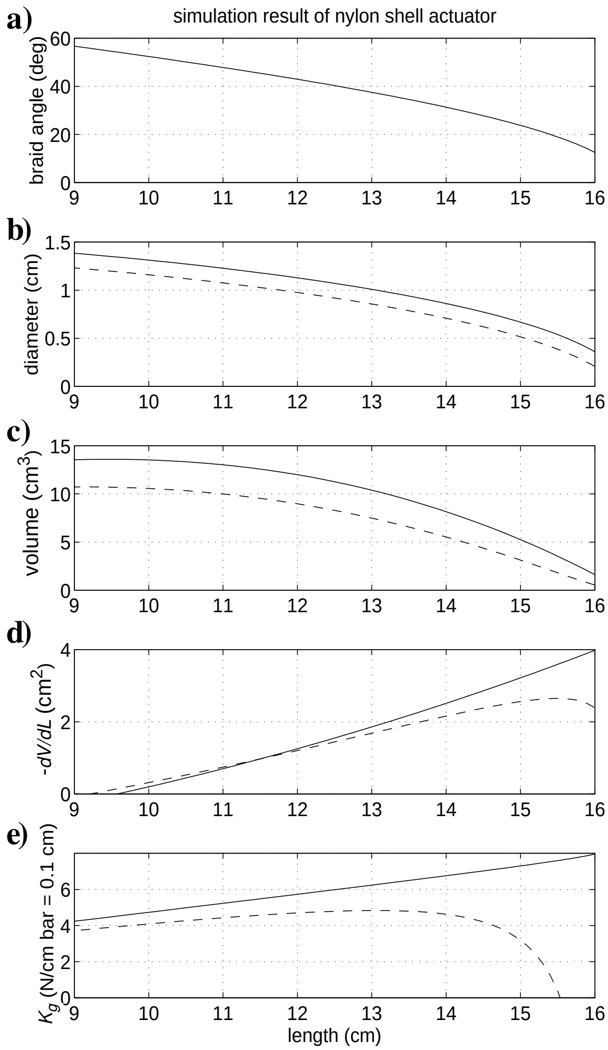

Fig.3.8 a to **e** Simulation results of nylon shell actuator's static characteristics as function of length. Dashed lines, results considering thickness of braided shell and bladder; solid lines, results without considering wall thickness.

$$V = \frac{1}{4}\pi (D - 2t_k)^2 L, \tag{3.9}$$

by plugging into Equ.3.4b,

$$F = -P'\frac{dV}{dL} = \frac{\pi D_o^2 P'}{4}\left(3\cos^2\theta - 1\right) + \pi P'\left[D_o t_k\left(2\sin\theta - \frac{1}{\sin\theta}\right) - t_k^2\right]. \tag{3.10}$$

This is more accurate but more complex than Equ.3.8b (Fig.3.8 a to d dashed line, with $t_k = 0.0762$ cm in addition).

Fortunately, a simplified model can be obtained by considering the tension as a function of the pressure and the length. In this format, the actuator is just like a variable-stiffness elastic element, or a "gas spring". According to Equ.3.10, the stiffness ($K \equiv dF/dL$) is proportional to the pressure, and the stiffness per unit pressure ($K_g \equiv dK/dP'$) approximates a constant within 10 to 14 cm length by simulation (Fig.3.8e, K_g = 4.61 N/cm·bar, or 0.461 cm). As a result, it can be linearized as

$$F = K_g P' (L - L_{min}) + nl(L) \qquad 3.11$$

where L_{min} is the theoretically possible minimum length (when $F = 0$).

Now, considering energy stored by the actuator in its bladder and shell, yields

$$F = K_g (P' - P_{th}) (L - L_{min}) + K_p (L - L_o) + nl(L) \qquad \text{if } P' > P_{th}\text{, or} \qquad 3.12a$$

$$F = K_p (L - L_o) + nl(L) \qquad \text{if } P' \leq P_{th} \qquad 3.12b$$

where P_{th} is the threshold for the pressure to overcome the radial elasticity of the bladder for expanding, K_p is the linearized equivalent parallel passive elastic constant for the shearing force of the bladder material and shell threads, and $nl(\cdot)$ is the non-linear term due to the non-perfect cylinder while the actuator is at its extreme length (Fig.3.9a). The first two product terms in Equ.3.12a can also be expressed as

$$F = K_g (P' - P_a) (L - L_{min}) + F_a \qquad 3.13$$

where $P_a = P_{th} - K_p / K_g$, and $F_a = K_p (L_{min} - L_o)$. To experimentally estimate these parameters, 10 points of hypothetically static tension-length-pressure pairs are sampled from the results of quasi-static experiment and fit into Equ.3.13 (Fig.3.9b). The parameter optimization gives K_g = 4.66 N/cm·bar, P_a = 0.062 bar, L_{min} = 9.91 cm, and F_a = -16.0 N. Also, P_{th} and K_p can be estimated by knowing L_o = 14.0 cm, which yields P_{th} = 0.903 bar and K_p = 3.92 N/cm. Notice the K_g is very close to the simulation value (4.61 N/cm·bar) of the theoretical model. The non-linear term only becomes significant when the actuator is extremely short or extremely long, usually this is out of regular operating range, and will not be discussed further.

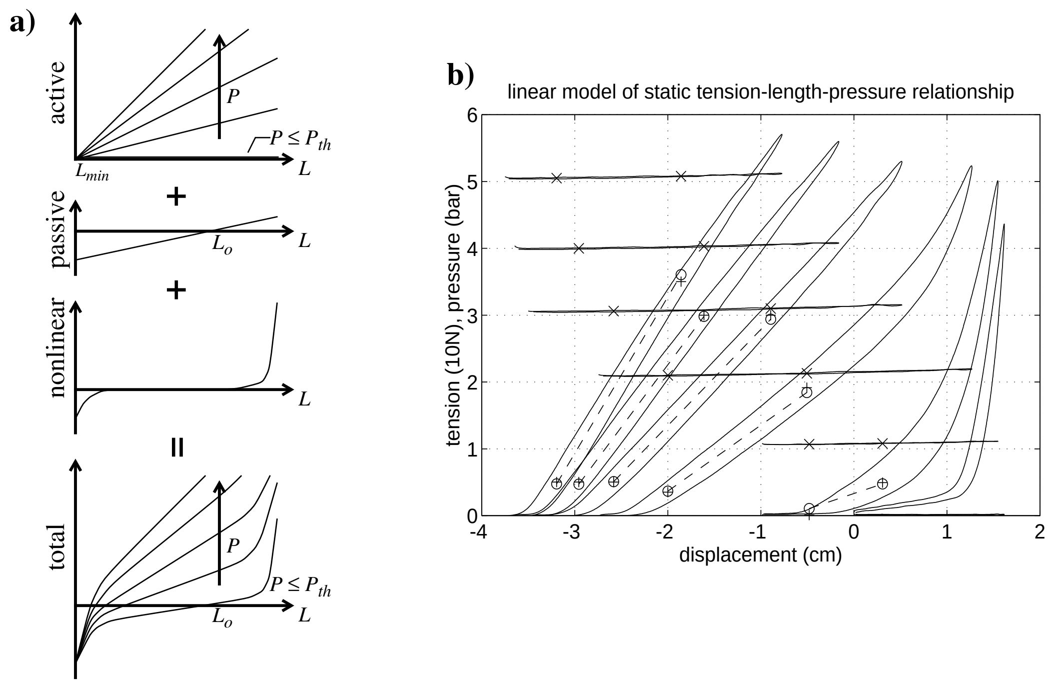

Fig.3.9 a and **b** Static model of McKibben actuator. **a** Total tension is summation of active term, passive term, and non-linear term. **b** Parameters of linearized model are optimized with 10 tension-length-pressure sample points from experimental data of Fig.3.3a. **x**, sampled pressure; **+**, sampled tension; **o**, simulation tension.

3.5.2. Quasi-static and dynamic characteristics

It has been shown that there is hysteresis in the tension-length cycle, and that the dominant friction is the frequency insensitive Coulomb friction, which is caused by the contact between the bladder and the shell, between the braided threads and each other, and the shape changing of the bladder. The history dependence makes the friction difficult to predict precisely, especially after the actuator is attached to artificial bones with curving shape. As a result, it is suggested to add a typical friction value (e.g. ± 2.5 N, positive for lengthening, negative for shortening) to the hypothetically static equation (Equ.3.12a or 3.13 and 3.12b) if a simple friction model is sufficient.

3.6. Discussion

In the following, comparisons will be given between the McKibben muscles and biological skeletal muscles in terms of static and dynamic mechanical properties. Selected properties of the supplementary pneumatic elements will also be evaluated.

3.6.1. Static properties: tension-length-activation and output work

The general shape of the tension-length curve of the actuators is a monotonic increasing function of the length. For the tested polyester shell actuator, the tension reaches zero when the length is shorter than 0.69 L_o (L_o = 30.5 cm), and becomes very stiff when the length is longer than 1.02 L_o. Between these two points, the stiffness is about constant with a typical value of 28.6 N/cm (871 N/L_o) at 5 bar, and is approximately proportional to the pressure with some offset. The maximum tension is 291 N at 1.02 L_o and 5 bar. The integration of the tension within 0.69 to 1.02 L_o is 48 NL_o, which is the maximum output work per each mechanical cycle.

In order to calculate the stiffness and tension intensities per unit cross section area and the work per unit volume, the external cross section area at maximal shortening is used, because this is the maximum cross section area which the actuator should be allowed to occupy in a limb segment. For the polyester shell actuator, the cross section area is 2.54 cm^2 at 0.69 L_o, which yields the stiffness intensity of 343 N/$L_o cm^2$, the maximum tension intensity of 115 N/cm^2, and the work per cycle per unit volume of 0.19 J/cm^3.

The above properties of the four tested actuators are listed in Table 3.1. The diameter ratio of the internal bladder and the external shell, and the way that the threads form the external braided shell of the actuators influence most differences between the four actuators. The nylon shell actuator consists of smaller bladder to shell diameter ratio and the lowest thread density and thickness shell, which yields the widest 35% moving range, the highest power density per cycle, and the smallest Coulomb friction. On the other hand, the polyester shell actuator consists of the smallest bladder to shell diameter ratio and medium thread density and thickness shell, which yields the second widest 33% moving range and power density per cycle.

For biological muscles, the tension-length relation can be described by the "active tension" with a trapezoidal shape and the "passive tension" with increasing stiffness when

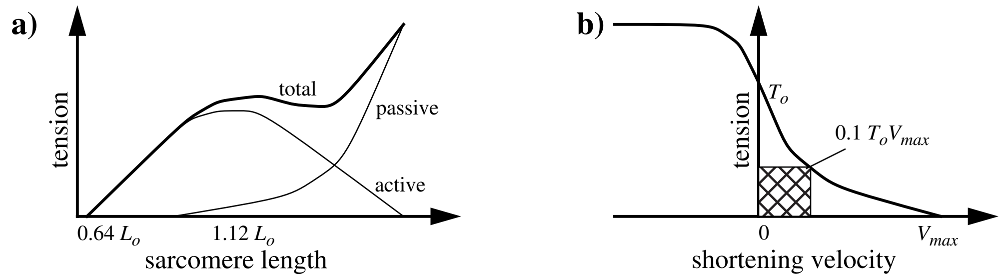

Fig.3.10 a and **b** Mechanical characteristics of biological muscle. **a** Static tension-length relationships. Total tension is summation of active tension and passive tension. **b** Dynamic tension-velocity relationships. Maximum power approximates 0.1 T_oV_{max}.

stretched beyond a certain length (Fig.3.10a). There may be a local maximum of the total tension if the increase of passive tension is less than the decrease of active tension to the length. The zero-tension lengths of the active tension are 0.64 and 1.8 L_o (frog striated muscle, Gordon et al. 1966), however, if we define the dynamic range of biological muscles by the non-negative-slope region of the active tension-length curve, then it is within 0.64 to 1.12 L_o. The maximum tension intensity is about 35 N/cm^2 (Guyton 1986, or 30 N/cm^2 from Gordon 1989), this yields the average stiffness intensity of 73 N/$L_o$cm^2, and the work per cycle per unit volume of 0.13 J/cm^3 by numerically integrating the tension-length curve within the dynamic range.

In summary, the biological muscle can be stretched beyond its resting length much longer than the actuators. Also, the biological muscle can shorten a little more than the actuators. This is a major disadvantage of the actuators. On the other hand, the tension intensity of the actuators is much higher than biological muscles, this is a major advantage of the actuators and yields higher work density and stiffness intensity. Finally, to improve the match to biological muscle static properties, passive parallel and serial elastic elements, which exist in biological muscles, can be added into the actuators if desired.

3.6.2. Dynamic properties: tension-velocity, power, and response time

The tension-velocity relation of the nylon shell actuator, if we do not count the viscosity of the pneumatic circuit, is dominated by a velocity-insensitive Coulomb friction, and the velocity-dependent viscous friction is immeasurable, which yields a very high maximum

Table 3.1 Mechanical properties of McKibben actuators and biological muscles

properties	units	McKibben actuators @ 5 bar				Biological muscles
		Nylon shell	Fiberglass shell	Bridgestone	Polyester shell	
resting length (L_o)	cm	14.0	20.0	14.7	30.5	
dynamic range	L_o	0.75 - 1.1	0.85-1.15	0.78 - 1.02	0.69 - 1.02	0.64 - 1.12
maximum tension	N @ L_o	110 @ 1.1	56 @ 1.15	260 @ 1.02	291 @ 1.02	
stiffness	N/L_o	322	185	1090	871	
max. work per cycle	NL_o	19	8.4	31	48	
cross section area	cm^2@ L_o	0.95 @ 0.75	0.64 @ 0.85	1.8 @ 0.78	2.54 @ 0.69	
tension intensity	N/cm^2	116	88	144	115	35
stiffness intensity	$N/L_o cm^2$	340	290	606	343	73
work density per cycle	J/cm^3	0.20	0.13	0.17	0.19	0.13
coulomb friction	N	2.5	5	5	2.5-6.5	0
maximum velocity	L_o/s	> 6.2				2 - 8 or 20
average power density	W/cm^3	1.1				
peak power density	W/cm^3	> 2.65				0.70
energy efficiency	-	0.32 - 0.49				0.2 - 0.25

velocity in theory. The measured highest peak velocity is 6.19 L_o/s. The measured power per unit volume is 1.1 W/cm^3 in average of half cycle and 2.65 W/cm^3 in peak. For the full activation step response, the total delay time in above experiments is 20 ms, the tension rising time is 30 ms, and the falling time is 53 ms.

On the other hand, the hyperbolic tension-velocity curve of biological muscles (Fig.3.10b) indicates the viscosity decreases when the velocity increases (Hill 1938), and there is no Coulomb friction reported. The typical maximum shortening velocity is 2 L_o/s for slow muscle and 8 L_o/s for fast muscle (Winters 1990) or 20 L_o/s for fast muscle (Gordon 1989). According to Hill's tension-velocity curve, the maximum peak power is about 0.1 $F_{max}\boldsymbol{v_{max}}$ (McMahon 1984). Applying 35 N/cm^2 maximum tension intensity and

20 L_o/s maximum shortening velocity yields maximum peak power per unit volume of 0.70 W/cm^3 for skeletal muscle.

Obviously the tension-velocity relationship of the actuator is not similar to that of biological muscles. Fortunately, the viscous friction is much smaller and thus we can add some parallel viscous elements to simulate biological muscles. In addition, there may be some types of lubricant which can effectively reduce the Coulomb friction. Finally, The response time of motor units and biological muscles motor units, although are not given here, have very wide range, and can be shorter in proximal, fast muscles than in the actuator.

Please also refer to (Chou & Hannaford 1996) for more detail on the analysis and comparison of energy efficiency of the actuators and biological muscle.

3.6.3. Supplementary pneumatic elements

Besides the above considerations, the properties of the supplementary pneumatic elements must be considered, too. The necessary elements include an electro-valve, tubing, and a high pressure gas source.

The Festo MPP-3-1/8 electro-valve used in above experiments is 0.8 kg in weight, 14.5x4.5x4.5 cm^3 in size, and it takes 0.95 A current at 18 V to get 600 l/min flow rate at 6.9 bar input without load. Another tested valve (Animate Systems SARCOS servovalves C100P/80) is 0.1 kg in weight, 8.3x1.9x1.9 cm^3 in size, takes 0.4 A at 5.8 V to get 23 l/min at the same conditions. The flow rate of the former is much higher with the costs of higher control energy and larger size. Although the volume change of the actuator is small, or even zero for isometric condition, we should notice that gas is highly compressible, and the mass changes greatly when its pressure changes. The higher flow rate valve will shorten the system response time, and thus gives a closed loop controller more flexibility to remain stable. However, it is much heavier and bigger than the second valve. This will increase the total weight and size of the system, and also force the designer to avoid putting the valves on moving parts, as a result, long tubing must be used to connect each valve to each independent-controlled actuator. Also, the high control energy will reduce the energy efficiency of the whole system.

Due to the need for remote routing of heavy, bulky valves, there would be many pieces of long tubing in a whole system. The gas viscosity inside tubing decreases as the diameter increases, however, its transversal flexibility decreases at the same time. So, a trade off exists between high flexibility, in order not to disturb movement, and low viscosity, in order not to slow down response.

In order to drive several actuators for many shortening-lengthening cycles, there must be a gas reservoir with very high pressure and acceptable volume if there is no additional energy source. This will waste a lot of energy to compress gas above necessary operating pressure while preparing the high pressure source, and yields a very poor energy efficiency. On the other hand, a compressor with motor or engine may reduce the poor energy efficiency problem, however, it may be heavy and noisy. Finally, a low pressure reservoir with heating chamber may obtain the highest efficiency since the heat is converted directly to actuator's mechanical energy, however, the hot gas may damage the actuator and injure the user.

Please also refer to (Chou & Hannaford 1996) for more detail on the experiment and modeling of the actuator gas dynamics, and the energy efficiency analysis of the actuators.

3.6.4. Short conclusion

The linearized mechanical model of the actuator gave us simple yet accurate descriptions of the actuator and the pneumatic behaviors. A lumped parameter model of the pneumatic system can be found in (Chou & Hannaford 1996). With these two models, a mechano-pneumatic integrated model can be built by cascading the output of the pneumatic circuit model to the input pressure of the actuator dynamic model, and adding a feedback pathway from the length of actuator to its volume (gas capacitance). This may analogous to the mechanical coupling of calcium ion concentration (or active state) in real muscle (Zahalak 1990, Gordon and Ridgway 1990). These models would be very helpful in simulation of single or multiple actuator systems.

The static mechanical features of the actuator are very similar to biological muscles, except the dynamic range is narrower and the tension intensity is much higher. Some parallel and serial elastic elements may be added to fine tune the passive elastic characteristics. On the other hand, some dynamic features may need to be modified to get even closer, for examples: use lubricant to reduce the Coulomb friction and add some viscous material to increase the viscous friction in order to fit the tension-velocity relationship.

The pneumatic system, which provides control and power to the actuator, however, still needs a lot of improvement, for example: we need to find a lighter valve with acceptable flow rate, integrate the tubing into the muscle-bone assembly components to solve tubing length and wrapping problems, and find a light, quiet, and safe gas source with reasonable energy efficiency. Besides the actuator performance, these are also important factors which must be improved in order to implement a feasible muscle replacement system.

IV. Mechanical Muscle Spindle

In this chapter, the mechanical muscle spindle, which will be used in the following experiments, will be briefly described. This work is based on Marbot (1995).

4.1. Introduction to Mechanical Muscle Spindle

One key element of human motion control is the muscle spindle, which is distributed in parallel with tension generating muscle fibers (extrafusal fiber) and is responsible for muscle length and velocity feedback. The main components of this sensor are a stretch sensor and a special muscle fiber. The stretch sensor is connected by a Ia afferent sensory neuron to generate its output signal. The special muscle fiber which connected in series with the stretch sensor (intrafusal fiber) is innervated by a gamma motoneuron (γMN) in the central nervous system to change the spindle's resting length, stiffness, and viscosity. This in turn, changes the offset and the gain of the Ia afferent output. In order to emulate this sensing feature in the anthroform systems, the mechanical muscle spindle (mechanical spindle for short) was built as a replica of the biological muscle spindle by Marbot in 1995.

4.2. Block diagram of mechanical spindle

Similar to the biological muscle spindle, which consists of a stretch sensor and an

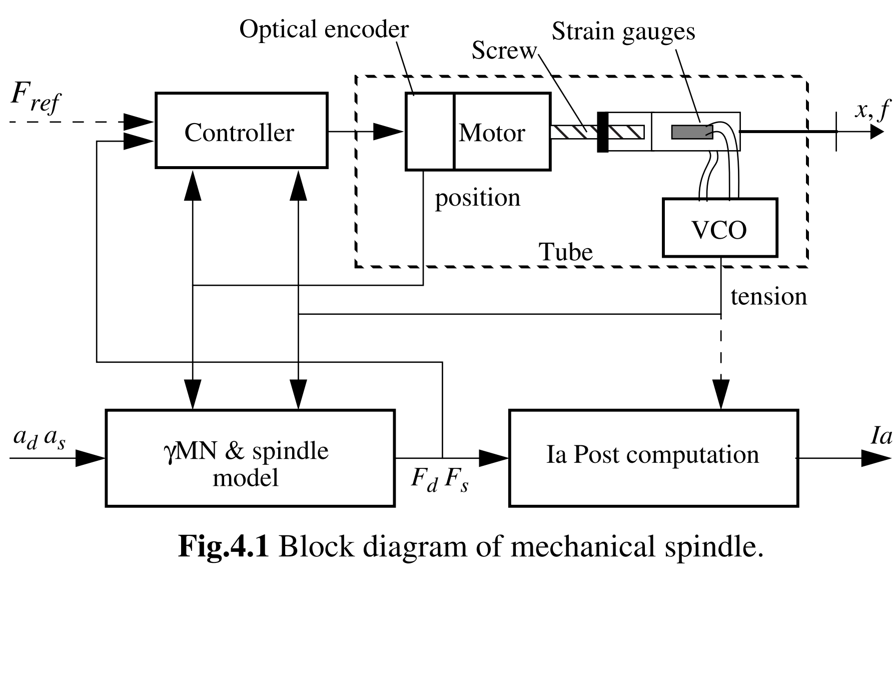

Fig.4.1 Block diagram of mechanical spindle.

actuator, the mechanical spindle consists of a strain gauge tension sensor and a small motor with angular position optical encoder. The block diagram of the mechanical spindle is shown in Fig.4.1. The tension-length-activation relationship of the intrafusal fiber is emulated by feeding back the tension signal from the strain gauge and the position signal from the optical encoder to perform closed loop control. The Ia afferent signal is derived from the actual tension or emulated tension.

4.3. Emulated biological muscle spindle model

The normalized tension-velocity model of the intrafusal fiber implemented in the mechanical spindle is a piecewise hyperbolic function based on Schaafsma's mathematical model of spindle response (Schaafsma et al. 1991). It is:

$$F_{v_i} = \begin{cases} \dfrac{1 + V/V_{max_i}}{1 - V/kV_{max_i}} & \text{if } V \le 0 \\ e_i - (e_i - 1)\dfrac{1 - V/V_{max_i}}{1 + h_i V/k_i V_{max_i}} & \text{if } V > 0 \end{cases} \qquad 4.1$$

where the V is the derivative of the fiber length, and the subscript i is s if the spindle is excited by static type of γMN or d if by dynamic type. Typical shapes of the tension-velocity curves are shown in Fig.4.2 c and d, where two set of parameters are applied under static or dynamic type of γMN excitation, respectively.

The original tension-length model of the intrafusal fiber used in Marbot's experiments with the mechanical spindle alone is an exponential function. However, when attached to the artificial muscle, the Ia afferent signal was very easy to reach either zero or maximum with the exponential model. This undesired result is due to the difference between the tension-length relationship of the spindle model and the actual actuator. This saturation effect will also occur even if a biological muscle were combined with the mechanical spindle since the tension-length relationship of the biological muscle is not an exponential function. Based on experience, a spindle model which matches the tension-length relationship of the actuator can best keep the Ia afferent output from saturation and

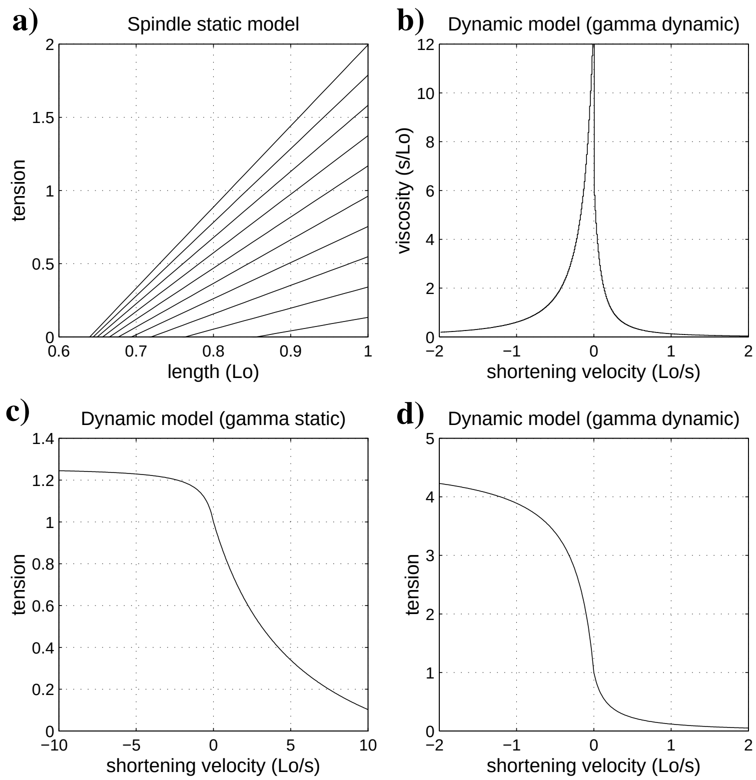

Fig.4.2 a to **d** Static and Dynamic model of muscle spindle. **a** Tension-length relationship. **b** Derivative of tension-velocity curve in **d**. **c** and **d** Tension-velocity relationships with gamma static and dynamic excitation respectively.

effectively provide length and velocity information of the actuator. As a result, a linear model, which is much closer to the actuator tension-length relationship, was chosen here:

$$F_{p_i} = K_{p_i}(L - L_{min_i}) + F_{min_i} \qquad 4.2$$

$$F_{a_i} = K_{a_i} a_i (L - L_{min_i}) \qquad 4.3$$

where the F_p is the passive tension, and F_a is the active tension. This is shown in Fig.4.2a.

Finally, the Ia afferent output is:

$$Ia = r_s(F_{a_s} F_{v_s} + F_{p_i}) + r_d(F_{a_d} F_{v_s} + F_{p_d}) \qquad 4.4$$

V. The Anthroform Arm and Testing Elbow

5.1. The Anthroform Arm

The term "anthroform" is defined to describe a robotic arm in which all aspects of its design are specified in terms of emulation of the corresponding functions of the human arm.

The Anthroform Arm implemented in this project consists of elbow and shoulder joints, scapula, humerus, radius and ulna bones, and 13 single or multiple actuator muscles. The bones were molded by Dr. Jack Winters of Catholic University of America from human cadaver bones with epoxy and fiberglass, and fitted with commercial surgical total-replacement joints (Fig.5.1).

The McKibben pneumatic actuators were used as the artificial muscles. The origin and insertion points of the actuators were based on the anatomy of the human arm (Snell 1980). On some muscles, the attachment points are spread widely. In these cases, appropriate

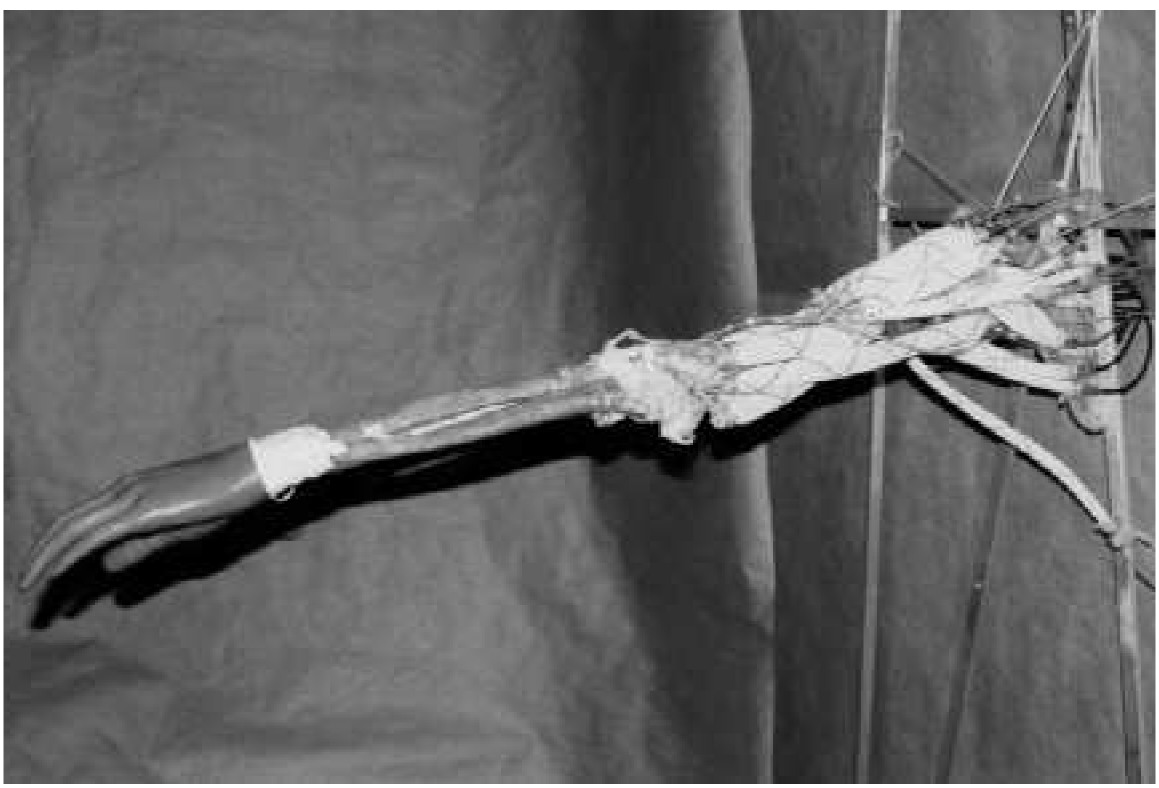

Fig.5.1 The Anthroform Arm.

Table 5.1 Actuators across shoulder and elbow joints.

muscles across shoulder joint		min L (cm)	max L (cm)	# of actuat.	[1]max. tension (N)	[2]desired tension (N)	[3]desired tension (N)	function						
								flex.	ext.	add.	abd.	m.r.	l.r.	stab.
deltoid	(ant.)	12	18	2 L[5]	220	158		x		x		x		
	(mid.)	12.5	17	4 L	440	474	910				x			
	(post.)	15	22	2 L	220	135			x	x			x	
pectoralis major		15	25	1 L	110[4]	472	480	x		x		x		
subscapularis		11.5	14	3 L	330	339	470					x		x
supraspinatus		9	14	1 L	110	158	180				x			x
infraspinatus		11.5	14	2 L	220	203	330						x	x
teres minor		8	11	1 L	110	90	100			x			x	x
teres major		9	14	2 L	220	203	350		x	x		x		
latissimus dorsi		15	25	1 L	110[4]	200	300		x	x		x		
coracobrachialis		8.9	15.9	1 S[5]	56	45	88	x		x				
triceps b.	(long)	23	31	1 L	110									
biceps b.	(long)	26	36	1 S	56			x						
elbow joint								flex.	ext.			pro.	sup.	
triceps brachii	(long)	23	31	1 L	110				x					
	(lat.)	18	24	1 L	110	407			x					
	(med.)	15.2	20	2 L	220				x					
biceps brachii	(long)	26	36	1 S	56	113	220	x					x	
	(short)	22.5	37.5	1 S	56			x					x	
brachialis		14.9	19.5	2 L	220	316		x						
brachioradialis		19.5	30.5	1 S	56	45		x				x		
pronator s.												x		
pronator t.												x		
supinator													x	

Note:

1. Max. tension is estimated based on experimental data, actual geometry and material of the actuators.
2. Desired tension is estimated based on anatomical data of Wood et al. (1989) and 35 N/cm2 of human muscle strength.
3. Desired tension is estimated based on anatomical data of van der Helm (1991) and 35 N/cm2 of human muscle strength.
4. Only part of muscle fibers are emulated.
5. ‘L’ indicates nominal 1/2” ϕ actuator; ‘S’ indicates nominal 1/4” ϕ actuator.

points were chosen for the actuators to produce the motion ranges as close as possible to anatomical data. The length of each actuator was also designed individually based on the real muscle length.

In addition, since the cross sectional areas of human arm muscles vary greatly, each artificial muscle was designed to combine different numbers and sizes of actuators. The functions and some mechanical parameters of the human arm muscles which are emulated by the artificial muscles are given in Table 5.1

The Anthroform Arm has successfully performed most of the shoulder and elbow joints functions under open loop control, which include shoulder joint adduction, abduction, medial and lateral rotations, and elbow joint flexion and extension (Hannaford et al. 1994).

5.2. The Testing Elbow and Experiment Setup

In order to measure the motion dynamically, and integrate the mechanical muscle spindle and force sensors to perform closed loop control, a robotic arm, called the testing elbow, was implemented based on the experience obtained from the Anthroform Arm. The

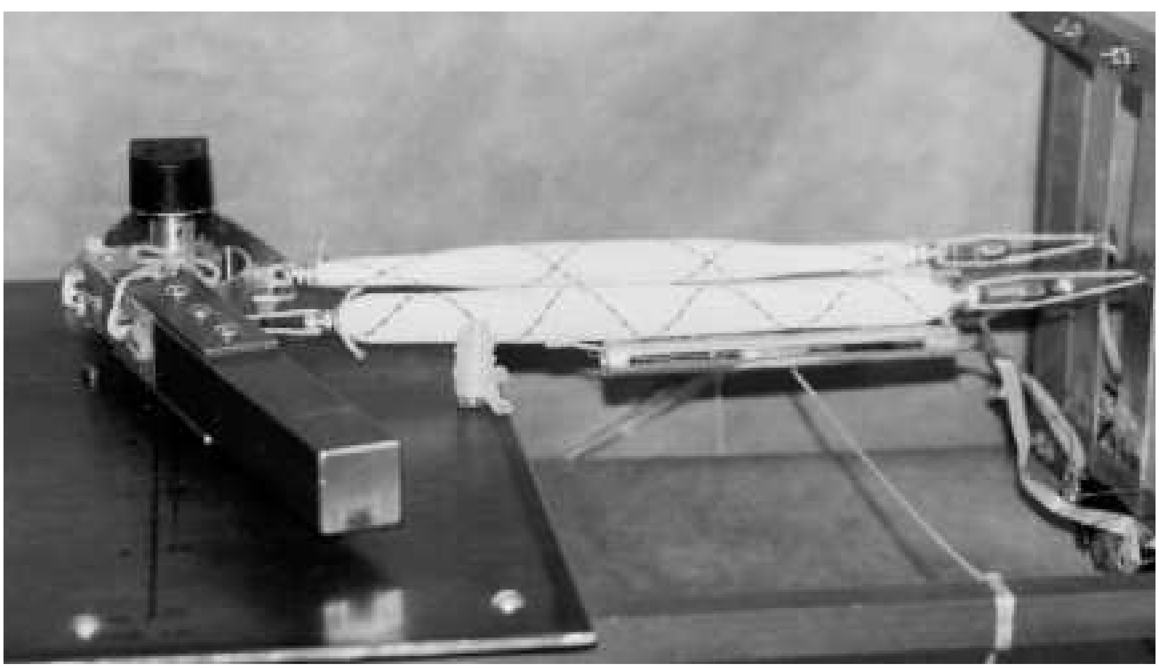

Fig.5.2 The Testing Elbow.

testing elbow consists of an equivalent forearm segment and two McKibben muscles, each attached in parallel with a mechanical muscle spindle and in series with a force sensor. The two McKibben muscles act as elbow flexor and extensor (Fig.5.2).

Electrical control signals sent from the neural controller regulate the output pressures of the electro-valves, which in turn control the mechanical behavior of the actuators. The sensory signals are fed back to the neural controller as Ia and Ib afferents.

The testing elbow is also attached to a dynamic testing system at the elbow joint to form a test bed (Fig.5.3). The dynamic testing system consists of a personal computer (PC), a torque motor, an angular position optical encoder, and various sensors (some of which are overlapped with the afferent signals).

For practical reasons, the inertia of the testing elbow and the strength of the artificial muscles are scaled down by a factor of 3 to make the test bed smaller and also to reduce the

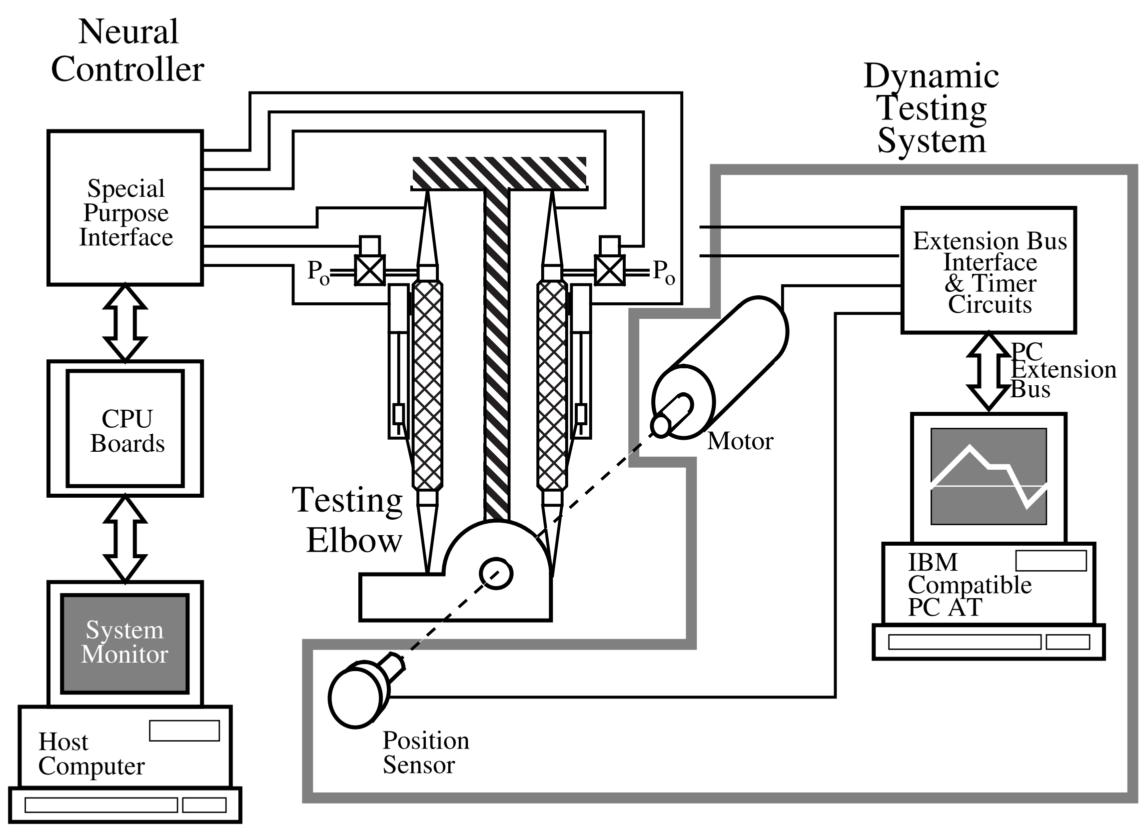

Fig.5.3 Block diagram of elbow test bed, which includes neural controller, testing elbow, and dynamic testing system.

power requirement of the motor. As a result, the actual inertia of the testing elbow is 0.02 Nm s^2/rad (0.06 before scaling in Allum & Young 1976).

While the PC performs mechanical data acquisition, the neural controller itself performs neural activity data acquisition. The efferent signals sent to McKibben muscles are assumed to have the same timing and relative amplitude characteristics as spatially summed and rectified EMG. The activities of the neural network elements and forearm mechanical variables were recorded during experiments and will be shown and analyzed in the following chapters.

VI. Spinal Reflex Neural Circuitry

The spinal segmental neural circuitry is believed to play the major role in low latency reflex response, which, for example, is involved in posture maintenance against external perturbation (Fuchs 1989). It is also called spinal reflex circuitry in this dissertation. Based on physiological discoveries (Binder 1989b, 1989c), the most well studied neurons in the spinal reflex circuitry include alpha motoneurons, gamma motoneurons, muscle spindle Ia afferents, Golgi tendon organ Ib afferents, Ia inhibitory interneurons, Ib inhibitory interneurons, and Renshaw cells (Fig.6.1). The functions of these neurons and their connections will be implemented in the neural controller and applied to the testing elbow to perform experiments in the next two chapters.

In the following, the popularly believed functions and connections of the above spinal neurons will be described. I have no intention to dispute the structure of the spinal circuitry.

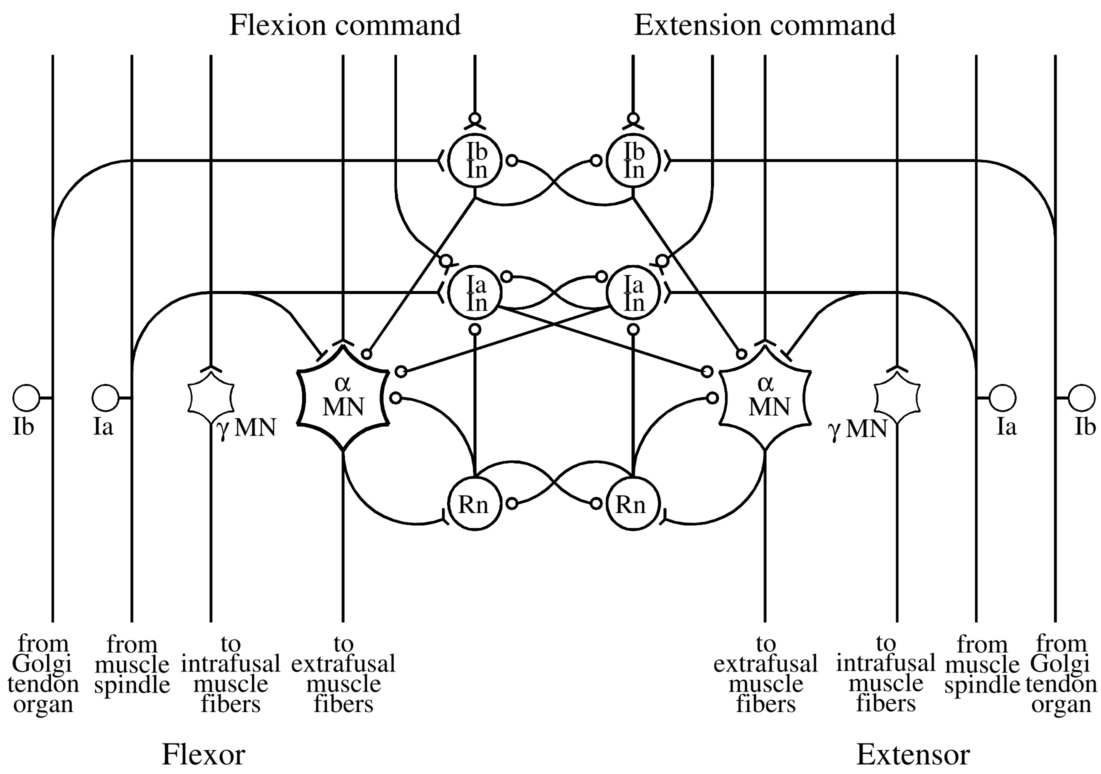

Fig.6.1 Spinal segmental reflex neural circuitry. Circuitry consists of α and γ motoneurons (MN), Ia and Ib afferents, Ia inhibitory (IaIn) and Ib inhibitory (IbIn) interneurons, and Renshaw cells (Rn), with descending pathways connected to all MNs and interneurons. Terminals with line segments or open circles represent excitatory and inhibitory synapses respectively. Combination of above symbols (descending inputs) indicates pathways which may include more than one type of pre-synaptic neuron.

Instead, the effects of changing its structure and parameters will be demonstrated and analyzed in the experiments.

6.1. The Motoneurons and Efferent Pathways

The alpha motoneuron (αMN) and the gamma motoneuron (γMN) are two major types of neurons which directly innervate the biological actuators, the muscles, through their efferent axons to initiate muscle contraction. There are also two types of skeletal muscle fibers. The one innervated by the αMN, called extrafusal fiber, is the type which generates usable tension against load. The other, innervated by the γMN, called intrafusal fiber, is the fiber type which changes the reference length, stiffness and viscosity of the muscle spindle, and in turn modifies the offset and gain of the spindle sensing (Binder 1989b). In the rest of this dissertation, the term "muscle", if not specified, will indicate the extrafusal fibers.

The signal propagation speed through motoneuron axons is about 100 m/s (Binder 1989a). This will introduce several milli-seconds of propagation delay in human which depends on the distance of the innervated muscle to the spinal segment.

6.2. The Sensory Neurons and Afferent Pathways

The muscle spindle Ia afferent and the Golgi tendon organ (GTO) Ib afferent are believed to be the two most important feedback pathways in short latency reflexes with the fastest propagation speed among various types of mechanical afferents, about 90 m/s (Binder 1989b).

The muscle spindle, as mentioned in Chapter 4, is the muscle length and velocity sensor with variable reference length, stiffness, and viscosity which is controlled by the intrafusal muscle fibers. By properly cooperating the intrafusal and extrafusal muscle fibers through αMN and γMN, the high sensitivity and wide dynamic range of the sensing features can be achieved simultaneously (Marbot 1995). The fastest reflex response is achieved by the Ia to αMN excitatory monosynaptic pathway. There is also a pathway from the Ia afferent through spinal interneuron, called Ia inhibitory interneuron, to antagonist αMN. Both pathways provide negative length and velocity feedback.

On the other hand, the GTO is the tension sensor which attaches in series to extrafusal muscle fibers. There are pathways from the Ib afferent through two or more spinal interneuron to the homonymous and synergistic αMNs. These interneurons consist of both excitatory and inhibitory neurons. To emulate part of these pathways, an equivalent neuron, called Ib inhibitory interneuron (IbIn), is involved. This provides negative tension feedback. Unlike the muscle spindle, the role of the GTO Ib afferent has not found agreement among physiologists (Gandevia & Burke 1992) (Loeb 1987) (McCrea 1992). One idea suggested that the Ib afferent is only activated when muscle tension is very high, and is responsible to keep the muscle from overloading. Another suggested that the Ib afferent is very sensitive to the "active force" of the muscle fiber it connects, and is responsible to force control tasks. Another suggested that the Ib afferent is part of the flexion reflex afferent system.

There are more types of sensory afferents, spinal interneurons, and more complex synaptic connections have been found. However, we must limit our scale in order to finished this study in the limited time.

6.3. The Spinal Interneurons

Ia inhibitory interneuron (IaIn), Ib interneurons, and Renshaw cell (Rn) are three types of spinal interneurons which have been heavily studied to show their close relationships to the αMN and Ia and Ib afferents. While the IaIn forms the inhibitory synapse to antagonist αMN, the agonist and antagonist IaIn also form synapses to each other to perform reciprocal inhibition (Binder 1989c). Similar reciprocal inhibition has also been found in the IbIn (Brink et al. 1983) (McCrea 1986) an in the Renshaw cell (Binder 1989c). The Renshaw cell also has excitatory input from the αMN, and in turn inhibits the αMN and IaIn (Binder 1989c) (Shoemaker & Hannaford 1994) (Windhorst 1989).

6.4. Descending Pathways

There are many ways descending neural signals influence the spinal neural circuitry. In this study, only the synaptic inputs to the motoneurons and the IaIn and IbIn are considered. Through these inputs, the αMN receives the main command from the higher level central nervous system to voluntarily control the contraction of the extrafusal muscle fibers. The γMN receives a reference signal to control the muscle spindle to cooperate with the extrafusal muscle fibers.

On the other hand, the patterns of the descending signals to the spinal interneurons have not been well studied yet. A combination of these descending signals for voluntary fast movement will be suggested in Chapter. 8.

6.5. Implementation

The functions of the above spinal reflex circuitry were implemented by a software program, Nnet, running in the Anthroform Arm DSP computer system (MacDuff et al. 1992) to form the neural controller. The neural network kernel of the Nnet updates the neural activity states and neural outputs every milli-second according to the command and sensor inputs, the synaptic connections, and the neural functions. The software architecture allows each type of neuron to have an individually defined function to control its behavior, and each individual neuron can have its own set of parameters to fine tune its response based on physiological evidence if available.

Typical neural functions implemented in the neural controller include artificial delay, post-synaptic weighted summation, infinite impulse response digital filter, and nonlinear transformation (Fig.6.2). The neuron functions of the gamma motoneurons and the Ia afferent neurons were described in Section 4.3.

The z-transformation of the digital filter in each neuron has at least a zero at -1 (500 Hz), which is at a half of the sample (update) frequency. In addition, to implement the adaptation phenomena of αMN (Shoemaker & Hannaford 1994), the αMNs also have a

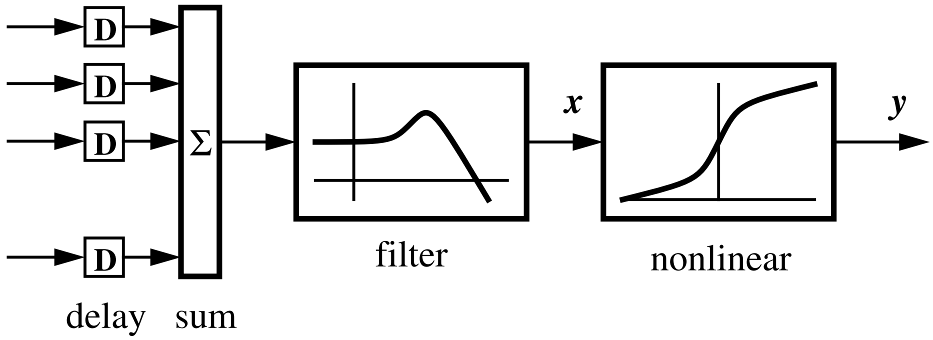

Fig.6.2 Typical Neural Functions Emulated by Neural Controller.

zero at 0.974 (-26.0 rad, 4.14 Hz) and a pole at 0.905 (100 rad, 15.9 Hz).

The non-linear transfer function in alpha motoneurons and interneurons is:

$$y = max\left(0, k_y\left(\frac{2}{1+e^{-2k_x(x-x_o)}} - 1\right) + y_o\right) \quad 6.1$$

where k_x and x_o are input gain and offset; k_y and y_o are output gain and offset. Typical value is 1 for k_x and k_y, and 0 for x_o and y_o. In Ib inhibitory interneurons, k_x=2, k_y=0.5, x_o=0.5, y_o=0.5. Please note that there are some degrees of redundancy for assigning the gain among the synaptic weights, filter, and the non-linear transformation. This will give us more freedom to chose an optimization or learning algorithm in the future. Initially, the DC gain of the filter, and the $dy/dx|_{x=0}$ of the non-linear transformation are designed to be 1 in order to highlight the relative importance of each synaptic weight. However, this is not the case for the afferent neurons and the descending command.

Due to the difficulty of converting data from groups of biological neurons to emulated neurons, several assumptions are defined as the starting point to assign the synaptic weights. 1) A value of '1' is assigned to the synaptic weights where the source is the descending command, or the synapses are the sole excitatory input of the destination neurons. These include the descending input to γMN, IaIn, and αMN, αMN to Rn synapses, and the extensor Ib to IbIn synapse. A weight of '1.4' is assigned to the flexor Ib to IbIn synapse due to the consideration of different moment arms between the flexor and extensor muscles 2) A weight of '-1' is assigned to the synaptic weights where the source is the descending command and the destination neurons will inhibit the agonist αMN. This includes the descending input to IbIn. 3) A weight of ‘-0.5’ is assigned to the synaptic weights which performed reciprocal inhibition. These include the reciprocal IaIn’s and Rn’s. The synaptic weights of the reciprocal IbIn’s are ‘-0.25’ since the importance and function of the these connections are not very clear yet. 4) The synaptic weights of the Ia, IaIn, and IbIn to αMN are assigned based on the comparison of reflex experiments between the neural controller-testing elbow system and physiological results. Experiments on the effects of these synapses will be demonstrated and discussed in the next chapter. The synaptic weights of the source-destination neuron pairs are listed in Table.6.1.

The network structure definition and the parameters of the neurons and synapses can be stored in files in advance and down loaded to the DSP through the interpreter of the Nnet

Table.6.1 Synaptic weights of spinal neurons.

Source	Dest.	Flexor					Extensor				
		γMN	IbIn	IaIn	Rn	αMN	αMN	Rn	IaIn	IbIn	γMN
Flexor	descend	1	-1	1		1					
Flexor	Ib		1.4								
Flexor	Ia			0.25		0.25					
Flexor	IbIn					-0.5				-0.25	
Flexor	IaIn						-0.5		-0.5		
Flexor	Rn			-0.25		-0.25		-0.5			
Flexor	αMN				1						
Extensor	αMN							1			
Extensor	Rn				-0.5		-0.25		-0.25		
Extensor	IaIn			-0.5		-0.5					
Extensor	IbIn		-0.25				-0.5				
Extensor	Ia						0.3		0.3		
Extensor	Ib									1	
Extensor	descend						1		1	-1	1

when needed. They can also be created, modified, or deleted by the user or by an external program during run time. The descending commands can be either pre-programmed and stored in the DSP or transmitted from a host computer during run time. Finally, some or all of the neural activities in the network can be transmitted to the host computer for recording and analysis. Please refer to Appendix A to C for more information on the neural controller software and operating environment.

VII. Posture Maintenance Experiments

In the following, a series of experiments regarding to posture maintenance will be involved. According to the bottom up approach as mention in Review, first the intrinsic mechanical features of the musculo-skeletal system, the devices, will be described. After this, Ia afferent and Ib afferent feedbacks will be added to form simple closed loop control. Finally, the complete spinal reflex circuitry described above will be integrated into the system to resemble Lacquaniti et al. experiment (1982). In order to reveal the effects of neural components and parameters, comparative experiments with modified network configuration and parameters will be demonstrated, too.

7.1. Open Loop Stiffness Control with Muscle Co-contraction

In this experiment, the actuator pressure (analogous to muscle activation level) was kept as constant as possible while cyclic displacement or torque patterns (0.25 Hz) were

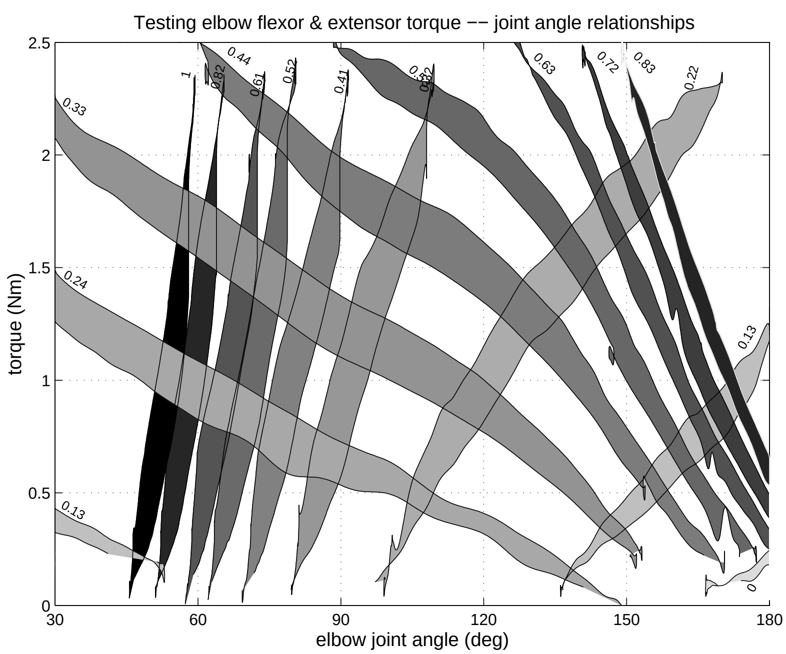

Fig.7.1 Open loop torque-angle-activation relationships for elbow flexor & extensor. Joint equilibrium angle is the intersection of two curves, one for each actuator of corresponding activation level. Normalized muscle activation level is indicated on top of each curve with 1 corresponding to 100 psi (6.9 bar). Joint stiffness, which is the sum of stiffness of two muscles, increases when muscles co-contract.

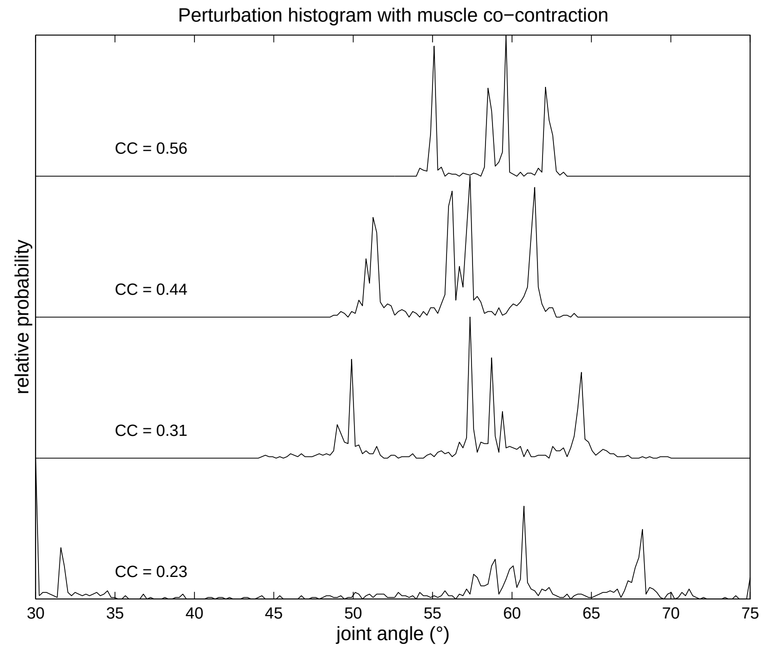

Fig.7.2 Elbow joint angle histograms in response to constant amplitude disturbing torque steps with different muscle co-contraction levels (CC). Narrower width of histogram indicates the joint stiffness is higher.

applied to the joint. The neural controller was not involved at this point. The relationships between elbow joint torque, displacement, and actuator pressure of the flexor and the extensor are superimposed in Fig.7.1. The hysteresis loop of each curve is caused by the actuator friction and the gas viscosity. The loop direction is clockwise for flexor and counterclockwise for extensor. The joint equilibrium angle will be the intersection of two curves, one for each actuator of corresponding activation level. The stiffness (absolute value of the slope) of each actuator curve increases when the pressure increases. As a result, the joint stiffness, which is the sum of the stiffness of the two muscles, increases when muscles co-contract.

To verify the above point, constant amplitude disturbing torque steps were applied to the elbow with various levels of co-contraction. The angular position was recorded and histograms of the position responses are shown in Fig.7.2. The higher the co-contraction level is, the narrower the histogram of position is. This indicates that the stiffness increases with co-contraction.

7.2. Closed Loop Stiffness Control with Ia or Ib Afferent Feedback

In this experiment, muscle spindle Ia afferent feedback and Golgi tendon organ Ib afferent feedback effects will be demonstrated.

The muscle spindle Ia afferent is sensitive to the length and velocity of human muscle (Binder 1989a). This kind of feedback pathway to muscle activation will increase the stiffness of the mechanical system. The mechanical muscle spindle has been reported to be able to emulate the sensitivity and some non-linear properties of the spindle under isolated testing (Marbot 1995) (Marbot & Hannaford 1993). In this experiment, it will be tested with the flexor actuator of the arm to demonstrate the effect of joint stiffness modification.

In the first part of this section, the neural controller consists of an α motoneuron (MN), a γ motoneuron, and a Ia afferent sensory neuron. Each simulated "neuron" actually represents a pool of physiological neurons. Values for the synaptic weight between Ia and αMN and a constant command signal to the αMN were chosen to achieve the desired

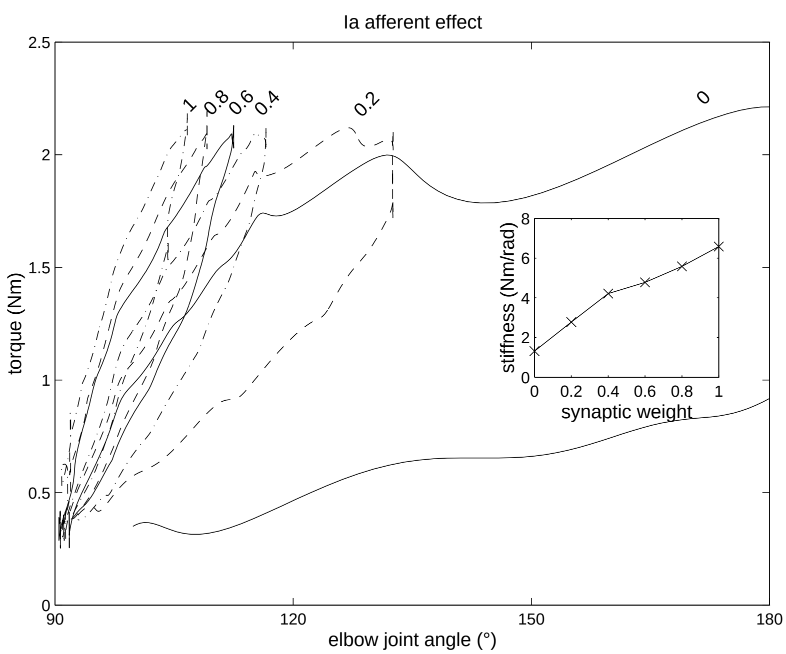

Fig.7.3 Ia afferent effect. Joint angle was recorded while cyclic disturbing torque was applied to the elbow joint. Each curve corresponds to different weight of Ia-αMN synapse. Approximate stiffness vs. synaptic weight is plotted in inset. Joint stiffness increases significantly when synaptic weight increases.

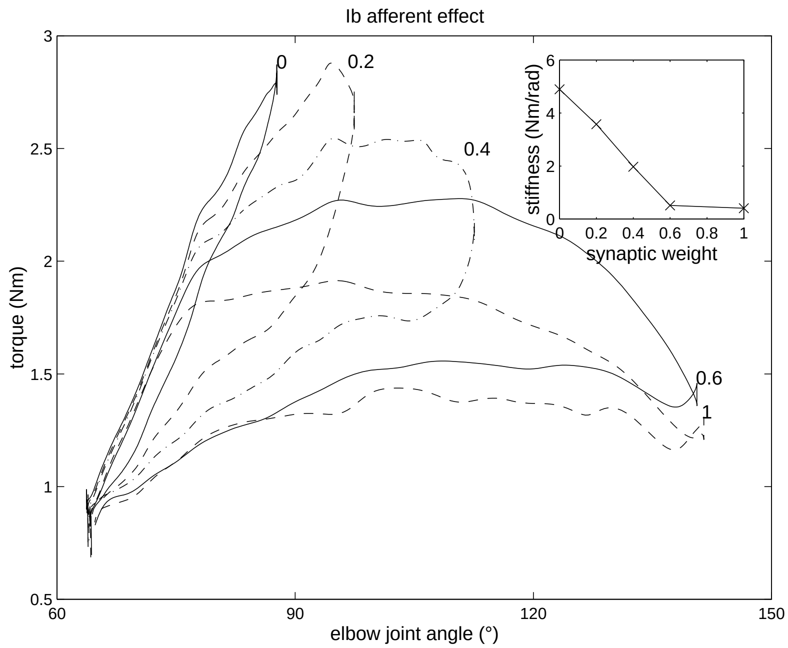

Fig.7.4 Ib afferent effect. Joint torque was recorded while cyclic disturbing angle was applied to the elbow joint. Each curve corresponds to different weight of IbIn-αMN synapse. Approximate stiffness vs. synaptic weight is plotted in inset. Joint stiffness decreases significantly when synaptic weight increases.

operating points to keep the elbow motion in dynamic region. The joint angle was recorded while a cyclic disturbing torque was applied to the elbow joint (Fig.7.3). Each curve corresponds to a different synaptic weight of the Ia-αMN synapse. The relationships of the joint stiffness and synaptic weight are plotted in the inset of Fig.7.3. The joint stiffness increases significantly from 1.4 to 6.6 Nm/rad when the synaptic weight increases.

On the other hand, the Golgi tendon organ senses the tension of its connected muscle fibers (Binder 1989b). The action of this kind of inhibitory feedback pathway will increase the compliance (reciprocal of stiffness) of the system. A strain gauge force sensor was applied to the “tendon” of each actuator to perform this function.

In the second part of this section, the neural network consists of an αMN, a Ib afferent sensory neuron, and a Ib inhibitory interneuron (IbIn). Values for the synaptic weight between IbIn and αMN and a constant command signal to αMN were again chosen to achieve the desired operating points. The joint torque was recorded while a cyclic disturbing angle was applied to the elbow joint (Fig.7.4). Each curve corresponds to a different synaptic weight of the IbIn-αMN synapse. The relationships of the joint stiffness and synaptic weight are plotted in the inset of Fig.7.4. The joint compliance increases significantly from 0.2 to 2 rad/Nm when the Ib inhibitory synaptic weight increases.

7.3. Posture Maintenance with Spinal Reflex Circuitry in Response to Transient Perturbation

In this section, the complete spinal reflex neural circuitry described in the previous chapter is involved in the posture maintenance experiment.

The testing conditions are designed to resemble those described in Lacquaniti et al. in 1982 (Fig.7.5), which demonstrated how different instructions to the human subjects shape the reaction to the same external mechanical load and perturbation. In their experiment, the

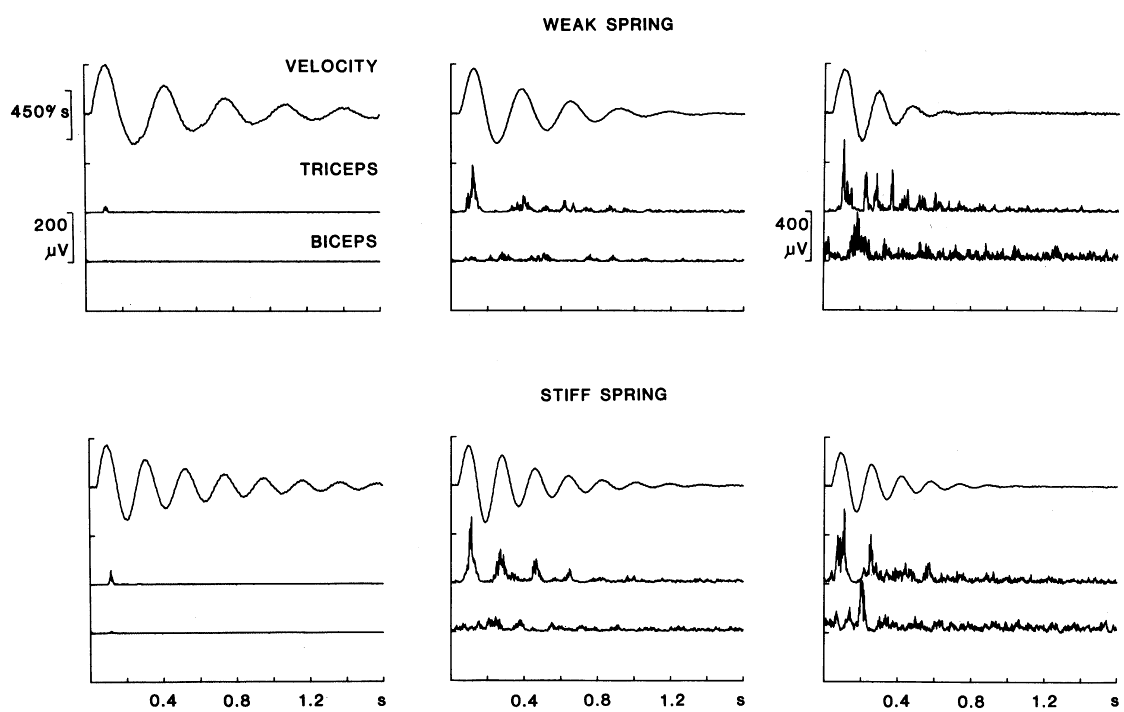

Fig.7.5 Experimental results of Lacquaniti et al. First column corresponds to the task "do not resist", second to "resist", and third to "resist maximally". First trace in each subplot corresponds to forearm angular velocity (flexion is positive). Second and third traces are rectified EMG activities of triceps and biceps, respectively. Perturbation responses were measured with three external viscoelastic loads. (source: Biological Cybernetics, vol. 44: 35-46)

subjects' upper arm was fixed, and their forearm was fitted with damped springs to create viscoelastic loads with three different values. Initially, the forearm and damped spring system was pulled away from its equilibrium angle by a torque motor. Then it was abruptly released and made damped oscillations. The subjects were instructed to perform three motor tasks: 1) "not to resist the perturbations by remaining as relaxed as possible" (refer to "do not resist"), 2) "to apply a moderate amount of force without attempting to control the perturbed position of their forearm" (refer to "resist"), and 3) "to resist the perturbations so as to arrest the forearm oscillations" (refer to "maximally resist"). The results of their experiments showed that the estimated time constant decreases, and the stiffness, damping factor and oscillation frequency increase when the instructed resistance level increases. In another words, the settle time is shorter when the resistance level is higher.

To emulate the different subject instructions, the following inputs were applied as "descending commands" to our spinal level network. For the 1st motor task ("do not resist"), both the α and γ MNs descending commands were set to zero to emulate the "relaxed" condition. For the 2nd task ("resist"), a moderate level of co-contraction command was applied to α and γ MNs to produce 0.6 Nm co-contraction torque from each, oppositely acting, muscle actuator. For the 3rd task, since there was only spinal segmental level control in our system, intentional control to arrest the forearm oscillations is not possible. To substitute this case, a co-contraction level of 1.5 Nm was chosen (refer to "resist harder) to obtained higher resistance without intension.

The viscoelastic load was emulated by the closed loop controlled torque motor with three different position and velocity feedback gains to produce stiffness and damping equivalent to the damped springs used in Lacquaniti's experiments. Note that the medium load has the lowest value of viscosity among the three. Tests without load were also performed for comparison.

As mentioned in Section "The Anthroform Arm has successfully performed most of the shoulder and elbow joints functions under open loop control, which include shoulder joint adduction, abduction, medial and lateral rotations, and elbow joint flexion and extension (Hannaford et al. 1994).", the inertia of the Elbow and the strength of the muscles are scaled down by a factor of 3. In order to compare to Lacquaniti's experiment easier, all of the torque related parameters and measurements will be scaled up by 3 before being reported.

As in Lacquaniti's experiment, the forearm and damped spring system was initially pulled away from its equilibrium angle and then abruptly released making damped oscillation. The transient elbow joint velocity and actuator valve input signals (EMG) are shown in Fig.7.6. Each column corresponds to a different motor task: **i**) "do not resist", **ii**)

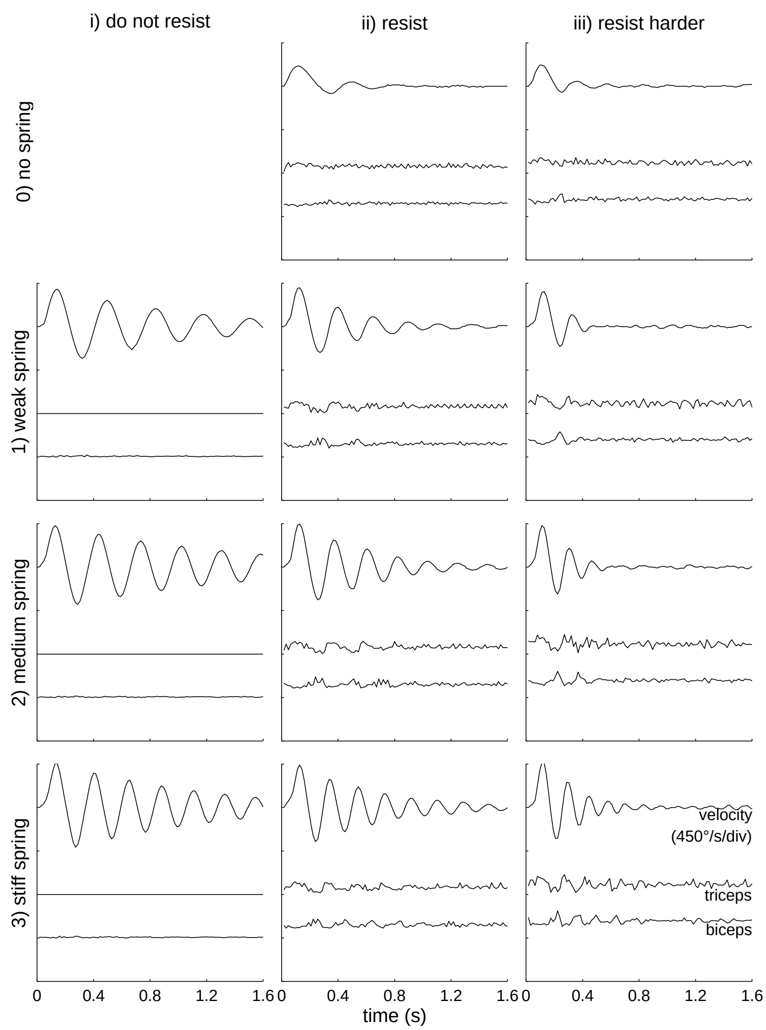

Fig.7.6 Testing elbow transient response with spinal reflex circuitry. Each column corresponds to different motor task: **i**) "do not resist", **ii**) "resist", and **iii**) "resist harder". Each row corresponds to different viscoelastic load: **0**) no load, **1**) weak, **2**) medium, and **3**) stiff spring. First trace in each subplot corresponds to forearm angular velocity (flexion is positive). Second and third traces are analogous to spatial summation of rectified EMG activities of extensor and flexor muscle groups, respectively.

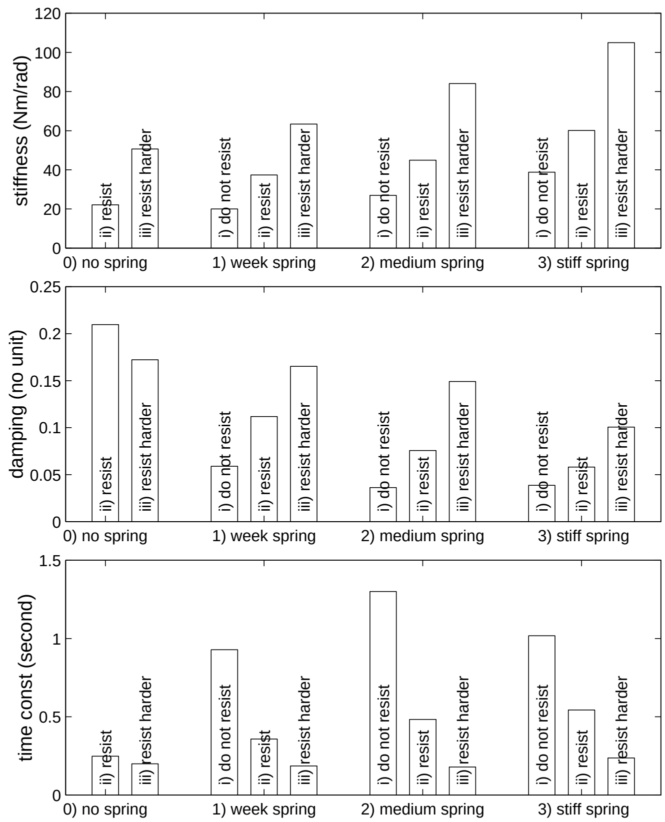

Fig.7.7 Damped oscillation parameters of experiment with spinal reflex circuitry. Time constant, stiffness, and damping factor were calculated from the first four wavelengths of each oscillation.

"resist", and **iii**) "resist harder". Each row corresponds to a different viscoelastic load: **0**) no load, **1**) weak, **2**) medium, and **3**) stiff spring. The parameters of the oscillation (time constant, stiffness, damping factor) were calculated from the first four wavelengths of each oscillation and plotted in Fig.7.7. The results show that the time constant does decrease, and the stiffness, damping factor and oscillation frequency do increase when the resistance level increases. This matches Lacquaniti's experiment very well. However, in the "resist harder" task, the time constant does not decrease as significantly as it does in "maximally resist" task of Lacquaniti's experiment. More detailed discussion will be described later.

The test system allows all neural activities, afferent and efferent signals, and dynamical variables to be recorded. Although complete sets of data were recorded in this experiment, the amount of data is too large to report in this article. Instead, the covariance coefficients of each pair of variables are plotted as circles in a matrix (Fig.7.8). The size of the circle

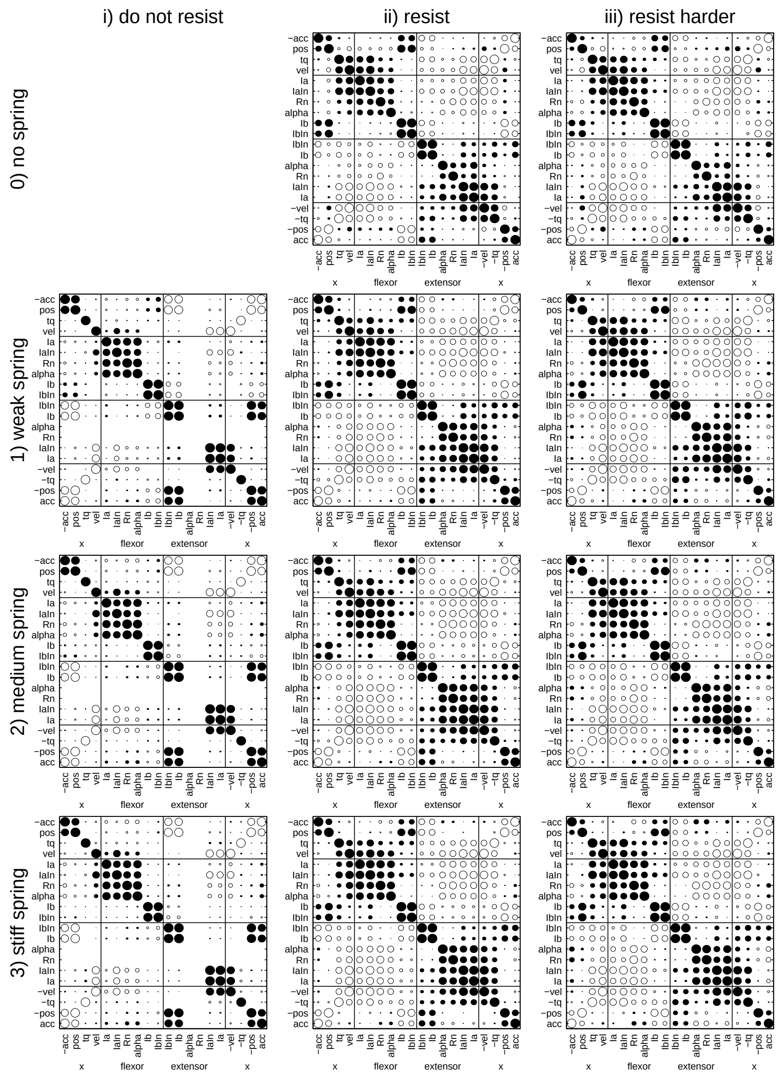

Fig.7.8 Covariance diagrams of experiment with spinal reflex circuitry. Covariance coefficients of each pair of variables, including neural activities and elbow joint mechanical quantities, are plotted as circles. Size of circle represents amplitude of covariance between row and column variables, and color represents sign: black is positive, white is negative. Column and row numbering is the same as defined in Fig.7.6.

represents the amplitude of covariance between the row and column variables, and black indicates positive. The column and row numbering is the same as defined in Fig.7.6. We will call this a covariance diagram. The covariance diagram greatly reduces the amount of data and highlight the points of interests.

By properly arranging the order of the variables, the covariance diagram forms several clusters with large circles and others with small circles. The clusters of larger circles indicate that the variables in the cluster are strongly related to each other (e. g. Ia, IaIn, Rn, and αMN to each other). The clusters of small circles indicate that the variables in the cluster are weekly related to each other (e. g. Ib and IbIn are weakly related to Ia, IaIn, Rn, and αMN). Also, we can find that the positively co-varying pairs are mostly located near the diagonal, while the negative ones are located near the anti-diagonal. This demonstrates the agonist-antagonist nature of the system (e. g. the flexor αMN cluster and the extensor αMN cluster). On the diagonal are trivial covariances of +1. The advantage of the

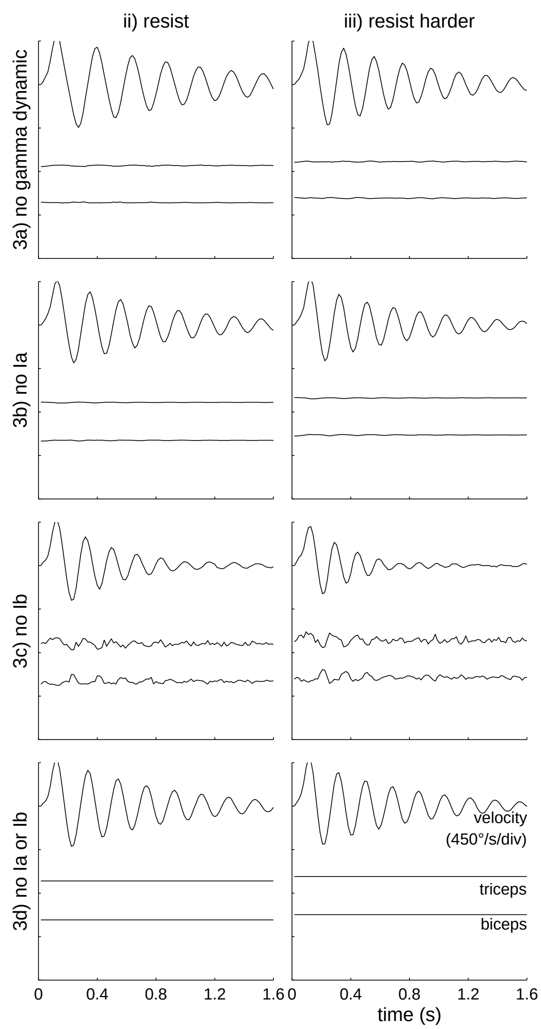

Fig.7.9 Testing elbow transient response with modified circuitry. Each column corresponds to different motor tasks: **ii**) "resist" and **iii**) "resist harder". Each row corresponds to a different, modified, network configuration: **3a**) without γMN dynamic excitation, **3b**) without Ia afferent feedback, **3c**) without Ib, and **3d**) without Ia or Ib. Only the trials with stiff spring are performed. The first trace in each subplot corresponds to forearm angular velocity (flexion is positive). The second and third traces are equivalent to average rectified EMG activities of extensor and flexor muscle groups, respectively.

covariance diagram will be enhanced later.

7.4. Comparative Experiments with Modified Spinal Reflex Circuit Elements

In order to highlight the roles of specific sub-networks of the neural circuitry, another set of experiments were performed similar to the above but with modified neural circuitry. The following configurations, modified from the original circuitry (Fig.6.1), were chosen: 1) without γ dynamic excitation of muscle spindles, 2) without Ia feedback, 3) without Ib feedback, 4) without Ia or Ib feedback, and 5) without αMN activation dynamics.

The transient responses and oscillation parameters are shown in Fig.7.9 and Fig.7.10 respectively. Each column of Fig.7.9 corresponds to a different motor task: **ii**) "resist" and **iii**) "resist harder". Each row corresponds to a different network configuration: **3a**) without

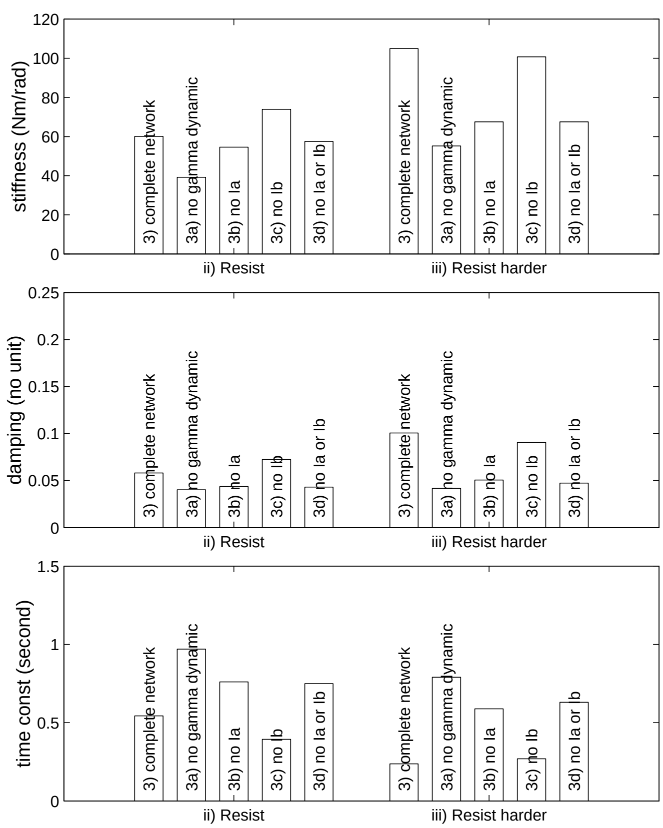

Fig.7.10 Damped oscillation parameters with modified circuitry. Time constant, stiffness, and damping factor were calculated from the first four wavelengths of each oscillation. Parameters for "resist" and "resist harder" tasks with stiff spring of Fig.7.6 (**3.ii** and **3.iii**) are also shown here for comparison.

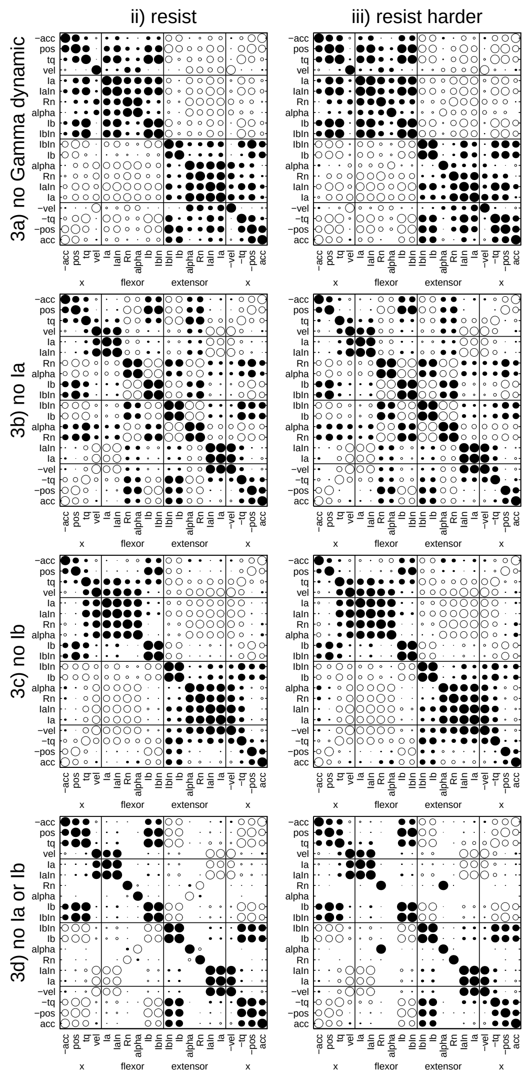

Fig.7.11 Covariance diagrams of experiment with modified circuitry. Notation and column and row numbering is the same as defined in Fig.7.9.

γMN dynamic excitation, **3b**) without Ia afferent feedback, **3c**) without Ib, and **3d**) without Ia or Ib. Only the trials with stiff spring are performed. The result of the tests without αMN activation dynamics was very similar to the tests without γ dynamic excitation and is not shown. In general, the results show that the system stiffness decreases without Ia feedback, and increases without the Ib feedback. Also, the damping factor decreases without either γ dynamic excitation or αMN dynamics. None of these modified configurations can obtain the same disturbance rejection performance (short time constant) as the original network.

The covariance diagram introduced in the previous section is applied here as well and is shown in Fig.7.11. The column and row numbering is the same as defined in Fig.7.9. In order to calculate the covariance, afferent signals were always recorded even if feedback was turned off. For convenience, neurons are classified into three subsystems: α subsystem, including αMN and Renshaw cell; Ia subsystem, including Ia afferent and IaIn; Ib subsystem, including Ib afferent and IbIn. Compared to the previous experiment, only the configuration without Ib feedback has similar covariance diagram patterns. The one without γ dynamic excitation has strong covariance between Ia, Ib and α subsystems. The case without Ia feedback has very low covariance between Ia and α subsystems, but very strong (negative) between Ib and α subsystems. Finally, the case without either Ia or Ib subsystem has very low covariance between different subsystems, and most off-diagonal circles shrink into small dots.

7.5. Stability Experiments

The effects of the network components have been demonstrated in the previous section by modifying the structures of the neural network. Now, the effects of the feedback delay and loop gain on the system stability are demonstrated with the original neural circuitry.

Phase margin and gain margin are two critical factors to determine the stability of a linear system. The phase margin defines the addition amount of phase angle which will make the feedback of the linear system at unity gain frequency to become 180°. This will turn the negative feedback into a positive feedback with loop gain of one, as a. result, makes the system become unstable. The unity gain frequency is the frequency where the feedback loop gain of the system equals one. And the gain margin defines the factor of gain which will make the feedback loop gain at 180° phase lag frequency to become one. These concepts can also be used to analyze a nonlinear system such as the elbow system. In addition, “delay margin” will also be introduced similar to the phase margin for convenience.

In order to estimate system delay margin and gain margin, the system stability were observed while the time delay or loop gain of the Ia feedback pathways were artificially added in addition to their original values. The experiment procedures are the same as in the

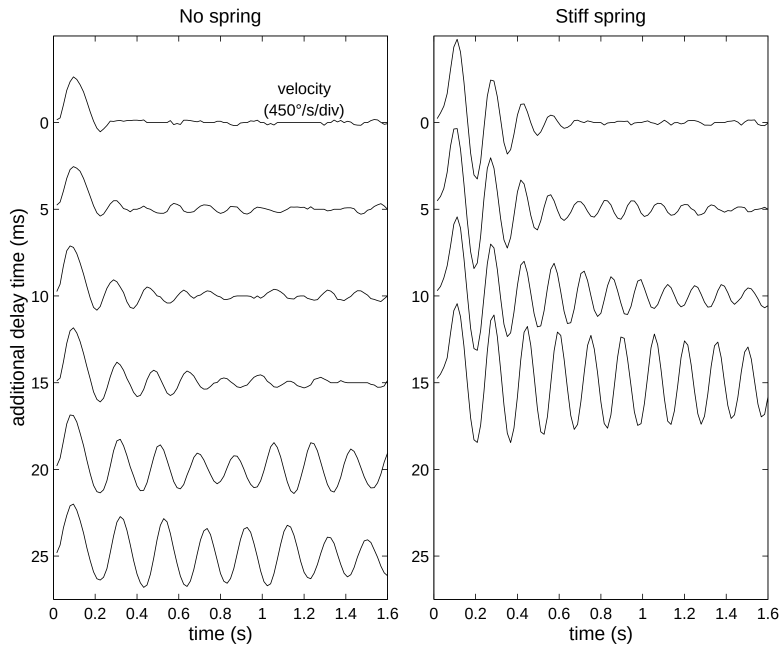

Fig.7.12 Transient velocity responses with additional feedback delay. Feedback loop delay was increased beyond original delay of 17 ms by 5 ms every trial.Additional delay time at which oscillation occurs and oscillation frequency are estimated to be 17 ms and 5 Hz for no load case, and 10 ms and 6.5 Hz for stiff load case.

previous two sections. However, only the "resist harder" task with stiff load or without load are performed.

The nominal delay in the elbow replica and neural controller system is about 17 ms. This total includes 2 ms sensory input and processing, 1 ms monosynaptic neural computation, 1 ms command output, 7 ms pneumatic valve actuation, and 6 ms gas propagation delay. Although additional delay can be generated by the neural controller if desirable, 17 ms is already slightly longer than the physiological data of 15 ms for the tendon jerk reflex time of human biceps brachii (Marsden 1976).

In the delay experiment, feedback loop delay was increased beyond the original delay of 17 ms by 5 ms every trial. The transient velocity response is shown in Fig.7.12. The additional delay time at which oscillation occurs (delay margin), and the oscillation frequency are estimated to be 17 ms and 5 Hz for the no load case, and 10 ms and 6.5 Hz for the stiff load case. The phase margins, which will be derived from the above delay margins and oscillation frequencies, will be discussed in 7.6.7.

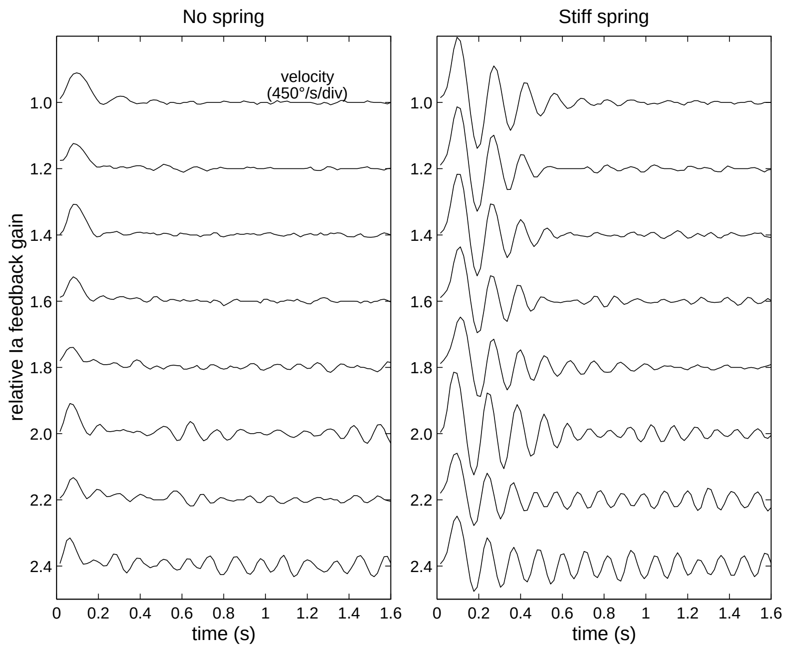

Fig.7.13 Transient velocity responses with increased feedback loop gain. Ia afferent loop gain is increased by 20% in every trial. Gain margins are about 1.8 for both load conditions. Oscillation frequencies are 8.5 Hz for no load and 9 Hz for stiff load condition.

In the loop gain experiment, the Ia afferent loop gain is increased by 20% in every trial. The result is shown in Fig.7.13. The gain margins are about 1.8 for both load conditions. The oscillation frequencies are 8.5 Hz for no load and 9 Hz for stiff load condition. The gain margin and the loop gain function will be further discussed in 7.6.7.

7.6. Discussion

7.6.1. Tools

In the following, we will explain the effects of the system components and the loads from a linear control point of view. This linear model will help us clarify relative roles of co-contraction and Ia reflex activity in maintaining posture. Although the system is nonlinear, a linear model can be used to qualitatively analyze the effects of some system parameters and to conveniently show plausible roles for system components in generating the observed experimental results. Of course we should always keep in mind that the

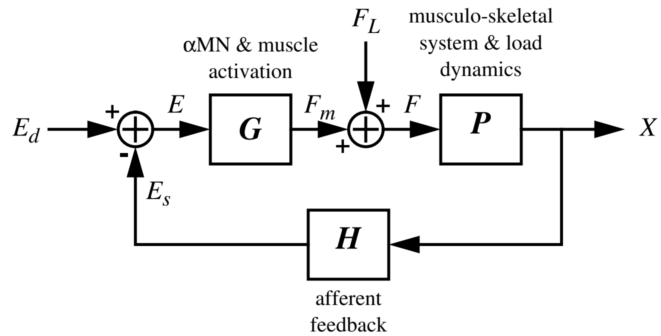

Fig.7.14 Signal block diagram of simplified elbow joint linear model, which includes controller, *G*, plant, *P*, and feedback, *H*.

accuracy of the linear model will decrease significantly when system states are moving away from the current operating point.

The signal block diagram of the linear model, including the controller, *G*, the plant, *P*, and the feedback, *H*, are shown in Fig.7.14. The frequency response from the closed loop joint angle to the perturbing torque will be:

$$\frac{X(s)}{F_L(s)} = \frac{P(s)}{1 + G(s)P(s)H(s)} \qquad 7.1$$

In terms of linear analysis, the frequency response of the α motoneuron and muscle activation dynamics can be approximately expressed as:

$$G(s) = \frac{F_m(s)}{E(s)} = \frac{K_m(x_o - x)(1 - s/z_{\alpha MN})}{1 - s/p_m} \qquad 7.2$$

where F_m is muscle torque, E, αMN input, K_m, muscle stiffness, x_o, joint angle at ideal minimum muscle length, $z_{\alpha MN}$, αMN activation dominant zero, and p_m, muscle activation dominant pole. The joint angle, x, is treated as a constant in this equation (like isometric case) for simplification. Note that the term "muscle" implies extrafusal muscle fiber if not specified elsewhere. The effect of propagation delay will be included in Section 7.6.7.

The frequency response of the arm and load dynamics (the plant) is:

$$P(s) = \frac{X(s)}{F(s)} = \frac{1}{(K_m a_m + K_L) + (B_m a_m + B_L)s + (I_{arm} + I_L)s^2} \qquad 7.3$$

where X is joint angle, F, total torque, K_m, muscle stiffness, B_m, muscle viscosity, I_{arm}, forearm inertia, K_L, load stiffness, B_L, load viscosity, and I_L, load inertia. The normalized muscle activation level, a_m, is treated as a constant in this equation, again for simplification. Note that the muscle internal length-tension and tension-velocity relationships are treated as individual elastic and damping elements in the plant.

The frequency response of the muscle spindle afferent feedback is:

$$H(s) = \frac{E_s(s)}{X(s)} = wr(K_s a_{s1} + B_s a_{s2} s) \qquad 7.4$$

where E_s is Ia afferent feedback output, w, equivalent synaptic weight to αMN, r, a scaling factor, K_s, spindle stiffness, B_s, spindle viscosity, and a_{s1} and a_{s2}, equivalent static and dynamic terms of normalized spindle activation levels (which are the combinations of γMN static and dynamic excitations). The effect of Ib afferent feedback can be analyzed in the same manner.

The relationships X/F_L, P, and $1/GH$ are shown schematically in Fig.7.15, assuming that the zero of αMN activation dynamics matches the pole of muscle activation dynamics. According to Equ.7.1, the value of X/F_L will approximate P if P is much less than $1/GH$ (i.e. GPH is much less than 1, typically in high frequency range), and approximate $1/GH$ if P is much greater than $1/GH$ (i.e. GPH is much greater than 1, usually in medium and low frequency range). In addition, it will be less than either P or $1/GH$ if the phase of GPH is

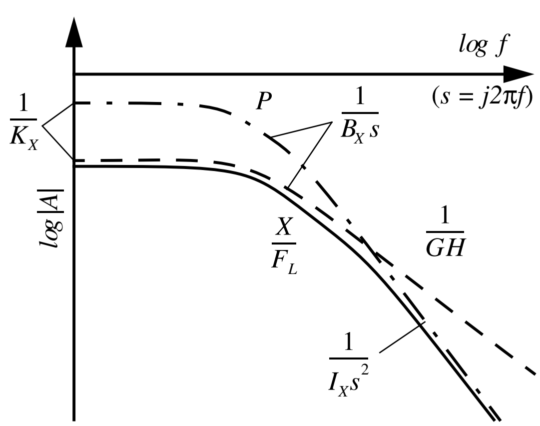

Fig.7.15 Schematics of elbow joint frequency response. X/F_L curve (limb compliance) is upper bounded by and very close to P or $1/GH$ curve, whichever is smaller.

away from 180°. In other words, the X/F_L curve is upper bounded by and very close to the P or the $1/GH$ curve, whichever is smaller. This will be utilized in the following.

7.6.2. Load effects

Viewed in the frequency domain, the arm and load dynamics described in Equ.7.3 (Fig.7.15, curve P), forms three segments with slopes of 0dB/dec (decade), -20dB/dec, and -40dB/dec, respectively. External stiffness and damping were supplied in Lacquaniti et al.'s experiment and are included in our model. Increasing external load stiffness will reduce the magnitude of the 0dB/dec segment and as a result, decrease system damping factor and increase oscillation frequency. This can be verified by comparing row 1 with row 3 in Fig.7.6 and the associated parameters shown in Fig.7.7. Similar changes appear in Lacquaniti's results (Fig.7.5).

Increasing external load viscosity will reduce the magnitude of the -20dB/dec segment and increase system damping factor. This can be verified by comparing Fig.7.6 row 2 (with the smallest damper) with row 1 and row 3. Finally, increasing load inertia will reduce the magnitude of the -40dB/dec segment, and decrease system damping factor and oscillation frequency (this effect is not studied in the experiments).

7.6.3. Open loop co-contraction effects

When subject to open loop co-contraction, the intrinsic stiffness and viscosity of muscle have mechanical effects similar to those described above. However, in biological muscle, the change of viscosity and stiffness are dependent and usually proportional to each other. Under this constraint, without significant change of inertia, the damping factor will increase when the co-contraction level increases. In addition, because the initial external perturbations in the "posture maintenance" experiment were chosen to have the same amplitude of displacement regardless of the system stiffness, the effect of stiffness on steady state position error can not be observed in the results. However, in the "open loop stiffness control" experiment, it is obvious that by applying constant amplitude torque perturbations, the steady state position error will be smaller when joint stiffness increases by muscle co-contraction (Fig.7.2). This is also true with afferent feedback and is also consistent with the linear model. As a result, co-contraction is an effective way not only to reduce the steady state error of joint angle but also to reduce the settling time (proportional to the time constant) of the system. The effect on settling time is shown by comparing Fig.7.6 3.i with Fig.7.9 row 3d. The time constants decrease from 1.02 s to 0.63 s as co-contraction level is increased.

7.6.4. Ia and Ib afferents effects

According to Equ.7.2 and Equ.7.4, the $1/GH$ curve in Fig.7.15 forms two segments with slopes of 0dB/dec and -20dB/dec respectively. As mentioned in “Tools”, the X/F_L curve will approximate the $1/GH$ curve in the low and medium frequency range, and approximate the P curve in the high frequency range. Similar to the effect of open loop co-contraction on the P curve and closed loop response, increasing the spindle stiffness and viscosity (by increasing the γ excitation level) is an alternative way to reduce the steady state error of joint angle and the system time constant. The effect of Ia afference with γ excitation on settling time is shown by comparing Fig.7.6 row 3 with Fig.7.9 row 3b. By applying the Ia afference with α-γ co-activation, the results yield time constants of 0.54 and 0.24 s (Fig.7.6 3.ii and 3.iii). By removing the Ia afference, which is equivalent to deactivating γMN, with only α co-contraction, the results yield time constants of 0.76 and 0.59 s (Fig.7.9 3b.ii and 3b.iii). This effect is also shown by comparing Fig.7.9 row 3c with row 3d, where Ia afference yields time constants of 0.39 and 0.27 s (Fig.7.9 3c.ii and 3c.iii), and without Ia afference yields time constants of 0.75 and 0.63 s (Fig.7.9 3d.ii and 3d.iii).

By combining open loop co-contraction and Ia afference with γ excitation, the system performance greatly increases in terms of steady state error and settling time. This is shown by comparing “do not resist” cases in Fig.7.6 column i with “resist” and “resist harder” cases in column ii and iii. The time constants shown in Fig.7.7 significantly decrease at each load when the α-γ co-activation levels increase.

Two major differences between the Ia afferent effect and open loop co-contraction effect are efficiency and stability. The muscle activity produced by Ia afferent feedback is only induced when there is a perturbation while co-contraction activity is always present.

This makes the Ia afferent feedback more efficient than muscle co-contraction since isometric co-contraction uses a lot of metabolic energy without doing any work. On the other hand, Ia afferent feedback is subject to phase lag due to neural conduction delay. Delay, as is present in both the biological and anthroform arms, limits the maximum feedback gain (and in turn, the closed loop stiffness and viscosity) possible at a given phase margin. This will be discussed more detailed in Section 7.6.7. Time delay has no effect on the stability of the open loop system.

While the Ia afferent feedback increases the closed loop stiffness, the Ib afferent feedback decreases it. The system without Ib afference has higher stiffness, lower damping factor, and longer time constant. This is shown by comparing responses with Ib afference (Fig.7.6 row 3 and Fig.7.9 row 3b) with responses without Ib afference (Fig.7.9 row 3c and row 3d).

Since the Ia and the Ib afferent systems have the opposite effect, how these two afferent systems cooperate remains to be determined. There are two reasonable suggestions 1) Ia afferent feedback is utilized during position-priority tasks while the Ib afferent feedback is utilized during force-priority tasks. And 2) since Ia afferent and Ib afferent signals are not only processed by the spinal segmental reflex circuitry but also propagate through inter-segment and higher CNS levels, they are very likely to be processed by other neural circuitries in different ways and have different effects.

7.6.5. Gamma static and dynamic excitation effects

The mechanical properties of intrafusal muscle fiber are controlled by the γ motoneuron (Binder 1989b). While γ static excitation mainly changes the stiffness of the fiber (Equ.7.4, $K_s a_{s1}$), γ dynamic excitation mainly changes the viscosity ($B_s a_{s2}$). This allows the system to modify position feedback and velocity feedback independently through the Ia afferent. The difference in the resulting system response is shown by comparing Fig.7.6 row 3 with Fig.7.9 row 3a.

7.6.6. Dynamic characteristics of alpha MN and muscle activation

In previous discussion, the zero of αMN activation dynamics and the pole of the muscle activation dynamics were assumed to match each other. Shoemaker (1993) suggested an optimal value of the zero of -26.0 rad/s (-4.13 Hz) for the αMN activation dynamics. Although a cat's αMN was studied in her thesis, this value should be close enough to humans αMN for our experiments. On the other hand, the pole of muscle (actuator) activation dynamics can be derived from the reciprocal of the time constant of muscle (actuator) isometric activation. The time constant of our artificial muscle actuators was measured to be 45 ms, yielding a pole at -22.2 rad/s pole. This is close enough so that we have a good degree of pole-zero cancelation in our system.

The perturbation response of the elbow system without αMN activation dynamics was similar to the result without γ dynamic excitation (Fig.7.9 row 3a). Since there is no longer an αMN zero to cancel the effect of the muscle pole (Equ.7.2). This pole in turn bends the medium and high frequency portion of the *GH* curve to flat (originally 20 dB/dec). In other words, the αMN activation dynamics has a feed forward effect to overcome the high frequency attenuation and phase lag (low pass filtering) of muscle activation dynamics. This helps to maintain stability with higher closed loop gains.

7.6.7. Feedback delay, loop gain, and stability

According to the experiment results shown in Fig.7.12, the delay margin and oscillation frequency are 17 ms and 5 Hz for no load case, and are 10 ms and 6 Hz for stiff load case. These frequency reflect the unity gain frequencies of the original system in different load conditions. The phase margins are equivalent to the phases which are introduced by the delay times at the oscillation frequencies. As a result, the phase margins for no load cases will be 30.6°, and for stiff load case will be 21.6°. In other words, this indicates that the phase of the original system will be 149.4° lag at 5 Hz and 158.4° lag at 6.5 Hz. On the other hand, the measured gain margin (Fig.7.13) is about 1.8, and the oscillation frequency is about 8.5 and 9 Hz for both load conditions. This frequency reflects the 180° phase lag frequency of the original system.

Now, In order to verify the linear model introduced in the previous chapter, the phase margin and gain margin will be derived with the Ia afferent loop gain function, *GPH*. The first pole of αMN dynamics ($z_{\alpha MN}$, relatively higher than the second pole of the plant) is included here for more accurate phase calculation. The resulting loop gain function will be:

$G(s)P(s)H(s) =$

$$\frac{K_m (x_o - x)\left(1 - \frac{s}{z_{\alpha MN}}\right) wr\,(K_s a_{s1} + B_s a_{s2} s)}{\left(1 - \frac{s}{p_m}\right)\left(1 - \frac{s}{p_{\alpha MN}}\right)\left((\Sigma K_m a_m + K_L) + (\Sigma B_m a_m + B_L)\,s + (I_{arm} + I_L)\,s^2\right)} e^{-s\tau} \qquad 7.5$$

where τ is the delay time. The bode plots of Equ.7.5 are shown in Fig.7.16.

Based on the design of the physical system, operating point, and experimental data, the values of parameters in Equ.7.5 are listed in the following:

$K_m = 5.06$ (Nm/rad)

$x_o - x = \pi/2$ (rad)

$z_{\alpha MN} = -26$ (rad/s) * phase angle

$p_{\alpha MN} = -100$ (rad/s) *

$p_m = -22.2$ (rad/s) *

$w = 0.333$

$rK_s a_{s1} = 0.144$ (1/rad)

$rB_s a_{s2} = 0.229$ (s/rad)

$\Sigma K_m a_m + K_L = 5.93$ or 18.93 (Nm/rad)

$\Sigma B_m a_m + B_L = 0.0141$ or 0.0791 (Nms/rad)

$I_{arm} + I_L = 0.02$ (Nm s^2/rad)

$\tau = 17$ (ms)

The equivalent synaptic weight, *w*, is considered to be the summation of the synaptic weight of the Ia afferent to aMN monosynaptic pathway and the synaptic weight product

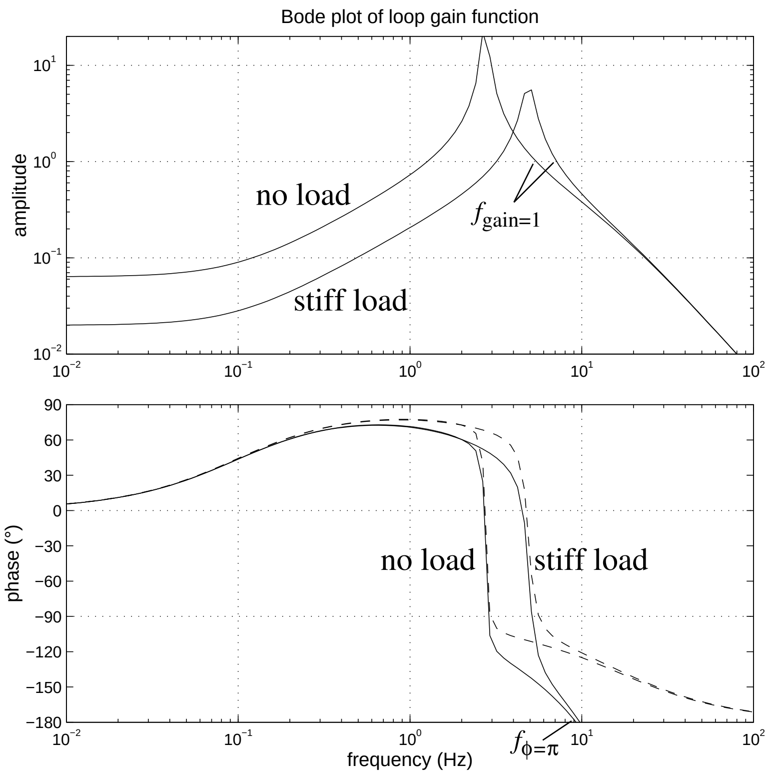

Fig.7.16 Bode plot of loop gain function. $f_{gain=1}$ indicates unity gain frequency, and $f_{\phi=\pi}$ indicates 180° phase lag frequency. Solid lines in phase plot: total phase shifts of feedback loop; dashed lines: phase shifts without propagation delay.

of the Ia through IaIn to antagonist aMN pathway. Apply these values to Equ.7.5 yields the 180° phase lag frequency of 9.24 and 9.59 Hz, the loop gain of 0.440 and 0.501, and the gain margin (reciprocal of the loop gain) of 2.27 and 2.00 for no load and stiff load conditions, respectively. These are very close to the experimental result of 1.8. In addition, the phase margins can also be verified with Equ.7.5 and the above parameters, which yields 35.5° and 27.3° at unity gain frequency of 5.39 and 7.12 Hz for no load and stiff load conditions, respectively. This yields the delay margin of 18.3 and 10.6 ms. This is very close to the experimental delay margins of 17 and 10 ms, again. As a result, the accuracy of the linear model was demonstrated.

Also noteworthy is that according to Equ.7.5 the Ia feedback loop gain at DC is approximately proportional to $wK_s a_{s1} / (\Sigma K_m a_m + K_L)$, which is the product of synaptic weight and the ratio of the spindle stiffness to the joint stiffness. The loop gain at frequency close to unity gain frequency is approximately proportional to $wB_s a_{s2} / (I_{arm} + I_L) s$, which is the product of synaptic weight and the ratio of the spindle viscosity to the joint inertia. As a result, the loop gain can be easily modified dynamically by changing the γMN static and dynamic excitations (resulting the changes in a_{s1} and a_{s2}) instead of changing the synaptic weight.

7.6.8. Addition factors

The results of our experiment (Fig.7.6 and Fig.7.7) are very consist with the results of Lacquaniti's experiment (Fig.7.5) except for the third motor task. Because of the lack of high level response in our system, the two experiments are not directly comparable. We compensated for lack of high level response with increased co-contraction, and labeled the condition "resist harder" in our setup compare to "maximally resist" in their setup. The settling time does not decrease as significantly as it does in "maximally resist" task of Lacquaniti's experiment because of insufficient change of damping. In a recent study, the McKibben pneumatic muscle was found to have less damping than biological muscle (Chou & Hannaford 1994 & 1996). This is a major performance limitation to our physical elbow system. In addition, it is also very likely that the higher level CNS has a time varying strategy to utilize αMN co-activation and γMN static and dynamic excitation. Resolving this question is beyond the scope of this dissertation.

7.6.9. Covariance diagrams

It is not difficult to find a strong relationships between the network configuration (Fig.6.1) and the covariance diagrams (Fig.7.8 and Fig.7.11). An excitatory synapse with large synaptic weight will pre-dominate the covariance of its pre and postsynaptic neurons. This is shown by the strong covariance between the Ia afferent and the αMN (Fig.7.8) which have an excitatory synapse with large synaptic weight, unless feedback is turned off on purpose (Fig.7.11 row 3b and 3d). On the other hand, an inhibitory synapse seems to have less effect on the covariance of its pre and postsynaptic neurons if there are other excitatory sources sent to the postsynaptic neuron. This is shown by the weak covariance between the Ib afferent and the αMN (Fig.7.8) which have an inhibitory synapse with the presence of Ia feedback. As a result, the absence of Ib feedback doesn't change the covariance much (Fig.7.11 row 3c). However, if the inhibitory synapse becomes the only source for the postsynaptic neuron, it will in turn dominate the covariance of its pre and postsynaptic neurons with a negative value. This is shown when the Ib afferent inhibits the αMN without the presence of Ia feedback. Finally, when both Ia and Ib feedbacks are turned off, the covariance between Ia, Ib, and αMN drops into some small value which depends on the pattern of movement.

It is interesting to note that Ia and Ib afferents become strongly co-varying when the γ dynamic excitation of the muscle spindle is absent (Fig.7.11 row 3a). This might imply their high redundancy. However, this covariance will decrease if variable descending command or different load pattern is given.

VIII. Voluntary Forearm Flexion Experiments

In the previous chapter, the posture maintenance experiments, the descending commands of CNS are presumed to be constant during each trial. As a result, only the spinal neural circuitry and the pre-calculated constant descending neural commands are involved. However, more complicated hierarchical networks will be required in multi-segment posture maintenance or voluntary movement tasks. In this chapter, in order to perform voluntary movement, the descending commands must change dynamically according to desired movement. As a result, it is necessary to integrate higher level feed forward controllers into the neural controller to convert movement parameters to spinal neural input patterns.

8.1. Feed Forward Inverse Kinematics and Dynamics Controller

We operate on the theory that through repeated experience, the CNS has learned very well to predict the amount of motor unit activity for posture maintenance, accelerating, and decelerating limb segments. This requires some feed forward networks capable of performing certain types of neural activity transformation from conceptual domains, such as hand position and velocity, to executive domains, such as elbow and shoulder joint angles or motor unit activities. The positioning part is the inverse kinematics transformation, and the moving part is the inverse dynamics transformation.

A feed forward, time delayed perceptron neural network (Hertz et al. 1991) would be capable of implementing the above transformations. However, our concern is with modeling the spinal circuitry at the segmental level, thus, in the following experiment, these feed forward features are implemented with non-neural kind mathematical formulations.

8.1.1. Inverse kinematics

The simplified kinematic model of the musculo-skeletal system of the testing elbow can be described as:

$$T_f = -K_f a_f(\theta - \theta_{fo}) + T_{fo} \tag{8.1a}$$

$$T_e = -K_e a_e(\theta - \theta_{eo}) + T_{eo} \tag{8.1b}$$

$$T_f = -T_{cc} - r_f T_L \tag{8.1c}$$

and $$T_e = T_{cc} - r_e T_L \tag{8.1d}$$

with $r_f + r_e = 1$, where T_x and T_{xo} are the joint torque and offset generated by flexor if $x = f$, or extensor if $x = e$; T_{cc}, co-contraction torque; T_L, external torque; K_x, active stiffness constant; a_x, muscle activation level; θ and θ_{xo}, joint angle and threshold; r_x, load distribution factor. By solving Equ.8.1a to d, the solutions for forward kinematics and inverse kinematics are obtained.

Now the solutions for the inverse kinematics under no load condition are:

$$a_f = \frac{T_{cc} + T_{fo}}{K_f(\theta_d - \theta_{fo})} \tag{8.2a}$$

and $$a_e = \frac{T_{cc} - T_{eo}}{K_e(\theta_{eo} - \theta_d)} \tag{8.2b}$$

with input variables θ_d and T_{cc} and parameters optimized to:

$K_f = 5.0$ (Nm/rad)

$K_e = 3.5$ (Nm/rad)

$\theta_{fo} = -2.2$ (rad)

$\theta_{eo} = 1.8$ (rad)

$T_{fo} = 1.7$ (Nm)

$T_{eo} = -1.3$ (Nm)

based on the measurement of the testing elbow. Note that the desired joint angle, θ_d, is substituted for the actual joint angle, θ, since this is a feed forward transformation. The results are illustrated in Fig.8.1.

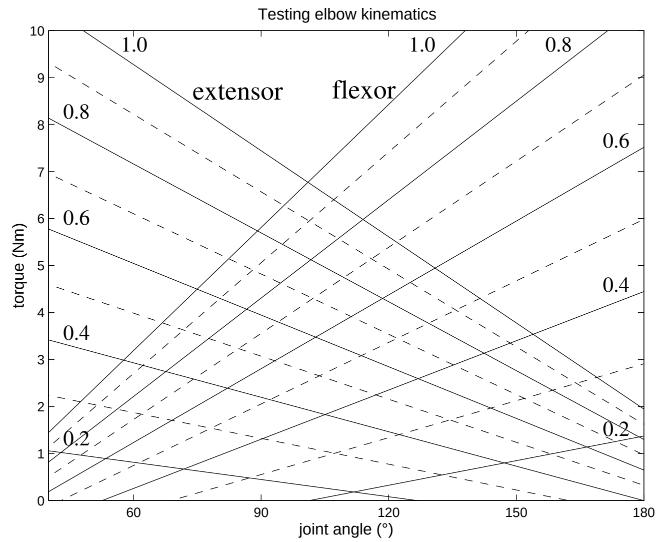

Fig.8.1 Torque-angle-activation relationships of testing elbow. Normalized muscle activation level is indicated on top of each curve.

8.1.2. Inverse dynamics

The simplified dynamics model can be described as:

$$-K_f a_f(\theta-\theta_{fo}) + T_{fo} - B_{fm}\dot{\theta} = r_f\Big(K_L\theta + B_L\dot{\theta} + (I_{arm}+I_L)\ddot{\theta} - T_L\Big) - T_{cc} \qquad 8.3a$$

$$-K_e a_e(\theta-\theta_{eo}) + T_{eo} - B_{em}\dot{\theta} = r_e\Big(K_L\theta + B_L\dot{\theta} + (I_{arm}+I_L)\ddot{\theta} - T_L\Big) + T_{cc} \qquad 8.3b$$

with the load distribution factors: $r_f + r_e = 1$, where B_{xm} is muscle viscosity; I_{arm}, inertia of the testing elbow; and K_L, B_L and I_L are load stiffness, viscosity and inertia, respectively.

The solutions for the no load condition are:

$$a_f = \frac{T_{cc} + T_{fo} - B_{fm}\dot{\theta}_d - r_f I_{arm}\ddot{\theta}_d}{K_f(\theta_d - \theta_{fo})} \qquad 8.4a$$

$$\text{and} \quad a_e = \frac{T_{cc} - T_{eo} + B_{em}\dot{\theta}_d + (1-r_f)I_{arm}\ddot{\theta}_d}{K_e(\theta_{eo} - \theta_d)} \qquad 8.4b$$

with input variables θ_d, T_{cc}, and r_f, and the additional parameters:

$B_{fm} = B_{em} = 0.14$ (Nm s/rad)

$I_{arm} = 0.02$ (Nms^2/rad)

The r_f is set to 0.8 during voluntary flexion and 0.2 during voluntary extension in order to match the EMG activities of physiological experiment (Dufresne et al. 1978).

8.1.3. Input redundancy

Another problem for the inverse kinematics and dynamics transformations is input redundancy since there are more inputs to the spinal reflex circuitry than outputs. There are 8 inputs including pairs of descending commands to αMN, γMN, IaIn, and IbIn neurons. Although the spinal reflex circuitry (Fig.6.1) used in the neural controller is based on well accepted information, we still lack evidence on the patterns of the descending inputs. We approach this problem by considering the functions of each type of neurons.

First, let's consider the simplified version of the spindle model emulated by the mechanical spindle and the DSP neural emulator:

$$Ia = r\left(K_s a_s (\theta - \theta_{so})\left(1 + b_s\dot{\theta}\right) - T_{so}\right) \qquad 8.5$$

Assume the Ia afferent firing will remain constant if the muscle follows the desired length and desired shortening or lengthening velocity. This is achieved when the external load is not present and the αMN and γMN commands are carefully coordinated. The approximate solution for the γMN input (using Equ.8.5) is:

$$a_s = \frac{(Ia_d + T_{so})\left(1 - b_s\dot{\theta}_d\right)}{rK_s(\theta_d - \theta_{so})} \qquad 8.6$$

The IaIn interneurons are presumed to perform the reciprocal inhibition of the agonist and antagonist pair of αMNs. As a result, the αMN commands are also sent to the IaIn interneurons.

Finally, we presume that the function of the Ib afferent system is inhibitory tension feedback. Therefore neural activity proportional to the desired tension of each actuator is sent through inhibitory synapses to the IbIn interneuron to dis-inhibit their αMNs.

8.2. Voluntary Fast Forearm Flexion Experiments

In these experiments, fast forearm flexion movements were performed with different feed-forward functions of the controller. The first experiment includes complete feed-forward functions in the controller which were described in the previous section. The second experiment removes the feed-forward inverse dynamics function to the αMNs from the controller (by assigning the viscosity, B_{em} and B_{fm}, and inertia, I_{arm}, to zero). And the third experiment removes the feed-forward compensation to the γMNs (by assigning the viscosity, b_s, to zero). The results show that 1) without the feed-forward inverse dynamics command to the αMNs, the movement has long initiation latency, slow acceleration, large overshoot, and slow convergence to target position. And 2) without the feed-forward command to the γMNs, the extensor Ia afferent produces significant output during forearm flexion, and the movement has "premature breaking" before reaching target position (Fig.8.2).

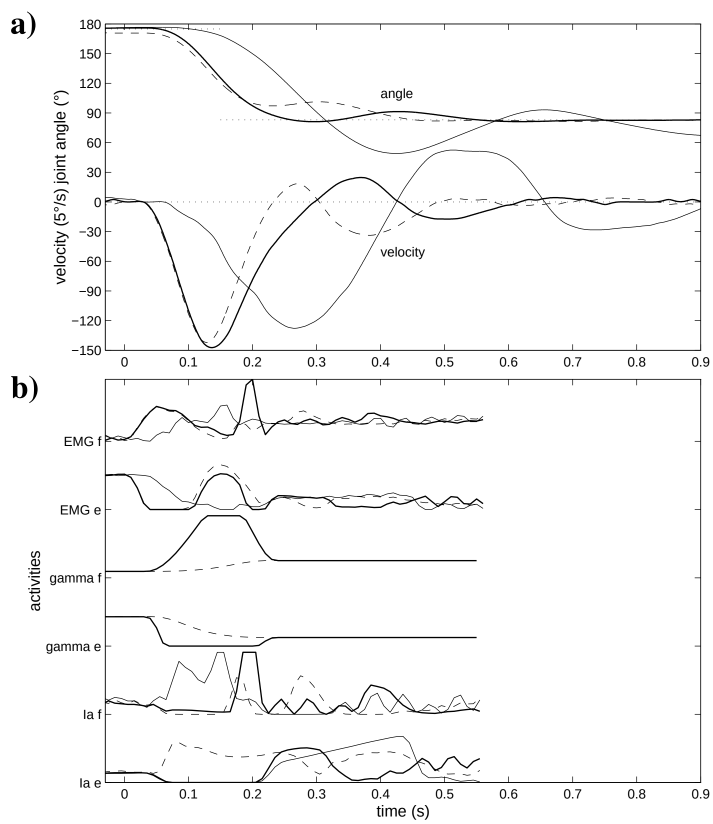

Fig.8.2 a and **b** Voluntary fast forearm flexion movements. Three curves are superimposed in each plot. Thick solid lines: movement with complete feed-forward inverse dynamics commands; thin solid lines: without inverse dynamics command to αMNs; dashed lines: without inverse dynamics command to γMNs.

8.3. Response to Transient Disturbances During Intentional Forearm Flexion

The testing conditions of this experiment are designed to resemble the fast elbow flexion experiment performed by Dufresne et al. (1978), who investigated whether the motor outputs to both agonist and antagonist muscles are accessible and influenced by sensory input signals. In their experiment, the subjects' upper arm was fixed, and their forearm was co-axially fitted with a lever to a torque motor which generated step torque during intentional forearm flexion without prior informing the subjects. In reproducing this experiment in the testing elbow system, we need to minimize the dependence on higher

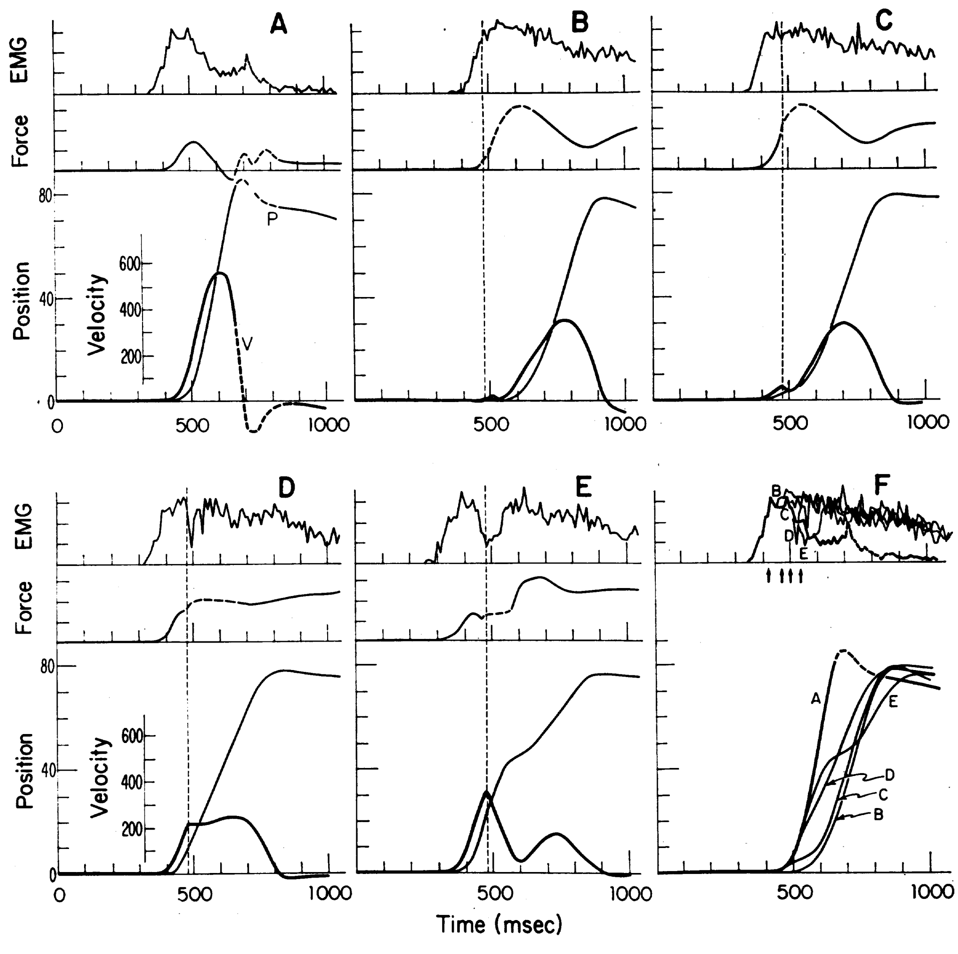

Fig.8.3 A to **F** Experimental results of Dufresne et al. Response to extension torque steps during maximal-velocity flexion movements. **A** Undisturbed movement. **B** to **E** Movements disturbed by 10 Nm torque steps with application time indicated by vertical dashed lines. **F** Composite of position and EMG of **A** to **E**, with time of torque onset given by arrows. (source: Brain Research, vol. 150: 103-115, Fig.3)

level feedback due to the lack of such control in the testing elbow system, therefore we emulated only the task of "move as fast as possible" (Fig.8.3). In this task, the subjects were instructed to initiate a flexion movement towards a target position upon command. The results of their experiments showed that the EMG activities of the biceps and triceps brachii change greatly in response to the disturbing torque step. The average EMG response latency was about 31.7 ms (derived from Table I of Dufresne et al. 1978).

In this experiment, to produce the fast flexion command, a 3rd order polynomial is used to generate the desired trajectory between initial and target positions. The initial position is 160° and the target position is 80°. The velocity at both ends are set to zero, and the movement duration is 0.2 s. This desired trajectory is then sent to the feed forward controller to translate into the descending command pattern. Four sets of trials were

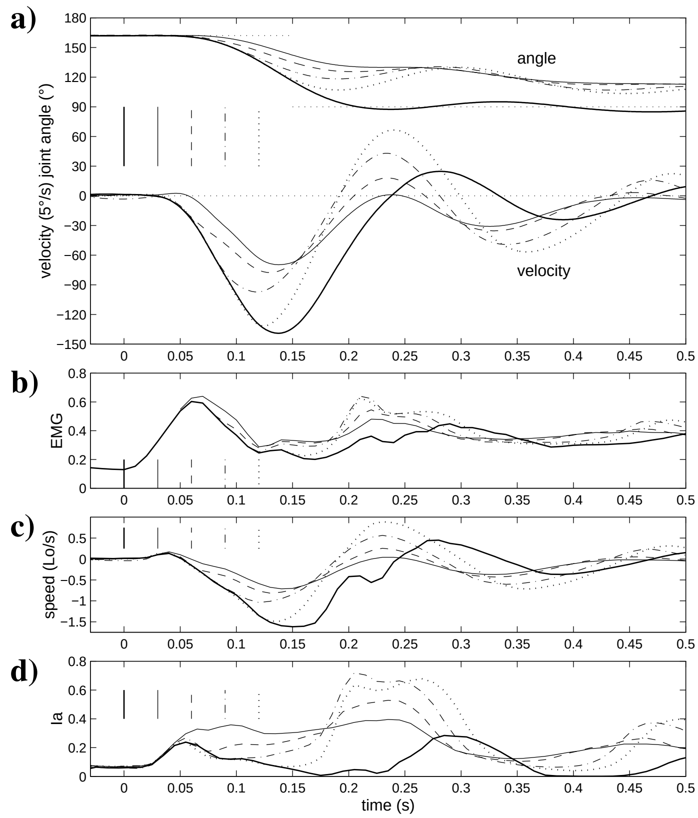

Fig.8.4 a to **d** Responses to extension torque steps during maximal-velocity flexion movements. Five curves are superimposed in each plot. Thick solid lines: undisturbed movement. Thin lines: movements disturbed by 2.5 Nm torque steps with time of torque onset indicated by vertical lines; solid line: 30 ms after onset of movement; dashed line: 60 ms; center line: 90 ms; dotted line: 120 ms.

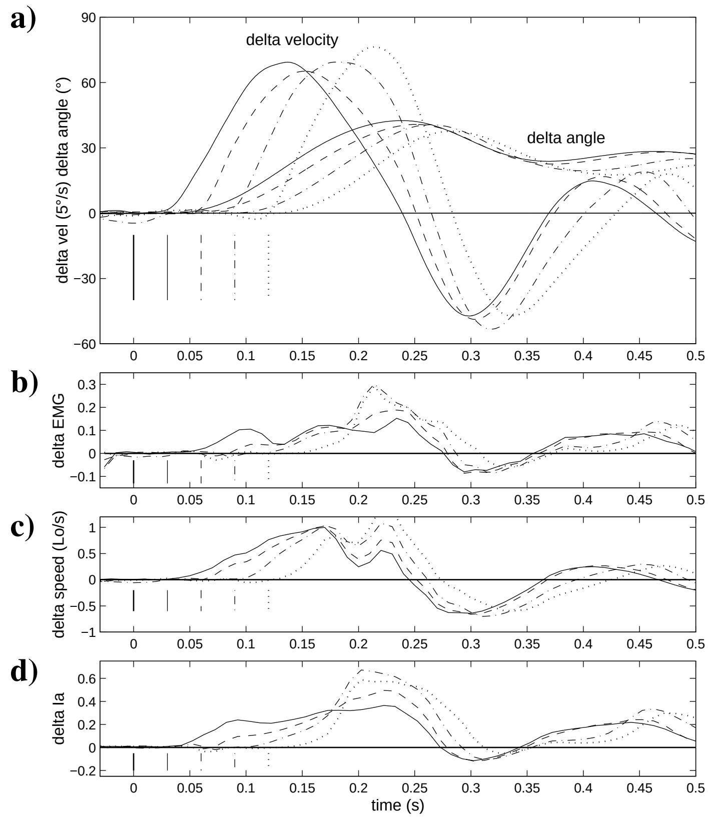

Fig.8.5 Differential responses to extension torque steps during maximal-velocity flexion movements. Each curve shows the difference between disturbed and undisturbed movements which shown in Fig.8.4. Definitions of line style are the same as Fig.8.4.

recorded with the 2 Nm torque step applied 30, 60, 90, and 120 ms after the initiation of movement, respectively. Another set of trials were performed without the torque step. The averaged experimental results of each set are superimposed in Fig.8.4, and the differential amount between each disturbed trial and the non-disturbed one is shown in Fig.8.5. The results show that the EMG has noticeable responses to the transient disturbances. However, it is much less significant than Dufresne's experiment. We observed responses of about 15% of maximum EMG activity compared to their result of 60%. In addition, the responses latency is about 20 ms instead of 31.7 ms in their results.

8.4. Discussion

8.4.1. Inverse kinematics and dynamics

The inverse kinematics and dynamics feed forward features effectively transfer the desired trajectory signal into a pattern of descending neural activities, and produce accelerating, viscous, and elastic torques which are necessary to perform fast movement accurately.

In the fast flexion experiments, when the inverse dynamics compensation was removed, very poor performance was observed, including long movement initiation latency, low movement acceleration and velocity, large overshoot, and slow converging speed (Fig.8.2a thin solid lines). This obviously disagrees with the “equilibrium-point hypothesis” first proposed by Feldman in 1966 (for a modified version, refer to Feldman 1986), which suggested the CNS is not required to perform the inverse dynamics transformation in voluntary movement.

On the other hand, the accuracy of the inverse dynamics transformation and its parameters effect movement performance but not stability (a feed forward controller cannot alter the stability of the controlled system). This disagrees with Bizzi et al. (1992), who claimed that “inertial parameter errors as small as 5% can result in instability” based on robotic experience of Slotine’s (1985).

8.4.2. Input redundancy

The feed forward controller also provides a feasible way to utilize the input redundancy of the spinal reflex circuitry. By properly coordinating α and γ motoneurons, the Ia afferents maintain minimal variation on their outputs when the disturbance is absent (Fig.8.2b thick solid lines). This keeps the Ia afferents away from saturation or deactivation, and in turn makes the Ia afferents more sensitive to the position and velocity error induced by external disturbance if presented. Without the proper coordination, the Ia afferents will fire while the antagonist muscle is lengthening and misfire while the agonist muscle is shortening voluntarily (Fig.8.2b dashed lines). This undesired firing or misfiring would cause muscles to react against their own voluntary movement (premature breaking, Fig.8.2a dashed lines). In other words, the bandwidth and efficiency of the system in response to voluntary commands would greatly decrease and become unacceptable.

8.4.3. Spinal reflex effects

Before discussing the effects of the reflexes on the disturbances, we should focus our interest on the period before the intentional correcting command arrives from higher level of the CNS, which was suggested to be 100-120 ms by Dufresne et al. (1978). The response after this period would be expected to involve intentional process, which could not be performed by the spinal reflex circuitry, and should not be confused with the reflex effects.

In the trials with step torque disturbances, the results showed that the EMG visibly changed in response to the disturbances. These were caused by: 1) the step torque produced negative acceleration in the movement, 2) this deceleration slowed the velocity of the elbow joint (Fig.8.4 and 8.5 a) as well as the velocity of the spindle (Fig.8.4 and 8.5 c), 3) the velocity discrepancy of the spindle changed the Ia afferent firing (Fig.8.4 and 8.5 d), and 4) the difference of the Ia afferent firing fed back to the αMN and changed the EMG activity (Fig.8.4 and 8.5 b) and muscle tension. This in turn partially corrected the disturbed movement.

However, the magnitude of spinal reflex response we observed is much less significant than Dufresne's experiment. In addition, the response latency is less. According to our linear stability analysis (Section 7.6.7), the gain margin limits how much the feedback loop gain can be increased to 1.8 times its current value. Hypothetically, increasing the synaptic weights of the Ia afferent system to 1.8 times will increase the magnitude of response to 27% of maximum EMG activity, but this is still not comparable to Dufresne's result, in spite of the significant degradation of stability caused by this increased loop gain. In addition, if the 31.7 ms delay of the Dufresne's data were to be implemented on the testing elbow, the high feedback loop gain would bring the system far from its stable region. One possible suggestion to explain these phenomena will be described in the following.

8.4.4. Proposed long latency feedback mechanism

According to the previous discussion, our spinal reflex emulation circuitry, although it has noticeable reaction to torque disturbance, is not capable of producing all of the experimental observed EMG activity. In addition, the latency of the spinal mono-synaptic reflex was estimated to be 17 ms (Section 7.5), which is much less than the 31.7 ms observed in Dufresne's result.

Now let's consider Deuschl and Lucking's study (1990), where a reflex component having total delay of 40 ms was observed in the EMG of various hand muscles in addition to a short latency reflex (SLR) of 28 ms delay. They classified this as "long latency reflex (LLR) I", and suggested this kind of reflex is produced by supraspinal or trans-cortical pathways. By considering the shorter length of the peripheral axons to the elbow flexor and extensor, the LLR I for the biceps and triceps brachii would be very close to the 31.7 ms.

One reasonable suggestion is that the response is a "nearly open loop, triggering" reaction. To explain this, first, since the magnitude and direction of the torque step never changed in the task of "move as fast as possible", the subjects could have learned the right amount of correcting command after repeated tests, and pre-programmed this correcting command. Once the CNS sensed the onset of resistance, it just executed, or triggered the pre-programmed command without relying on the consequent afferent signals. This is almost an open loop control scheme, and so doesn't have the stability problems.

Certain predictions for utilizing such "nearly open loop" control scheme can be derived as follows. 1) It will be very inaccurate if the step torque (or any other predictable pattern) changes its magnitude and direction, or more than one step is applied, otherwise it will require additional response time for the CNS to "sample" and estimate the new amount of torque disturbances. 2) It is only usable when the patterns of disturbances are predictable. For an arbitrary shaped analog torque disturbance, the CNS must keep listening to the afferent signals to re-sample and re-estimate the disturbance continuously. This also suggests that the CNS can choose different control schemes under certain situations to achieved the desired goal more effectively. And 3) it will take additional time for the CNS to voluntarily switch from another control scheme to this "nearly open loop" control scheme.

Similar phenomena to the first prediction can be found in physiological experiments performed by MacKay and Bonnet's study in 1990 (also Bonnet & MacKay 1989). In their forearm stretch reflex experiments, human subjects were given varying amount of prior information regarding the direction (flexion or extension) or force level (weak or strong) of an impending torque step. Their results showed the reaction time was shorter when direction was known in advance. Cortical activity and late stretch reflexes with very large magnitude were also observed, which indicates that with full prior information, "the intended movement had been fully processed by this time (the last 100 ms of the preparatory period) and awaited only a sensory trigger".

The third prediction agrees with the results shown in Fig.8.6 (Fig.5 of Dufresne et al. 1978), where the subjects were asked to perform fast flexion when an initial external

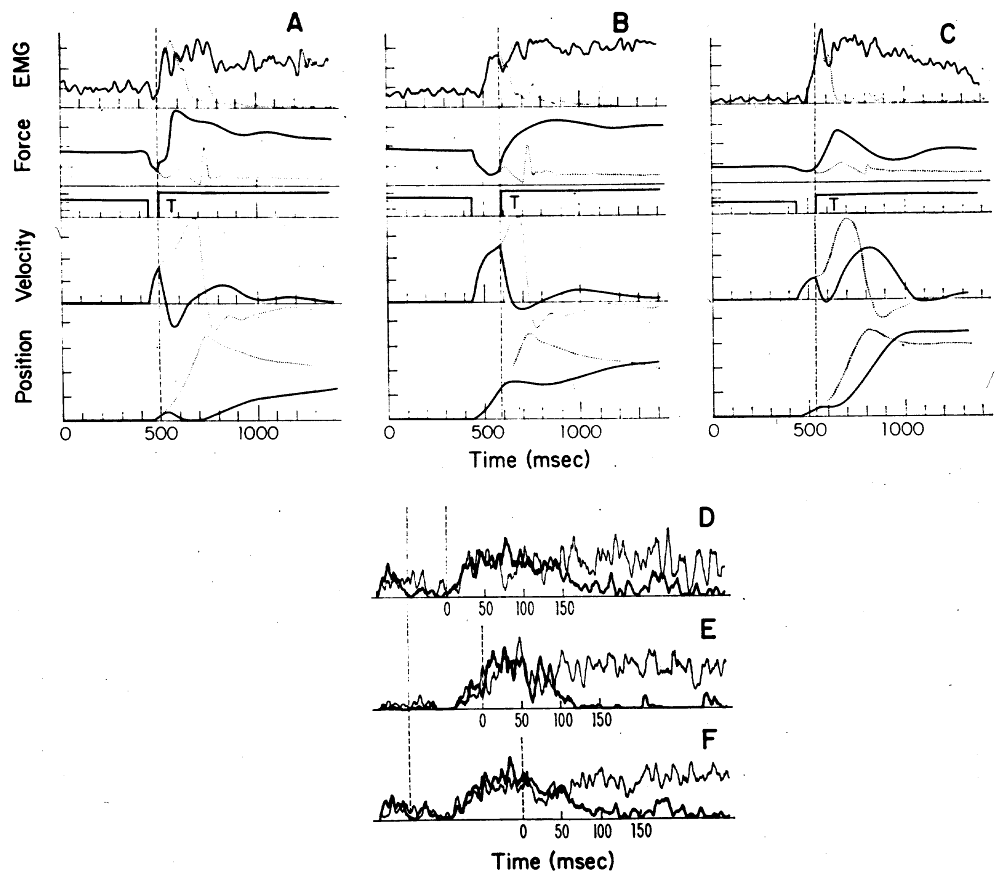

Fig.8.6 A to **F** Experimental results of Dufresne et al. Response to extension torque steps during maximal-velocity flexion movements with initial holding torques. **A** to **C** Movements disturbed by different magnitude torque steps with application time indicated by vertical dashed lines. **D** to **F** EMG of **A** to **C** with higher time-resolution. The first dashed vertical line indicates holding torque releasing time, the second indicates torque steps onset time. (source: Brain Research, vol. 150: 103-115, Fig.5)

holding torque was suddenly removed. As a result, the subjects had to change the control scheme from “hold and wait” to “start flexion and (nearly open loop) resist torque step”. The triggering reaction was not enabled until 190 ms after the holding torque disappeared. This yielded the resulting response delay for the following torque step to be much longer than the original 31.7 ms. Unfortunately, we did not have sufficient time and resources to further study this “nearly open loop” control scheme. More physiological and robotic experiments are encouraged to verify this proposed control scheme based on the three predictions in the future.

IX. Conclusion

9.1. Posture Maintenance

The neural controller and testing elbow have successfully demonstrated human-like performance in both open loop and closed loop conditions. In open loop conditions, the muscle intrinsic stiffness was effectively controlled by muscle co-contraction. In simple closed loop conditions, the joint stiffness increased significantly when the synaptic weight from Ia afferent to α motoneuron increased, and decreases significantly when the synaptic weight from Ib inhibitory interneuron to α motoneuron increased. By implementing a model of human spinal reflex neural circuitry into the controller, the elbow joint response to transient perturbation resembled experimental results in humans. The results showed that muscle co-contraction with afferent feedback greatly increased the system damping factor and shortened the settling time of the transient damped oscillation.

By utilizing the flexibility and repeatability of the neural controller, networks with modified synapses or neural activation dynamics were tested systematically to predict the results of experiments which are impossible to perform on human subjects. These tests also revealed roles of several synaptic connections and neurons. The results illuminated that 1) γ dynamic excitation is essential to produce the velocity feedback of the Ia afferent signal, which then effectively increases the closed loop damping factor. 2) The effect of the Ib afferent system is not significant in the posture maintenance task. 3) The α motoneuron activation dynamics works as a feed forward phase-lead controller to compensate the low-pass-filtering effect of muscle, and to maintain the system open loop bandwidth and phase in a closed loop controllable condition. And 4) the loop gain of the reflex loop was verified to be small, and the delay margins were predicted to be 17 ms for no load condition, and 10 ms for stiff load condition. Any abnormal physiological condition increasing the reflex response time over these limits is expected to cause the closed loop system to be unstable and useless.

Finally, the covariance diagram was a useful method to visualize relationships between large numbers of neuron activities and physical variables.

9.2. Voluntary Forearm Flexion

The inverse kinematics and dynamics feed forward models effectively transferred the desired trajectory signal into the pattern of descending neural activities, and produced accelerating, viscous, and elastic torques which are necessary to perform fast movement accurately.

The feed forward controller also provided a feasible way to utilize the input redundancy of the spinal reflex circuitry to properly coordinate the α and γ motoneuron activations. This kept the Ia afferents away from saturation or deactivation, and in turn made the Ia afferents more sensitive to the position and velocity error induced by external disturbance. Without the proper coordination, the Ia afferents would generate undesired firing or misfiring, and cause muscles to react against their own voluntary movement.

Also, the experiment results showed that there are noticeable reflex effects in response to external disturbance during voluntary fast flexion. However, the magnitude and delay of reflex response produced by the neural controller were much smaller than physiological data. Attempts to obtain the large reflex magnitude and delay caused the closed loop controlled system to be unstable.

One possible mechanism responsible for this large magnitude and delay reflex is so called “long latency reflex (LLR) I”, which was suggested to be produced by supraspinal or transcortical reflex. The CNS might utilize the LLR-I pathways to apply the proposed “nearly open loop” control scheme (Section 8.4.4) against step torque disturbances with predictable magnitude, and avoid the closed loop instability problem.

9.3. Limitations and Future Work

In the future it will be possible to extend the emulated neural circuitry to perform multi-joint tasks with the Anthroform Arm. However, due to the large number of synapses and neurons, a neural learning method will become more important for tuning the network parameters. A Hebbian type algorithm (Hebb 1949) may be the most desirable one. The required computations can be easily integrated into the neural controller and can run in real time.

For the higher level control, the "nearly open loop" control scheme was proposed to avoid closed loop instability. However, it was also predicted that accuracy would decrease and the response delay would increase if the disturbing torque consisted of more than one step or had arbitrary magnitude and direction. Physiological and robotic experiments are encouraged to verify this proposed control scheme based on the three predictions.

Finally, the implementation of higher level feed forward and feedback neural circuitries will have more difficulties to face. Although substantial data are available from single unit recordings (Fetz 1993) (Fetz et al. 1989) and models (Borghese & Arbib 1995), compared to the complexity of high level neural circuitry, there is still a lack of physiological experiment data on these pathways in human and animal CNS. The integration of this knowledge into a predictive model of movement, posture, and contact control will be a major role for physical replica models like the Anthroform Arm.

References

[1] Alexander GE, DeLong MR & Crutcher MD (1992) "Do cortical and basal ganglionic motor areas use "motor programs" to control movement?" Behavioral and Brain Sciences, vol. 15: 656-665.

[2] Allum JHJ & Young LR (1976) "The relaxed oscillation technique for the determination of the moment of inertia of limb segments", J. Biomechanics, vol. 9: 21-25.

[3] Binder MD (1989a) "Properties of motor units", in Textbook of Physiology, 21 ed., vol. 1, ch. 23, Univ. of Washington, School of Medicine, Seattle, Washington.

[4] Binder MD (1989b) "Peripheral motor control: spinal reflex actions of muscle, joint, and cutaneous receptors", in Textbook of Physiology, 21 ed., vol. 1, ch. 24, Univ. of Washington, School of Medicine, Seattle, Washington.

[5] Binder MD (1989c) "Spinal and supraspinal control of movement and posture", in Textbook of Physiology, 21 ed., vol. 1, ch. 26, Univ. of Washington, School of Medicine, Seattle, Washington.

[6] Bizzi E, Hogan N, Mussa-Ivaldi FA & Giszter S (1992) "Does the nervous system use equilibrium-point control to guide single and multiple joint movements?" Behavioral and Brain Sciences, vol. 15: 603-613.

[7] Bonnet M & MacKay WA (1989) "Changes in contingent-negative variation and reaction time related to precueing of direction and force of a forearm movement", Brain, Behavior and Evolution, vol. 33(2-3): 147-152.

[8] Borghese NA & Arbib MA (1995) "Generation of temporal sequences using local dynamic programming", Neural Networks, vol. 8, no. 1: 39-54.

[9] Brink E, Jankowska E, McCrea DA & Skoog B (1983) "Inhibitory interactions between interneurons in reflex pathways from group Ia and group Ib afferents in the cat", J. Physiology, vol. 343: 361-373.

[10] Bullock D, Contreras-Vidal JL & Grossberg S. (1992) "Equilibria and dynamics of a neural network model for opponent muscle control", in Neural Networks in Robotics, eds: Bekey & Goldberg, Kluwer Academic, Boston, pp. 439-457.

[11] Burke RE, Rudomin P and Zajac FE (1976) “The effect of activation history on tension production by individual muscle units”, Brain Res., vol. 109: 515-529.

[12] Chou C-P and Hannaford B (1992) “Dual stable point model of muscle activation and deactivation”, Biological Cybernetics, vol. 66: 511-523.

[13] Chou C.-P. & Hannaford B (1994) “Static and dynamic characteristics of McKibben pneumatic artificial muscles”, Proc. IEEE Intl. Conf. on Robotics and Automation, San Diego, CA, May 1994, vol. 1: 281-286.

[14] Chou C.-P. & Hannaford B (1996) “Measurement and modeling of McKibben pneumatic artificial muscles”, IEEE Trans. on Robotics and Automation, vol. 12, no. 1.

[15] Deuschl G & Lucking CH (1990) “Physiology and clinical applications of hand muscle reflexes”, in New Trends and Advanced Techniques in Clinical Neurophysiology, eds: Rossini & Mauguiere, Elsevier Science Publishers.

[16] Dufresne JR, Gurfinkel VS, Soechting JF & Terzuolo CA (1978) “Response to transient disturbances during intensional forearm flexion in man”, Brain Res., vol. 150: 103-115.

[17] Feldman AG (1986) “Once more for the equilibrium point hypothesis (λ model)”, J. Motor Behavior, vol. 18: 17-54.

[18] Fetz EE (1993) “Cortical mechanisms controlling limb movement”, Curr-Opin-Neurobiol, vol. 3, no. 6: 932-939.

[19] Fetz EE, Cheney PD, Mewes K, & Palmer S (1989) “Control of forelimb muscle activity by populations of corticomotoneuronal and rubromotoneuronal cells”, Prog. in Brain Research, vol. 80, Elsevier, 1989.

[20] Fuchs AF (1989) “The neural control of movement”, Textbook of Physiology, 21 ed., vol. 1, ch. 22, University of Washington, School of Medicine, Seattle, Washington.

[21] Gandevia SC & Burke D (1992) “Does the nervous system depend on kinesthetic information to control natural limb movements?” Behavioral and Brain Sciences, vol. 15: 614-632.

[22] Gasser HS and Hill AV (1924) “The dynamics of muscular contraction”, Proc. R. Soc. B, vol. 96: 398-437.

[23] Gavrilovic MM and Maric MR (1969) “Positional servo-mechanism activated by artificial muscles”, Medicine & Biological Engineering, vol. 7: 77-82.

[24] Gomi H & Kawato M (1993) “Neural network control for a closed loop system using feedback-error-learning”, Neural Networks, vol. 6, no. 7: 933-946.

[25] Gordon AM, Huxley AF and Julian FJ (1966) “The variation in isometric tension with sarcomere length in vertebrate muscle fibers”, J. Physiology, vol. 184: 170-192.

[26] Gordon AM (1989) “Contraction in skeletal muscle”, in: Textbook of Physiology, 21 ed., vol 1: excitable cells and neurophysiology, ch. 8, Seattle, Washington.

[27] Gordon AM and Ridgway EB (1990) “Stretch of active muscle during the declining phase of the calcium transient produces biphasic changes in calcium binding to the activating sites”, J. Gen. Physiology, vol. 96: 1013-1035.

[28] Guyton A C (1986) “Contraction of skeletal muscle”, in: Textbook of Medical Physiology, ch. 11, 7th ed.

[29] Hannaford B & Winters JM (1990) “Actuator properties and movement control: biological and technological models”, in Multiple Muscle Systems, ch.7, eds: Winters & Woo, Springer-Verlag, New York.

[30] Hannaford B, Winters JM & Chou C.-P. (1994) “The anthroform biorobotic arm”, Video Proceedings, IEEE Intl. Conf. on Robotics and Automation, San Diego, CA, May 1994.

[31] Hannaford B, Winters JM, Chou C.-P. & Marbot PH (1995) “The Anthroform Arm: a system for the study of spinal circuits”, Annals of Biomedical Engineering: L. Stark Special Issue, March 1995, vol. 23: 399-408.

[32] He J, Levine WS & Loeb GE (1991) “Feedback gains for correcting small perturbations to standing posture”, IEEE Trans. on Automatic Control, vol. 36-3: 322-332.

[33] Hebb DO (1949) “The organization of behavior: a neuropsychological theory”, John

Wiley & Sons, New York.

[34] Helm FCT van der (1991) “The shoulder mechanism, a dynamic approach”, Doctoral thesis, Dept. Mechanical Engr. and Marine Tech., Delft University of Technology.

[35] Hertz J, Krogh A & Palmer RG (1991) “Introduction to the theory of neural computation”, Addison-Wesley Publishing Company, Redwood City, CA.

[36] Hill AV (1938) “The heat of shortening and the dynamic constants of muscle”, Proc. R. Soc. B, vol. 126: 136-195.

[37] Hogan N, Bizzi E, Mussa-Ivaldi FA & Flash T (1987) “Controlling multijoint motor behavior”, Exercise and Sports Sciences Reviews, vol. 15: 153-190.

[38] Hollerbach JM & Atkeson CG (1987) “Deducing planning variables from experimental arm trajectories: pitfalls and possibilities”, Biological Cybernetics, vol. 56: 279-292.

[39] Inoue K (1988) “Rubbertuators and applications for robots”, Robotics Research: the 4th International Symposium, eds: Bolles & Roth, MIT Press, Cambridge, MA, 1988.

[40] Jacks A, Prochazka A & Trend PS (1988) “Instability in human forearm movements studied with feedback-controlled electrical stimulation of muscles”, Journal of Physiology, vol. 402:443-461.

[41] Lacquaniti F, Licata F, & Soechting JF (1982) “The mechanical behavior of the human forearm in response to transient perturbations”, Biological Cybernetics, vol. 44: 35-46.

[42] Levin A and Wyman J (1927) “The viscous elastic properties of muscle”, Proc. R. Soc. B, vol. 101: 218-243.

[43] Loeb G (1987) “Hard lessons in motor control from the mammalian spinal cord”, TINS, vol. 10, no. 3: 108-113.

[44] MacKay WA & Bonnet M (1990) “CNV, stretch reflex and reaction time correlates of preparation for movement direction and force”, Electroencephalography and Clinical Neurophysiology, vol. 76-1: 47-62.

[45] Marbot PH (1995) “Ia response of a Mechanical Spindle replica”, Ph.D. Dissertation,

University of Washington, Department of Electrical Engineering, March 1995.

[46] Marbot PH & Hannaford B (1993) "The Mechanical Spindle: a replica of the mammalian muscle spindle", Proc. IEEE Conf. on Engineering in Medicine and Biology, San Diego, CA, October 1993.

[47] Marsden CD, Merton PA & Morton HB (1976) "Stretch reflex and servo action in a variety of human muscles" J. Physiology, vol. 259: 531-560.

[48] McCrea DA (1986) "Spinal cord circuitry and motor reflexes", Exercise and Sport Sciences Reviews. 14: 105-141.

[49] McCrea DA (1992) "Can sense be made of spinal interneuron circuits?" Behavioral and Brain Sciences, vol. 15: 633-643.

[50] MacDuff I, Venema S & Hannaford B (1992) "The Anthroform Neural Controller: a system for detailed emulation of neural circuits", Proc. IEEE Intl. Conf. on Systems, Man, and Cybernetics, vol. 1: 117-22, Chicago, IL, October, 1992.

[51] McMahon TA (1984) "Fundamental muscle mechanics", in: Muscle, Reflexes, and Locomotion, ch. 1, Princeton University Press, Princeton, New Jersey.

[52] Raibert MH (1978) "A model for sensorimotor control and learning", Biological Cybernetics, vol. 29: 29-36.

[53] Ramos CF, Hacisalihzade SS, & Stark LW (1990) "Behaviour space of a stretch reflex model and its implications for the neural control of voluntary movement", Medical & Biological Engineering & Computing, vol. 28, no. 1: 15-23.

[54] Schaafsma A, Otten E & Willigen JD van (1991) "A muscle spindle model for primary afferent firing based on a simulation of intrafusal mechanical events", J. Neurophysiology, vol. 65- 6: 1297-1311.

[55] Schulte HF Jr (1961) "The characteristics of the McKibben artificial muscle", in The Application of External Power in Prosthetics and Orthotics. National Academy of Sciences-National Research Council, Washington D. C.

[56] Shoemaker M (1993) "A study and model of the role of the Renshaw cell in regulating

the transient firing rate of the motoneuron", MSEE Thesis, University of Washington, Department of Electrical Engineering, June 1993.

[57] Shoemaker M & Hannaford B (1994) "A study and model of the role of the Renshaw cell in regulating the transient firing rate of the motoneuron", Biological Cybernetics, vol. 71: 251-262.

[58] Slotine J-J E (1985) "The robust control of robot manipulators", Intl. J. Robotics Research, vol. 4: 49-64.

[59] Snell RS (1980) "Clinical Anatomy for Medical Students", 2nd ed., Little, Brown and Company, Boston.

[60] Wierzbicka MM, Wiegner AW & Shahani BT (1986) "Role of agonist and antagonist muscles in fast arm movements in man", Exp. Brain Research, vol. 63-2: 331-340.

[61] Windhorst U (1989) "Do Renshaw cells tell spinal neurones how to interpret muscle spindle signals?" Progress in Brain Research, vol. 80: 283-294.

[62] Winters JM (1990) "Hill-based muscle models: a system engineering perspective", in: Multiple Muscle Systems, ch.5, eds. Winters & Woo, Springer-Verlag, New York.

[63] Wood JE, Meek SG & Jacobsen SC (1989a) "Quantitation of human shoulder anatomy for prosthetic arm control - I. Surface modeling", J. Biomech., vol. 22: 273-292.

[64] Wood JE, Meek SG & Jacobsen SC (1989b) "Quantitation of human shoulder anatomy for prosthetic arm control - II. Anatomy matrices", J. Biomech., vol. 22: 309-325.

[65] Yoshida K & Horch K (1996) "Closed-loop control of ankle position using muscle afferent feedback with functional neuromuscular stimulation", IEEE Trans. on Biomedical Engineering, vol. 43-2: 167-176.

[66] Zahalak GI (1990) "Modeling muscle mechanics (and energetics)", in: Multiple Muscle Systems, ch. 1, eds: Winters & Woo, Springer-Verlag, New York.

[67] Zuckerman JD & Matsen III FA (1989) "Biomechanics of the elbow", in Basic Biomechanics of the Musculoskeletal System, ch. 13, eds: Frankel VH, Lea & Febiger, Philadelphia.

Appendix A. Software Functional Block Diagram

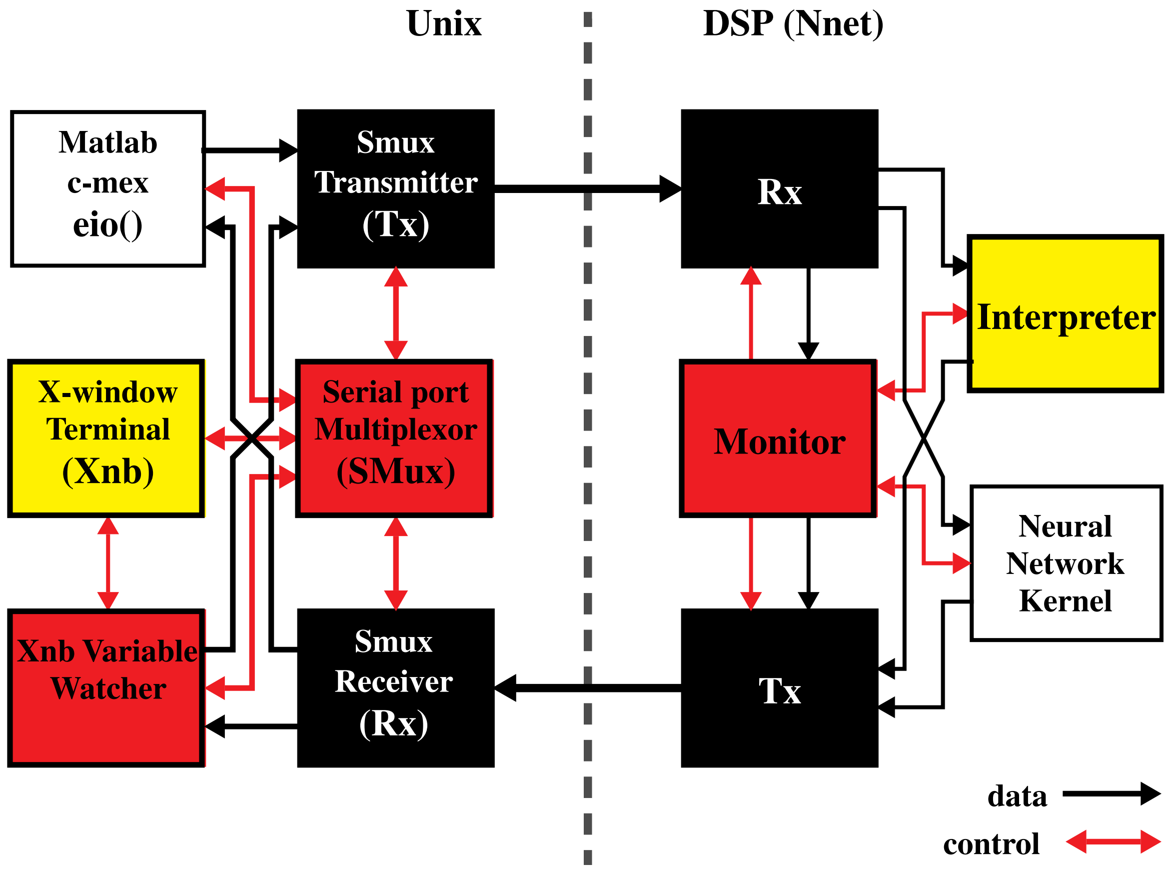

Fig.A.1 Software functional block diagram

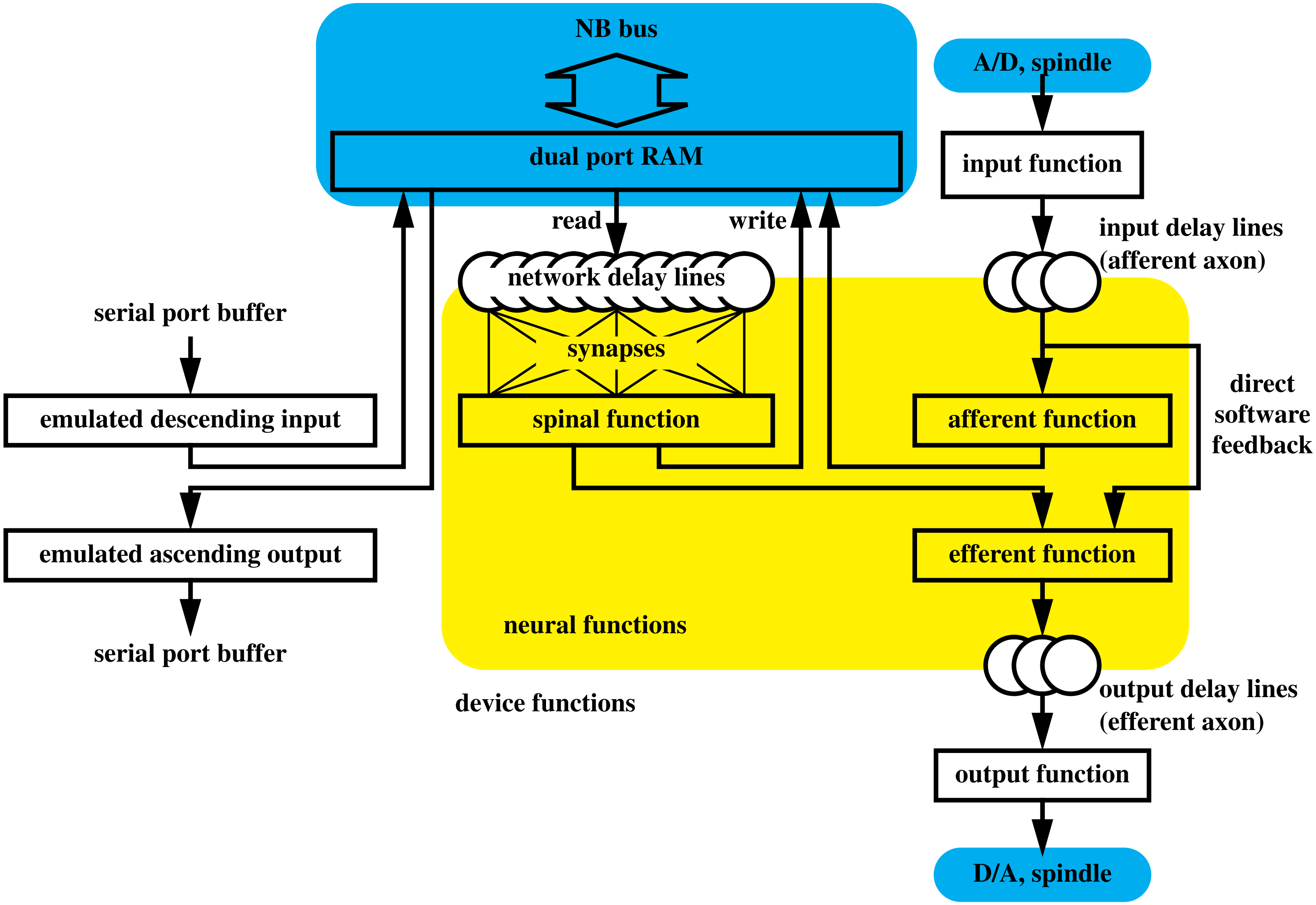

Fig.B.1 Neural controller data flow diagram

Appendix C. Example of Nnet Data and Command File

```
disable echo
disable verbal
disable spindle                     # select spindle model output
disable isr

create {                            # create data structure
    wave {                          # wave generators (non-physiological)
        (wave0);                    # co-contraction
        (wave1);                    # position
    }
    inter {                         # interneurons (non-physiol)
        (ff0);    (ff1);            # simple feed-forward
    }

    alpha {                         # alpha motoneurons
        (al0);    (al1);            # flexor, extensor
    }
    postalpha {                     # alpha MN post-processors (non-physiol)
        ([pa0 [1 0][1 0]]); ([pa1 [1 1][1 1]]);
    }
    ib {                            # Ib afferent sensory neurons
        ([ib0 [1 2]]);      ([ib1 [1 3]]);
    }
    gamma {                         # gamma motoneurons
        ([ga0 [0 0]]);      ([ga1 [0 1]]);
    }
    ia {                            # Ia afferent sensory neurons
        ([ia0 [0 0]]);      ([ia1 [0 1]]);
    }
    inter {                         # interneurons
        (ibin0);            (ibin1);        # Ib inhibitory
        (iain0);            (iain1);        # Ia inhibitory
        (rn0);              (rn1);          # Renshaw cells
    }

    out {                           # output to host computer (non-physiol)
        ([al0 0]);          ([al1 1]);
        ([ib0 2]);          ([ib1 3]);
        ([ga0 4]);          ([ga1 5]);
        ([ia0 6]);          ([ia1 7]);
        ([ibin0 8]);        ([ibin1 9]);
        ([iain0 10]);       ([iain1 11]);
        ([rn0 12]);         ([rn1 13]);
```

```
    }

    synapse {
        ([wave0 ff0]);      ([wave1 ff0]);                          # flexor side
        ([ff0 al0]);        ([ff0 ga0]);      ([ff0 ibin0]);        ([ff0 iain0]);
        ([al0 pa0]);        ([al0 rn0]);
        ([ib0 ibin0]);
        ([ibin0 al0]);      ([ibin0 ibin1]);
        ([ia0 al0]);        ([ia0 iain0]);
        ([iain0 al1]);      ([iain0 iain1]);
        ([rn0 al0]);        ([rn0 iain0]);    ([rn0 rn1]);

        ([wave0 ff1]);      ([wave1 ff1]);                          # extensor side
        ([ff1 al1]);        ([ff1 ga1]);      ([ff1 ibin1]);        ([ff1 iain1]);
        ([al1 pa1]);        ([al1 rn1]);
        ([ib1 ibin1]);
        ([ibin1 al1]);      ([ibin1 ibin0]);
        ([ia1 al1]);        ([ia1 iain1]);
        ([iain1 al0]);      ([iain1 iain0]);
        ([rn1 al1]);        ([rn1 iain1]);    ([rn1 rn0]);
    }
}

load {                                        # load parameters
    alpha([al0 al1]).[num den] = [[[1.8571 .0476 -1.8095] [-0.9048 0]]];
    alpha([al0 al1]).xoffset = [-0.05];
    postalpha([pa0 pa1]).[hyst anti_ratio] = [[[.15 .07] .7] [[.16 .165] .7]];
    ib([ib0 ib1]).num = [[0.5 0.5 0]];
    ia([ia0 ia1]).[sp_length sp_gain sp_offset sp_drag] =
        [[120 32 9 0.03 0.0005] [160 26 10 0.03 0.0005]];
    inter([rn0 rn1 iain0 iain1 ibin0 ibin1]).num = [[0.5 0.5 0]];
    inter([ibin0 ibin1]).[x0 y0 xamp yamp] = [[0.5 0.5 2 0.5]];

    synapse {
        ([[ff0 ga0] [ff1 ga1] []]).[weight delay] = [[1 -1e-4]];       # gamma dynamic
        ([]).weight = [];                                               # memorize .weight
        ([[wave0 wave1] [ff0 ff1]]) = [[0.4 0.4] [0.4 -0.4]];
        ([[ff0 al0] [ff1 al1] []]) = [1];
        ([[ff0 ibin0] [ff1 ibin1] []]) = [-1.25];
        ([[ff0 iain0] [ff1 iain1] []]) = [1];
        ([[al0 pa0 ] [al1 pa1] []]) = [1];
        ([[al0 rn0] [al1 rn1] []]) = [1];
        ([[ib0 ibin0] [ib1 ibin1] []]) = [1.4 1];
        ([[ibin0 al0] [ibin1 al1] []]) = [-0.5];
        ([[ibin0 ibin1] [ibin1 ibin0] []]) = [-0.25];
```

```
        ([[ia0 al0] [ia1 al1] []]) = [0.25 0.3];
        ([[ia0 iain0] [ia1 iain1] []]) = [0.25 0.3];
        ([[iain0 al1] [iain1 al0] []]) = [-0.5];
        ([[iain0 iain1] [iain1 iain0] []]) = [-0.5];
        ([[rn0 al0] [rn1 al1] []]) = [-0.25];
        ([[rn0 iain0] [rn1 iain1] []]) = [-0.25];
        ([[rn0 rn1] [rn1 rn0] []]) = [-0.5];
    }
    eioctrl = [[][]0];
}

restart wave
enable isr
enable verbal
enable echo
```

Ching-Ping Chou
4200 Union Bay Pl. N.E. Apt. 241
Seattle, WA 98105
(206) 524-5504
ccp@actin.ee.washington.edu

EDUCATION

01 / 92 - 06 / 96 **Ph.D in Electrical Engineering**, University of Washington, Seattle, Washington
Study of human motion control with a physiologically based robotic arm and spinal level neural controller.
Specialization: human motion control, spinal neural circuitry, kinesiology, biomechanics, McKibben pneumatic artificial muscle, real-time physiological-analogous artificial neural network controller.
Course work emphasis: artificial neural networks, parallel computer architectures, microwave circuits.

10 / 90 - 12 / 91 **MS in Electrical Engineering**, University of Washington, Seattle, Washington
Thesis: Dual stable point model of muscle activation and deactivation.
Course work emphasis: biomechanics, physiology, DSP, robotics, image understanding.

10 / 84 - 06 / 88 **BS in Electrical Engineering**, National Taiwan University, Taipei, Taiwan, Republic of China
Special projects: ultrasonic radar system, spread spectrum communication.
Course work emphasis: physics, engineering math., electronics, electromagnetics, digital circuits, computer architectures, communications, control systems, computer graphics.

EXPERIENCE

12 / 91 - 06 / 96 **Biorobotics Laboratory, University of Washington**, Research Assistant
In charge of Anthroform Arm Project: studied, designed, implemented, tested, and improved biomechanically and physiologically accurate robot arm and neural controller.

12 / 91 - 03 / 92 **Department of Electrical Engineering, University of Washington**, Teaching Assistant
Conduct undergraduate electronics and circuits laboratory section.

10 / 89 - 05 / 90 **Electronic Research & Service Organization / Industrial Technology Research Institute (Taiwan)**
Involved with wireless modem cards for PC: designed and implemented its virtual serial port interface to PC with EPLDs, and DSP algorithm and program; tested the cards in wireless networks.

SUPPLEMENTARY SKILLS

Languages: C++, C, Matlab/Simulink m-file/mex function, Pascal, Basic, Intel x86 Asm.
Software: Matlab/Simulink, Mathematica, Spice, AutoCAD, Framemaker.
Platforms: Sun sparc station (Unix+X window), PC (DOS+MS Windows), TI 320c30 DSP.
Hardware Design & Implementation: PC peripherals, AD, DA, amplifier & filter, phase lock loop, PWM, motor control, variant sensors and actuators.

AWARDS AND ACTIVITIES

09 / 87 & 02 / 88 Book Coupon Awards from National Taiwan University (twice).
05 / 94 - Present IEEE student member.
09 / 85 - 05 / 86 Computer Research Club member, National Taiwan University.
10 / 84 - 05 / 85 Aeronautics Club member, National Taiwan University.
10 / 84 - 05 / 88 Baseball team member, Electrical Engineering Department, National Taiwan University.

PUBLICATIONS

1996 C.-P. Chou, “Study of human motion control with a physiology based robotic arm and spinal level neural controller”, Ph.D. Dissertation, Electrical Engineering, University of Washington, June, 1996.

1996 C.-P. Chou & B. Hannaford, “Study of human forearm posture maintenance with a physiologically based robotic arm and spinal level neural controller”, submitted to Biological Cybernetics, April 9th, 1996.

1996 C.-P. Chou & B. Hannaford, “Measurement and modeling of McKibben pneumatic artificial muscles”, IEEE Transactions on Robotics and Automation, vol.12-1: 90-102.

1995 B. Hannaford, J.M. Winters, C.-P. Chou, P.H. Marbot, “The anthroform arm: a system for the study of spinal circuits”, Annals of Biomedical Engineering: L. Stark Special Issue, March 1995, vol. 23 no. 2.

1994 B. Hannaford, J.M. Winters, C.-P. Chou, “The anthroform biorobotic arm”, Video Proceedings, IEEE Intl. Conf. on Robotics and Automation, San Diego, CA, May 1994.

1994 C.-P. Chou & B. Hannaford, “Static and dynamic characteristics of McKibben pneumatic artificial muscles”, IEEE Intl. Conf. on Robotics and Automation, San Diego, CA, May 1994, vol. 1: 281-286.

1992 C.-P. Chou & B. Hannaford, “Dual stable point model of muscle activation and deactivation”, Biological Cybernetics, 1992, vol. 66: 511-523.

1991 C.-P. Chou, “Dual stable point model of muscle activation and deactivation”, Master Thesis, Electrical Engineering, University of Washington, 1991.